

---

Doctoral Dissertations

Student Theses and Dissertations

---

Fall 2021

## Sources of Quality Uncertainty in Laser Powder Bed Fusion Metal Additive Manufacturing

Zachary Young

*Missouri University of Science and Technology*

Follow this and additional works at: [https://scholarsmine.mst.edu/doctoral\\_dissertations](https://scholarsmine.mst.edu/doctoral_dissertations)



Part of the [Mechanical Engineering Commons](#)

Department: Mechanical and Aerospace Engineering

---

### Recommended Citation

Young, Zachary, "Sources of Quality Uncertainty in Laser Powder Bed Fusion Metal Additive Manufacturing" (2021). *Doctoral Dissertations*. 3191.

[https://scholarsmine.mst.edu/doctoral\\_dissertations/3191](https://scholarsmine.mst.edu/doctoral_dissertations/3191)

This thesis is brought to you by Scholars' Mine, a service of the Missouri S&T Library and Learning Resources. This work is protected by U. S. Copyright Law. Unauthorized use including reproduction for redistribution requires the permission of the copyright holder. For more information, please contact [scholarsmine@mst.edu](mailto:scholarsmine@mst.edu).

SOURCES OF QUALITY UNCERTAINTY IN LASER POWDER BED FUSION

METAL ADDITIVE MANUFACTURING

by

ZACHARY AARON YOUNG

A DISSERTATION

Presented to the Graduate Faculty of the

MISSOURI UNIVERSITY OF SCIENCE AND TECHNOLOGY

In Partial Fulfillment of the Requirements for the Degree of

DOCTOR OF PHILOSOPHY

IN

MECHANICAL ENGINEERING

2021

Approved by:

Dr. Lianyi Chen, Advisor  
Dr. Douglas Bristow, Co-Advisor  
Dr. Ashok Midha  
Dr. Frank Liou  
Dr. Yijia Gu

© 2021

Zachary Aaron Young

All Rights Reserved

## PUBLICATION DISSERTATION OPTION

This dissertation consists of the following three articles, formatted in the style used by the Missouri University of Science and Technology:

Paper I: found on pages 4 – 29, “Types of spatters and their features and formation mechanisms in laser powder bed fusion additive manufacturing process” has been published under Additive Manufacturing <https://doi.org/10.1016/j.addma.2020.101438>.

Paper II: found on pages 30 – 67, “Uncertainties induced by processing parameter variation in selective laser melting of Ti6Al4V revealed by in-situ x-ray imaging” is intended for submission in Materials special issue: “Metal Additive Manufacturing Application: Technological Advances, Metal Design, and Process Optimization.”.

Paper III: found on pages 68 – 100, “The Effect of Particle Size Distribution with Efficient Packing on Additive Manufacturing Powder Flowability and Selective Laser Melting” is intended for submission with Materials special issue: “Manufacturing and Mechanics of Materials”.

## ABSTRACT

Powder based additive manufacturing (AM) exhibits tremendous uncertainties, where variations in build quality is present despite utilizing similar build processing parameters. First, this work reports the features and formation mechanisms of five unique types of spatter during the LPBF process by in-situ high-speed, high-energy x-ray imaging. The unique physical characteristics of spatter are determined. The effect of laser scan speed and laser power on spatter formation, ejection, and mitigation are determined. Second, this work addresses the uncertainty challenge by identifying the sources of uncertainty in SLM by in-situ characterization due to variations from the additive manufacturing processing parameters needed for Ti6Al4V. Second, this work addresses the uncertainty challenge by identifying the sources of uncertainty in SLM by in-situ characterization due to variations from the additive manufacturing processing parameters needed for Ti6Al4V. We show that small variations in the laser beam size, power, scan speed, and powder bed thickness results in significant changes in the SLM dynamics.. Third, this work focuses on identifying the uncertainty due to particle size distribution (PSD) on the resulting Ti6Al4V powder's flowability. More specifically, we showed that the PSDs effect on flowability is not linear, rather the PSD near local high packing densities cause significant reductions in overall dynamic flowability and affect the finalized part's SLM dynamics. The understanding and control of these uncertainties are vital for increasing the capabilities and reliability of AM produced parts.

## ACKNOWLEDGMENTS

I would like to acknowledge most predominantly my advisor Dr. Lianyi Chen. Dr. Chen has and is a tremendous advisor, giving me enormous guidance, support, and mentoring during my time working for him as a research student. He has given me countless opportunities in the present and future and has helped guide me to greater capabilities professionally and academically.

I would like to acknowledge Dr. Chen's research group members that have given assistance in my growth and success as a graduate student. Specifically, I would like to thank Qilin Guo, Minglei Qu, Meelap M. Coday, S. Mohammad H. Hojjatzadeh, Luis I. Escano, and Dr. Lianghua Xiong.

I would like to acknowledge Argonne national laboratories IL, for their assistance and opportunities to resources to conduct these works.

I would like to acknowledge my Advisory committee members Dr. Robert Landers, Dr. Douglas Bristow, Dr. Frank Liou, Dr. Ashok Midha, and Dr. Yijia Gu for their time and assistance in the completion and improvement of this work.

I would like to acknowledge Boeing CAMT, Graduate Assistance in Areas of National Need (GAANN), and the National Science Foundation for supporting this research.

Finally, I want to thank the friends and family for the unbridled support and motivation to continue and pursue this work.

## TABLE OF CONTENTS

	Page
PUBLICATION DISSERTATION OPTION .....	iii
ABSTRACT.....	iv
ACKNOWLEDGMENTS .....	v
LIST OF ILLUSTRATIONS.....	x
LIST OF TABLES .....	xii
 SECTION	
1. INTRODUCTION.....	1
 PAPER	
I. TYPES OF SPATTERS AND THEIR FEATURES AND FORMATION MECHANISMS IN LASER POWDER BED FUSION ADDITIVE MANUFACTURING PROCESS .....	4
ABSTRACT .....	4
1. INTRODUCTION.....	5
2. MATERIAL AND METHOD.....	6
3. RESULTS AND DISCUSSION .....	8
3.1. IDENTIFICATION OF SPATTER TYPES AND FORMATION MECHANISMS .....	8
3.1.1. Solid Spatter.....	8
3.1.2. Metallic Jet.....	9
3.1.3. Powder Agglomeration Spatter.....	11
3.1.4. Entrainment Melting Spatter.....	12
3.1.5. Defect Induced Spatter.....	13

3.2. SCHEMATIC OF SPATTER FORMATION MECHANISMS .....	14
3.3. QUANTIFICATION OF SPATTER FEATURES .....	15
3.3.1. Spatter Speed and Size.....	16
3.3.2. Spatter Direction.....	17
3.4. EFFECTS OF PROCESSING PARAMETER ON SPATTER FORMATION AND MITIGATION.....	19
3.4.1. Effect of Laser Power and Scan Speed on Spatter Formation and Mitigation.....	19
3.4.2. Effects of Environment Pressure on Spatter Formation and Mitigation.....	22
3.4.3 Effects of Material Feedstock on Spatter Formation and Mitigation.....	24
4. CONCLUSION.....	24
ACKNOWLEDGEMENTS.....	25
BIBLIOGRAPHY.....	26
II. UNCERTAINTIES INDUCED BY PROCESSING PARAMETER VARIATION IN SELECTIVE LASER MELTING OF Ti6Al4V REVEALED BY IN-SITU X-RAY IMAGING .....	30
ABSTRACT.....	30
1. INTRODUCTION .....	31
2. MATERIALS AND METHOD.....	35
2.1. MATERIAL.....	35
2.2. IN-SITU HIGH-SPEED SYNCHROTRON X-RAY IMAGING EXPERIMENT .....	37
2.3. CHARACTERIZATION AND QUANTIFICATION OF THE SOURCES OF UNCERTAINTY IN SELECTIVE LASER MELTING	39
2.4. SELECTION OF UNCERTAINTY PROCESSING CONDITIONS .....	43

3. RESULTS AND DISCUSSION.....	46
3.1. LASER BEAM SIZE.....	46
3.2. LASER POWER.....	50
3.3. LASER SCAN SPEED.....	53
3.4. POWDER BED THICKNESS.....	56
3.5. SENSITIVITY ANALYSIS OF PROCESSING CONDITIONS.....	59
4. CONCLUSIONS.....	61
ACKNOWLEDGEMENTS.....	63
BIBLIOGRAPHY.....	63
III. THE EFFECT OF PARTICLE SIZE DISTRIBUTION WITH EFFICIENT PACKING ON ADDITIVE MANUFACTURING POWDER FLOWABILITY AND SELECTIVE LASER MELTING.....	68
ABSTRACT.....	68
1. INTRODUCTION.....	70
2. MATERIALS AND METHODS.....	73
2.1. POWDER AND PARTICLE SIZE DISTRIBUTION.....	73
2.2. EFFICIENT PARTICLE PACKING.....	75
2.3. FLOWABILITY TESTING.....	77
2.4. IN-SITU SELECTIVE LASER MELTING DYNAMICS.....	81
3. RESULTS AND DISCUSSION.....	84
3.1. AVALANCHE ANGLE AND BREAK ENERGY.....	84
3.2. EFFECT OF PSD ON FLOWABILITY.....	87
3.3. EFFECT OF PSD ON SLM DYNAMICS.....	89
3.4. SLM IMPACT DUE TO CHANGE IN PSD.....	91

4. CONCLUSION..... 93  
ACKNOWLEDGEMENTS .....95  
BIBLIOGRAPHY .....96

SECTION

2. CONCLUSION ..... 101  
VITA.....103

## LIST OF ILLUSTRATIONS

PAPER I	Page
Figure 1. Solid spatter.....	9
Figure 2. Metallic jet spatter.....	10
Figure 3. Powder agglomeration spatter.....	12
Figure 4. Entrainment melting spatter.....	13
Figure 5. Defect induced spatter.....	14
Figure 6. Schematic showing the formation mechanisms of all spatter types.....	15
Figure 7. Quantification of the speed and size of spatter.....	17
Figure 8. Effects of processing parameters on direction of spatter.....	18
Figure 9. Charts showing spatter formation under various processing conditions.....	20
Figure 10. Effect of atmosphere pressure on spatter behavior.....	23
<b>PAPER II</b>	
Figure 1. SEM imaging of two sizes of pyrogenesis powders with particle size distribution.....	36
Figure 2. Schematic of the in-situ high-speed synchrotron x-ray imaging and sample assembly setup.....	38
Figure 3. Dynamics of SLM.....	41
Figure 4. Process uncertainty causes.....	44
Figure 5. Variation in the SLM dynamics due to variation in the laser beam size for Ti6Al4V.....	46
Figure 6. Variation in the SLM dynamics due to variation in the laser power for Ti6Al4V.....	51

Figure 7. Variation in the SLM dynamics due to variation in the laser scan speed for Ti6Al4V. .... 54

Figure 8. Variation in the SLM dynamics due to variation in the powder bed thickness for Ti6Al4V. .... 58

### PAPER III

Figure 1. SEM images and histogram of particle size pyrogenesis powder was used for testing with two powder designated size ranges: ..... 74

Figure 2. SEM images and histogram of particle size distributions 4 powder size distributions were created by mixing different weight percentages of 15-25 $\mu m$  and 38- 45 $\mu m$  powders ..... 75

Figure 3. 3D representation of atomic packing method D.B Miracle's model of dense sphere packing for 15-25um(a) and 38-45um(b) particle distributions. .... 76

Figure 4. Schematic of powder revolution..... 78

Figure 5. SLM dynamics..... 82

Figure 6. Avalanche angle and break energy of different particle size distributions ..... 86

Figure 7. SLM dynamics..... 89

## LIST OF TABLES

PAPER II	Page
Table 1. Chemical composition of Ti6Al4V.....	37
Table 2. Experimental processing parameters for SLM Ti6Al4V.....	43
Table 3. Percent change in SLM dynamics induced by variations in laser beam size during laser scanning.....	49
Table 2. Percent change in SLM dynamics induced by variations in the laser power during scanning. ....	53
Table 3. Percent change in SLM dynamics induced by variations in the laser scan speed. ....	56
Table 4. Percent change in SLM dynamics induced by variations in the powder bed thickness. ....	59
PAPER III	
Table 1. PSDs Powder grain size distributions.....	75
Table 2. PSDs static density calculations. ....	80
Table 3. PSD's effects on avalanche angle and break energy. ....	86

## 1. INTRODUCTION

Additive manufacturing (AM) is a process of developing parts through feedstock material being fused in sections (or layers) to fabricate a final part. The applications of AM parts have grown into the fields of medical, aerospace, automotive, and private spheres. This growth is due to the method allowing the fabrication of unique, complex geometries without the need of post processing. The growing advantage over conventional methods is due to the applications for small scale part development without the costly need for tooling or molding. The limitation of AM manufacturing lies primarily in the lack of reliability of fabricated parts in terms of their final part properties and repeatability.

Laser powder bed fusion (LPBF) or also known as selective laser melting (SLM) is a process that deposits a bed of powder feedstock layer by layer for laser scanning during part fabrication. The dynamics are constantly changing during the AM process, causing uncertainty to the finalized part's properties. This uncertainty leads to reduction in part quality and repeatability. Some of the major uncertainties leading to the reduction in quality and capabilities of the SLM process lie in the spatter dynamics, sensitivity of processing conditions, and powder flowability. Determining the mechanisms driving these uncertainties are vital for the sustainability of AM in commercial and common use. Researching the underlying mechanisms that drive these uncertainties to determine the cause and test methods to mitigate or eliminate the uncertainty during SLM are vital.

To determine the cause of the uncertainty, research has been conducted utilizing visible light and IR videography and simulations. Visible light and IR videography can

monitor spatter moving behavior above the powder bed surface. However, they lack the ability to see through the metal powder bed, so the accurate determination of spatter formation mechanisms is difficult from the information acquired only above the powder bed surface. Simulations can model the melt pool which has revealed important physical mechanisms of spatter formation. Currently, simulations are hard to, however, accurately model the spatter formation resulting from the complex interplay of metal vapor plume and ambient gas flow.

In this work, we conduct hundreds of tests at varying laser parameters and environment conditions to obtain detailed insight into the types of spatter and their features and formation mechanisms. This work identifies five unique types of spatter that exist within the LPBF process. The formation mechanism of spatters has been determined and/or discussed. The size, speed, and direction have been quantified. The effects of the laser power, scan speed, and ambient pressure on spatter formation are also studied. We also report the sources of uncertainty in SLM due to variations from the optimized AM processing parameters for Ti6Al4V through in-situ characterization. We reveal the sensitivity of the SLM process to the processing parameters and identify the leading cause of uncertainty by quantifying the percent change in the SLM dynamics (depression zone dynamics, melt pool dynamics, build height dynamics, and spatter dynamics) due to three the laser processing parameters: (1) laser beam size, (2) laser power, and (3) laser scan speed and the three powder processing parameters: (1) powder size, (2) powder bed thickness, and (3) powder size distribution. The uncertainty in this work is studied by making small changes with respect to the optimized processing parameter needed for Ti6Al4V under SLM AM conditions. Finally, we incorporate D.B. Miracle's research to

determine the effect that the dense packing and varying PSDs of two unique powders have on the resulting flowability of the powder for powder spreading and determine the effects on SLM dynamics. The work investigates flowability characteristics of two powder sizes at various PSDs including D.B. Miracle's dense packing region to see if non-homogenous powders flow differently from a single mixture of powders. The goal is to determine the source of the uncertainty between commercially employed powders that lead to overall reductions in part quality and use.

## I. TYPES OF SPATTERS AND THEIR FEATURES AND FORMATION MECHANISMS IN LASER POWDER BED FUSION MANUFACTURING PROCESS

Zachary A. Young <sup>a, b</sup>, Qilin Guo <sup>b, c</sup>, Niranjana D. Parab <sup>d</sup>, Cang Zhao <sup>d</sup>, Minglei Qu <sup>b, c</sup>, Luis I. Escano <sup>b, c</sup>, Kamel Fezzaa <sup>d</sup>, Wes Everhart <sup>e</sup>, Tao Sun <sup>f\*</sup>, Lianyi Chen <sup>a, b, c\*\*</sup>

<sup>a</sup> Department of Mechanical and Aerospace Engineering, Missouri University of Science and Technology, Rolla, MO 65409, USA

<sup>b</sup> Department of Mechanical Engineering, University of Wisconsin-Madison, Madison, WI 53706, USA

<sup>c</sup> Department of Materials Science and Engineering, University of Wisconsin-Madison, Madison, WI 53706, USA

<sup>d</sup> X-ray Science Division, Advanced Photon Source, Argonne National Laboratory, Lemont, IL 60439, USA

<sup>e</sup> Department of Energy's Kansas City National Security Campus Managed by Honeywell FM&T, Kansas City, MO 64147, USA

<sup>f</sup> Materials Science and Engineering, University of Virginia, Charlottesville, VA 22904, USA

\* Corresponding author

\*\* Corresponding author

E-mail addresses: [lianyi.chen@wisc.edu](mailto:lianyi.chen@wisc.edu) (Lianyi Chen), [ts7qw@virginia.edu](mailto:ts7qw@virginia.edu) (Tao Sun)

**Keywords:** Spatter, Laser powder bed fusion, Additive manufacturing, High-speed imaging Synchrotron x-ray

### ABSTRACT

Spatter causes defect formation, powder redistribution and contamination in laser powder bed fusion (LPBF) additive manufacturing process. It is critical to distinguish

different types of spatters and understand their features and formation mechanisms. This work reports the features and formation mechanisms of five unique types of spatters during the LPBF process by in-situ high-speed, high-energy x-ray imaging. Spatters observed during LPBF testing were quantified by their speed, size, and direction. Distinct quantifiable characteristics for each type of spatter are identified. Effects of the laser power, scan speed, and ambient pressure on spatter formation and features are also revealed.

## 1. INTRODUCTION

Laser powder bed fusion (LPBF) is an additive manufacturing technology that can manufacture metal parts with complex geometry[1–5]. During fabrication, unfortunately, the spatters generated during laser-matter interaction have been witnessed to cause defects and part quality uncertainty [3,4,13–22,5,23–32,6,33,7–12] , which severely limits the application of LPBF-manufactured parts.

To determine the cause of spatter formation, research has been conducted utilizing visible light and IR videography[27,29] and simulations[2,6,26,28]. Visible light and IR videography can monitor spatter moving behavior above the powder bed surface[24,28,29]. However, they lack the ability to see through the metal powder bed, so the accurate determination of spatter formation mechanisms is difficult from the information acquired only above the powder bed surface. Simulations can model the melt pool which has revealed important physical mechanisms of spatter formation. Currently,

simulations are hard to, however, accurately model the spatter formation resulting from the complex interplay of metal vapor plume and ambient gas flow.

Recently, we showed that high speed x-ray imaging can overcome the limitations of conventional characterization tools to reveal the dynamics of spattering behavior during LPBF process[25]. We revealed spattering dynamics as a function of time, pressure, and location throughout the manufacturing process. However, our previous work did not distinguish different types of spatter.

In this work, we conduct hundreds of tests at varying laser parameters and environment conditions to obtain detailed insight into the types of spatter and their features and formation mechanisms. This work identifies five unique types of spatter that exist within the LPBF process. The formation mechanism of spatters has been determined and/or discussed. The size, speed, and direction have been quantified. The effects of the laser power, scan speed, and ambient pressure on spatter formation are also studied.

## **2. MATERIAL AND METHOD**

High-speed high-energy x-ray imaging (Beamline 32-ID-B, Advanced Photon Source, Argonne National Laboratory) was used to monitor the dynamics of spattering during the laser melting process. The experiments were first recorded at a frame rate of 45,259 fps (frames per second) to primarily determine physical characteristics of the phenomena. Then, a high frame rate of 135,776 fps was used to capture the detailed process of how certain phenomena form. ImageJ is used for image processing throughout the experimental data analysis.

An IPG continuous-wave (CW) ytterbium fiber laser (IPG YLR-500-AC, IPG Photonics, Oxford, USA) with a wavelength of 1070 nm and a maximum output power of 520W was used to melt the material. A laser scanner (IntelliSCANde 30, SCANLAB GmbH., Germany) is used to control laser scan speed. For all testing, a laser beam incident angle of 90 degrees was used throughout testing. The laser scan path was a single continuous scan of 3-4 mm perpendicular to the x-ray

Two commonly used additive manufacturing materials were used in testing the spatter dynamics in LPBF: Aluminum (AlSi10Mg) and titanium (Ti6Al4V). The feedstock powder is fabricated using plasma atomization. The resulting powder is spherical with near negligible satellites or internal porosity present. The powder size for aluminum and titanium feedstock is 15-38 $\mu$ m. and 25-45 $\mu$ m, respectively. The aluminum feedstock was obtained from Renishaw. The composition by mass contains 9-11% silicon, 0.25-0.45% Magnesium, and less than 0.25 of iron, nitrogen, oxygen, titanium, zinc, manganese, nickel, copper, lead, and tin. Titanium feedstock is provided by EOS. The composition by mass contains 5.5-6.5% aluminum, 3.5-4.5% Vanadium, and less than 0.25 oxygen, nitrogen, carbon, hydrogen, and iron.

Powder layers are spread on a metal substrate with identical composition to the powder. Two pieces of glassy carbon are mounted as side walls to hold the powder in place. The powder layer thickness is determined by the difference in height between the substrate and glassy carbon. Powder layer thickness is set at roughly 100 $\mu$ m to maintain consistent melt pool dynamics across testing. Powder size is varied between aluminum and Titanium depending on the supplier specification. Both aluminum and titanium were tested in our work. Testing is conducted in a vacuum chamber filled with argon gas

of 99.99% purity. Environmental pressure is varied from the region of near vacuum (0.002 atm) to atmospheric (1 atm) to observe the effects of ambient pressure.

### 3. RESULTS AND DISCUSSION

#### 3.1. IDENTIFICATION OF SPATTER TYPES AND FORMATION MECHANISMS

Five types of spatter were identified through in-situ analysis of the LPBF process. The spatter formation dynamics were captured and analyzed to determine their individual formation mechanisms. The five types of spatter and their formation mechanisms are discussed in detail below.

**3.1.1. Solid Spatter.** During scanning, powder was observed to be ejected prior to sufficient laser interaction to induce melting. Large amounts of un-melted spatter were seen throughout the entire scanning process. This type of un-melted spatter is referred to as solid spatter. The solid spatter generation is caused by the vapor jet (intense vapor generated due to localized laser heating) interacting with solid powder outside the strong laser interaction region. The vapor jet can create sufficient force to eject unmelted powders before melting can take place. Fig 1 shows the dynamics of the vapor jet ejecting unmelted powders away from the melt pool. The details about the vapor jet induced spatter phenomena can be found in our previous publication [25]. Solid spatter formation can lead to non-uniformity in powder layer thickness but has less detrimental effects on the overall part quality compared to liquid spatter [5,26–29,33].

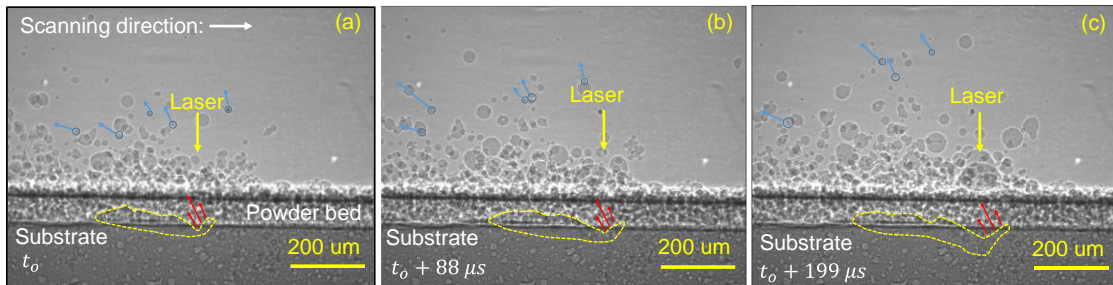


Figure 1. Solid spatter. Dynamic X- ray images showing dynamics of solid spatter when a laser beam with a diameter of 100  $\mu\text{m}$  and power of 322 W scans a powder bed with a layer thickness of 100  $\mu\text{m}$  at a scan speed of 0.8 m/s. Yellow arrow and dashed line indicate the position of the laser beam and the melt pool boundary, respectively. Blue circles and arrows indicate the representative solid spatters ejecting from the substrate over time. Red arrows indicate the hypothesized vapor jet direction.

**3.1.2. Metallic Jet.** Liquid droplet was observed to be ejected from the melt pool at the edge of the depression zone region. This type of spatter is referred to as metallic jet spatter. The formation of the metallic jet spatter is caused by the intense metallic vapor during the localized laser heating process. The intense metallic vapor generates high recoil pressure and shear forces on the depression zone's vapor-liquid interface during the LPBF process. The recoil pressure creates strong melt flow along the depression zone walls. The intense vapor flow also generates shear forces on the depression zone wall, contributing to high speed spatter upward from the melt pool. When the metallic vapor is intense enough to produce force capable of overcoming the surface tension, necking of the melt pool begins to appear on the walls of the depression zone (Figure 2, b,e) and leads to the liquid detachment from the elongated melt pool protrusion (Figure. 2, c,f). Our recent results show that bulk-explosion is also an important mechanism for metallic jet formation[18]. The production of metallic jet spatter is reliant on the intensity of the

vapor jet and stability of the depression zone; this makes deep, unstable depression zones more prominent in the production of metallic jet type spatters.

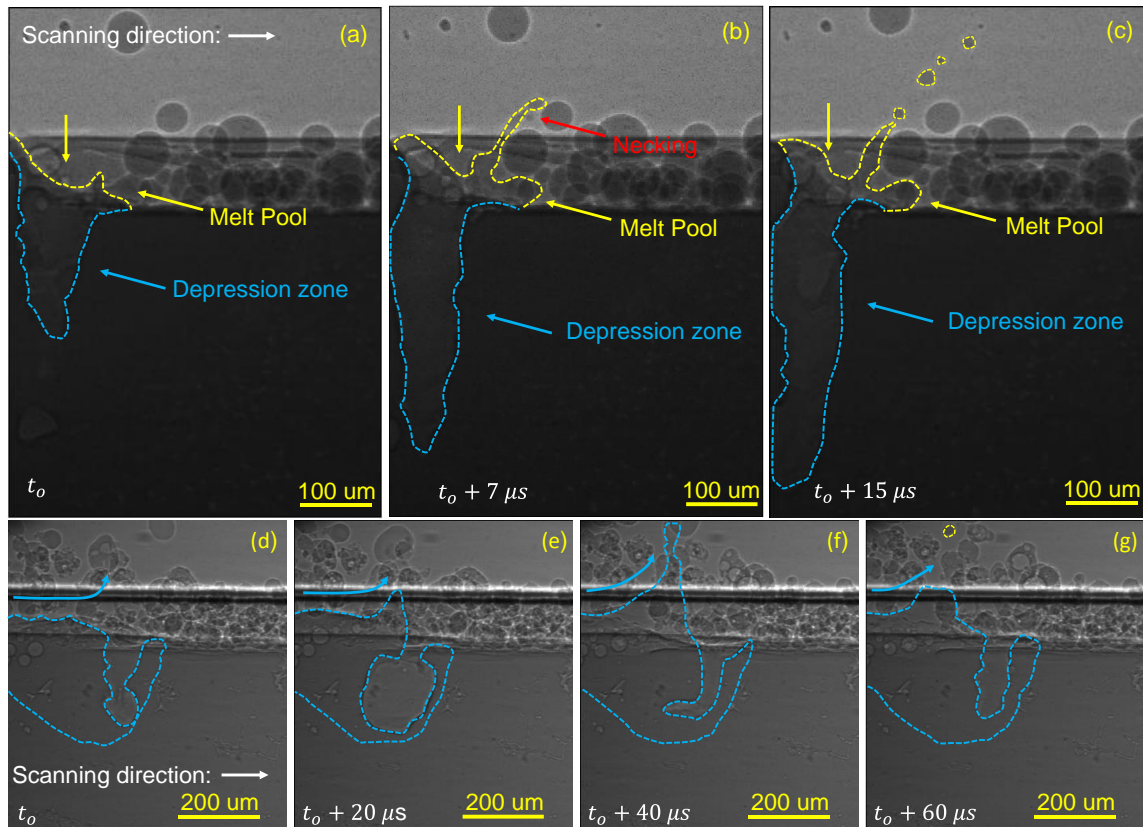


Figure 2. Metallic jet spatter. Dynamic X-ray images demonstrating front metallic jet spatter formation (a-c) and rear metallic jet formation (d-g). (a,d) Protrusion formation at the edge of the depression zone region. (b,e) Lengthening and necking of the protrusion. (c,f) Breaking of the neck to form liquid droplet (spatter). The rapid increase of the depth or the width of the depression zone was observed during the spatter formation process, which indicates the rapid depression zone expansion causes the spatter formation. The depression zone and top of the melt pool boundaries are marked in blue and yellow dashed lines, respectively. Figure a-c material is Ti6Al4V, laser power is 260 W, scan speed is 0.2 m/s. Figure d-f material is AlSi10Mg, laser power is 416 W, scan speed is 0.5 m/s.

**3.1.3. Powder Agglomeration Spatter.** Powders and spatters were observed to agglomerate and coalesce to form spatters many times larger than the original feedstock powder. This type of spatter is referred to as powder agglomeration spatter. Two main kinds of powder agglomeration spatter are commonly observed in the experiment: liquid-solid powder agglomeration and liquid-liquid powder agglomeration. Liquid-solid powder agglomeration spatter is seen as feedstock powders being melted near the melt pool region but not being captured and absorbed by it. Two forces contribute to the agglomeration ejection: the vapor plume and near side vaporization driven ejection of agglomerate. The vapor plume initially ejects the liquid spatter and allows the agglomerate to escape the powder bed. The laser beam also vaporizes the rear side of the ejecting spatter which pushes the liquid ball away from the laser beam[34]. The liquid ball then travels along the powder bed region (Figure. 3, a) and captures the un-melted feedstock powders (Figure. 3, b-c) along its path to grow, very similar to the growth of a snowball. The spatter is then ejected due to vaporization of the powder and vaporization of the depression zone, pushing the liquid ball away from the laser heating region to form a big spatter.

Liquid-liquid powder agglomeration spatter is the coalescence of two liquid spatter particles by colliding. Figs. 3(d-f) shows one example. Two independent liquid spatters are ejected away from the melt pool (Figure. 3d). During ejection, the two powders collide (Figure. 3e) causing the liquid spatters to consolidate into a single, larger spatter (Figure. 3f).

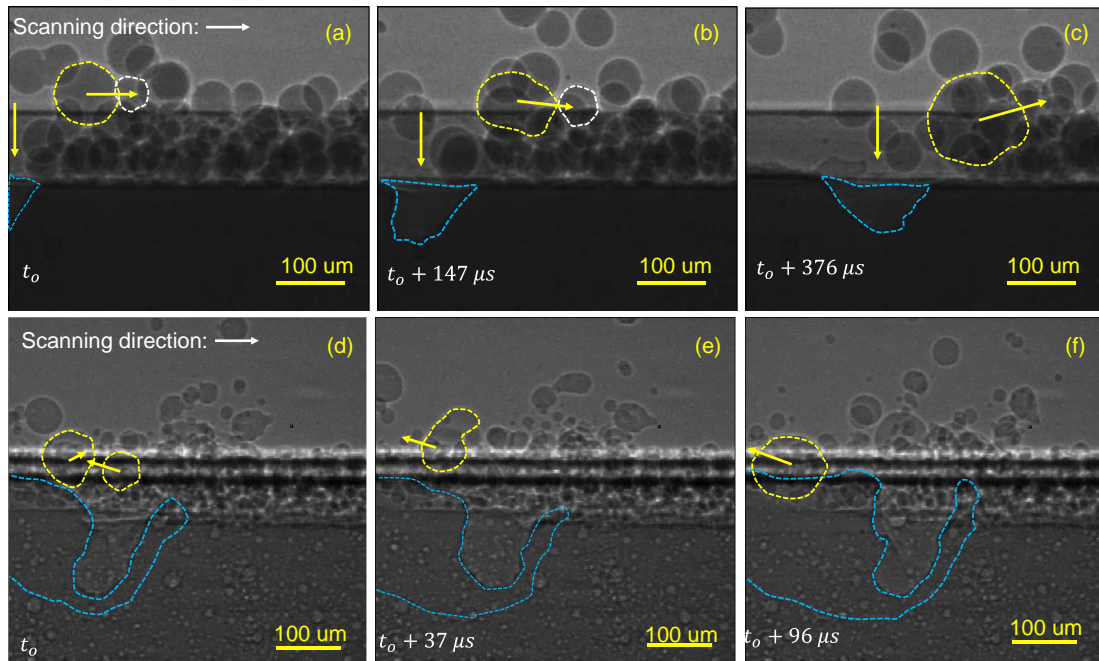


Figure 3. Powder agglomeration spatter. (a-c), Dynamic X-ray images demonstrating liquid-solid powder agglomeration spatter. Liquid droplets and solid feedstock powder prior to absorption are indicated by yellow and white dashed lines, respectively. (a) A liquid droplet (indicated by yellow dashed circle) is pushed or ejected away from the laser heating region towards the powder in front of the laser (the powder that will be absorbed by the liquid droplet is indicated by white dashed circle). (b) The liquid droplet and powder indicated in (a) merged to form a larger liquid ball (indicated by yellow dashed circle in b). The newly merged liquid ball was pushed towards another powder in the powder bed (indicated by the white dashed circle). (c) Absorption of multiple feedstock powders causing liquid droplet grows to multiple times larger than the size of the feedstock powder. (d-f), Dynamic X-ray images demonstrating liquid-liquid powder agglomeration spatter. (d) Initially melted powder droplets were ejected with different moving directions. (e) Then the two liquid droplets collide and merge during ejection. (f) Finally, the combined droplet ejects from the melt pool region. In (a-c), the material is Ti6Al4V, laser power is 312W, laser scan speed is 0.6 m/s. In (d-f), the material is AlSi10Mg, laser power is 416W, scan speed is 1.0 m/s. Melt pool boundaries are indicated by blue dashed lines.

**3.1.4. Entrainment Melting Spatter.** Ambient gas flow can carry solid powder to the laser heating region, also known as powder entrainment. Once the entrained solid powders encounter the laser beam, the solid powders are melted (Figure. 4 a,b) and ejected by the vapor jet (Figure. 4c). Sometimes, the melted entrained powders can

collide and coalesce (Figure. 4 a,b). This type of spatter is referred to as entrainment melting spatter.

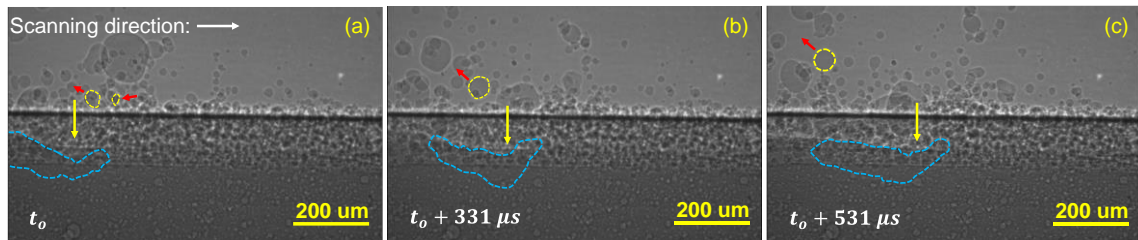


Figure 4. Entrainment melting spatter. Dynamic X-ray images demonstrating entrainment melting spatter. (a) A solid and liquid spatter get entrained towards the laser heating region. (b) The two spatters melt and coalesce in the laser heating region forming a single liquid droplet. (c) The liquid droplet was re-ejected away from the laser. Testing was conducted using a laser with a beam diameter of 100  $\mu\text{m}$  and laser power of 416W. The laser scans the AlSi10Mg powder bed at a rate of 0.4 m/s. The dashed yellow circles indicate the tracked spatters. The yellow arrow marks the location of the laser beam. The red arrow marks the moving direction of the spatter. The blue dashed lines indicate the melt pool boundary.

**3.1.5. Defect Induced Spatter.** X-ray imaging demonstrates that when the laser interacts with severe defects within the part such as large pores or cracks, a sudden eruption of liquid spatter can occur. During melting, laser interaction with these large pores exhibits sudden instability and results in unique spatter. This type of spatter is termed defect induced spatter. Figure 5 demonstrates an example of defect induced spatter recorded using x-ray imaging. During laser scanning, the melt pool comes into contact with a large pre-existing pore (Figure. 5a). The large pore interacts violently with the melt pool to cause the formation of liquid spatter (Figure. 5c). The rapid expansion of the trapped gas in the pore and/or the rapid change of the absorbed laser energy by multiple reflections in the pore are possible mechanisms for defect induced spatter.

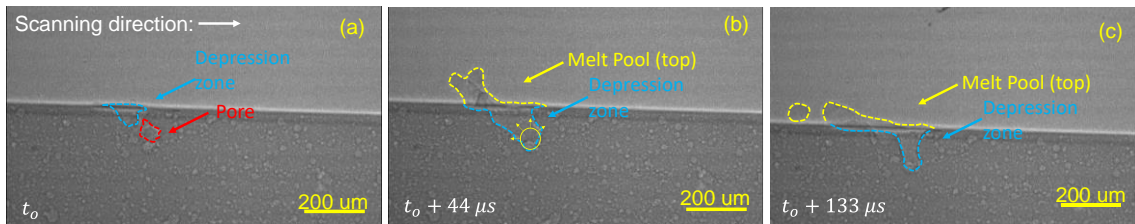


Figure 5. Defect induced spatter. Dynamic X-ray images demonstrating an example of defect induced spatter. Laser scans from left to right across the substrate. (a) The depression zone travels along the substrate towards a large pre-existing pore. (b) The interaction between melt pool/depression zone with the localized defect cause a sudden eruption out of the melt pool. (c) The ejection of a large liquid spatter occurs as the melt pool attempts to reform to steady state after eruption (a-c) show an AlSi10Mg substrate scanning at 416W laser power and 1.0m/s scan speed. The pre-existing pore and depression zones are outlined in red and blue respectively. The large defect interacting with the melt pool is marked and labeled. The sudden melt pool instability and resulting spatter are highlighted in yellow for all images. The laser beam size is 100  $\mu\text{m}$ .

### 3.2. SCHEMATIC OF SPATTER FORMATION MECHANISMS

To better visualize and understand spatter in the LPBF process, a schematic was constructed to summarize the spatter types and their formation mechanisms, as shown in Figure. 6. The formation dynamics of solid spatter, metallic jet spatter, powder agglomeration spatter, entrainment melting spatter and defect induced spatter are pointed out by A, B, C (C1 and C2), D and E, respectively.

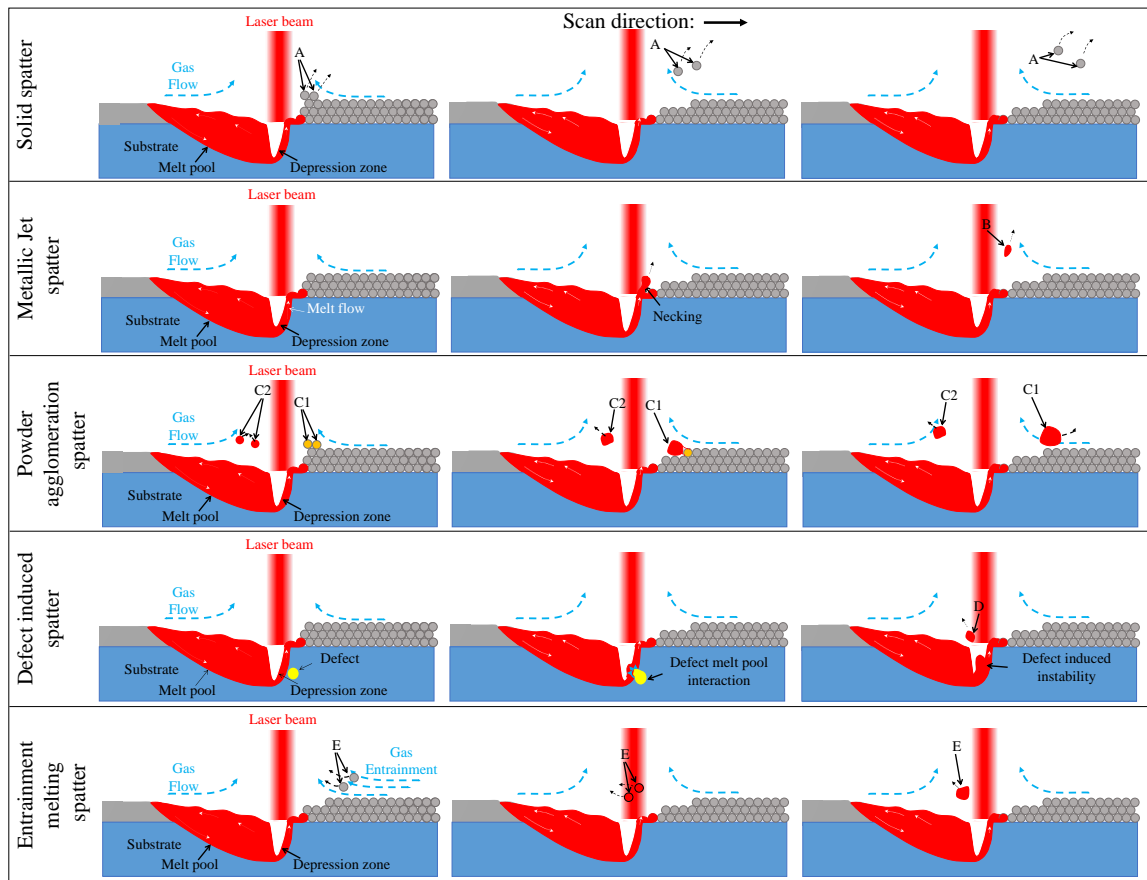


Figure 6. Schematic showing the formation mechanisms of all spatter types. A. Solid spatter. B. Metallic jet spatter. C. Powder agglomeration spatter (C1, liquid-solid agglomeration spatter, C2, liquid-liquid agglomeration spatter). D. Entrainment melting powder spatter. E. Defect induced spatter.

### 3.3. QUANTIFICATION OF SPATTER FEATURES

The size, speed and direction of the spatters are different due to their different formation mechanisms. Quantification was done by frame-by-frame manual powder tracking of individual spatter to maintain accuracy and ensure minimal error. Solid spatter will always remain constant in size due to no melting during ejection. Defect induced spatter is difficult to be quantified statistically due to the low number and randomness of pre-existing pores within tested substrates. As a result, these two types of

spatters were not included in the quantification study of their spatter features. All quantitative testing was conducted with aluminum for the consistency of comparison.

**3.3.1. Spatter Speed and Size.** The speed of the particles was quantified individually by recording the change in position of the object's geometric center over intervals of time. The standard deviation is taken from the variation of the average speeds generated by the particles observed and quantified. The spatter's speed is driven by their formation and ejection mechanisms, but the material properties and processing parameters being tested can also influence the speed of the ejected spatter. Average speeds of three types of spatter were determined and compared (Figure. 7a). The metallic jet was determined to be the fastest of the four phenomena, with an average speed of 2.17 m/s. Entrainment melting spatter moves faster than powder agglomeration spatter due to the large size difference or an initial velocity prior to melting. The powder agglomeration spatter followed behind the entrainment melting spatter with an average speed of 0.66 m/s. The standard deviation of the metallic jet is 1.30 m/s. The large variation in speed is caused by multiple spatters being ejected from the same protrusion; the initial ejected spatter has greater speed than the subsequent spatter.

The size of the four types of spatter are quantified (Figure. 7b). As expected, the solid spatter has the same size as the feedstock powder. The powder agglomeration spatter has the largest size with an average diameter of 114  $\mu\text{m}$ , which is over 4 times larger than the feedstock powder. The entrainment melting spatter has a size of 57  $\mu\text{m}$  in diameter, which is about 3 times larger than the feedstock powder. The metallic jet spatter's size is with an average size of 31  $\mu\text{m}$ , which is close to the size of the feedstock powder.

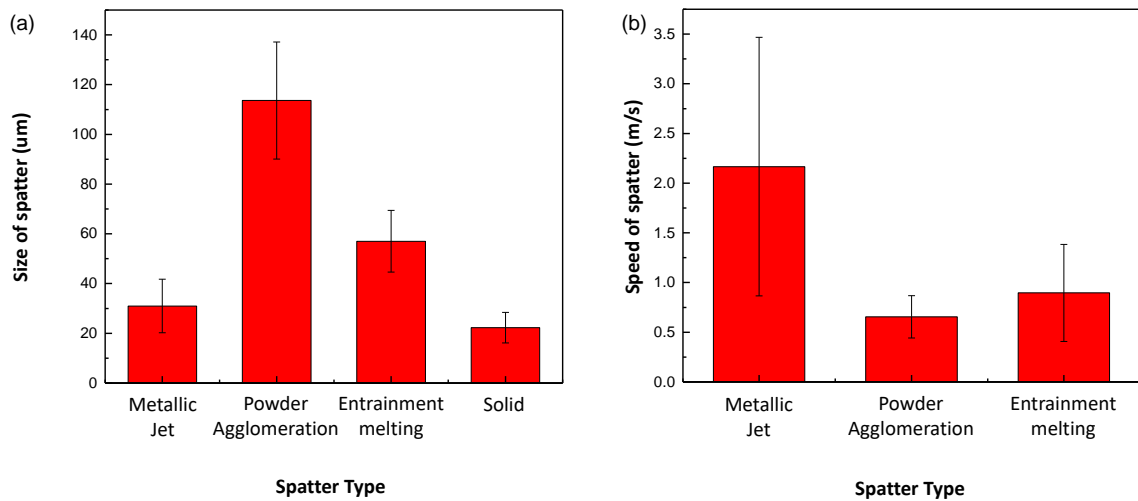


Figure 7. Quantification of the speed and size of spatter. (a) Spatter speed. (b) Spatter size. The material is AlSi10Mg. The error bar indicates standard deviation. Spatter phenomena are determined and collected from multiple videos under varying scanning speeds and laser powers.

**3.3.2. Spatter Direction.** Quantifying the moving directions of the different types of spatter were conducted. The results showed a general trend that the moving direction of the metallic jet spatter makes the smallest angle with the laser beam (normal to direction of the substrate) and the moving direction of the powder agglomeration spatter makes the largest angle with the laser beam. However, the spatter's moving direction varies in a very large range and strongly depends on processing parameters.

The dependence of the spatter direction on processing parameters originates from the effect of processing parameters on vapor jet direction, as shown in Figure. 8. Changing the laser power at a constant laser scan speed (Figure.8 a-c) or changing the scan speed at a constant laser power (Figure. 8 d-f) can significantly change the depression-zone geometry. The depression zone changes from a deep keyhole shape (with a depth over half width ratio larger than one) at high laser power and low scan

speed to a wide-open shape (with a depth over half width ratio less than one) at low laser power and high scan speed. Consequently, the vapor jet direction changes from nearly parallel to the depression zone front wall to nearly normal to the depression front wall. Since vapor jet is the major driven factor for spatter formation and moving, the spatter direction changes accordingly.

Due to the strong dependence of spatter direction on processing parameter, it is very hard to make a quantitative comparison among different types of spatters. However, the correlation among the spatter direction, depression-zone shape and laser processing parameter has important implications for developing in-situ monitoring tools based on spatter characteristics.

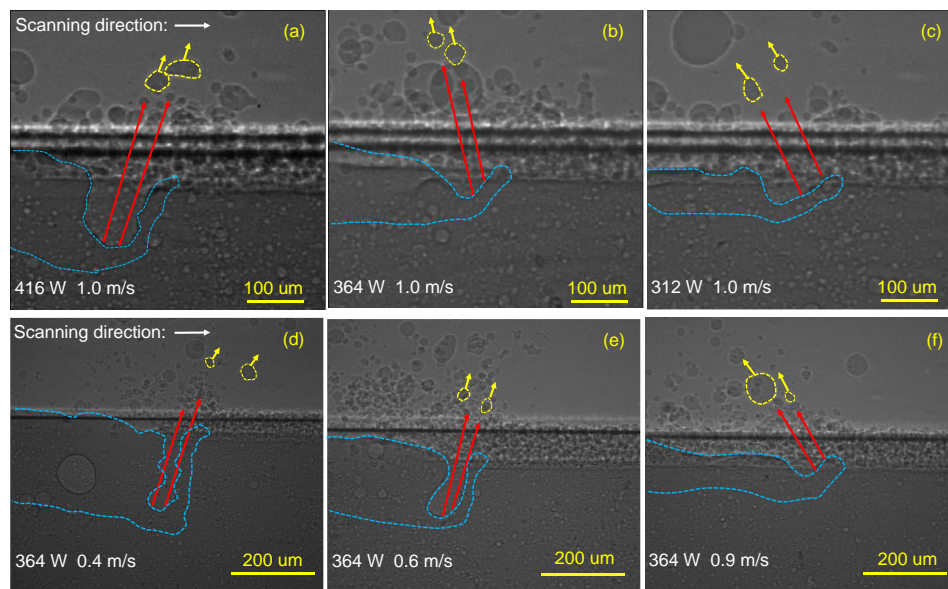


Figure 8. Effects of processing parameters on direction of spatter. (a-c) X-ray images demonstrating the effects of laser power on spatter direction and depression zone geometry. (d-f) X-ray images showing the effects of scan speed on spatter direction and depression zone geometry. Melt pool and spatter are outlined by blue and yellow dashed lines, respectively. Red arrows indicate the hypothesized vapor jet direction. The material is AlSi10Mg.

### **3.4. EFFECTS OF PROCESSING PARAMETER ON SPATTER FORMATION AND MITIGATION**

During quantification, isolating the effects of different processing parameters delivered some dramatic changes to different spatter phenomena. Changes to different dynamics within the melt pool and surrounding region lead to mitigation or elimination of different spatter types. Testing was conducted to determine the regions where laser power, scan speed, and ambient pressure induce mitigation or elimination of the observed spatter types.

**3.4.1. Effect of Laser Power and Scan Speed on Spatter Formation and Mitigation.** Laser power and scan speed play important role in spatter formation. The effects of laser power and scan speed on the formation of different types of spatters are summarized in Figure. 9.

Solid spatter was witnessed during all laser power and scan speed conditions tested (Figure 9a). Solid spatter is produced through vaporized metal ejecting unmelted powder away from the substrate. Our testing was conducted only when melting could occur, so elimination of solid spatter was not possible. Solid spatter mitigation was witnessed slightly by reducing the laser power or increasing the scan speed to reduce the overall energy density. The decrease in energy density reduces the strength of the vapor jet preventing more solid spatter from being ejected.

Metallic jet spatter was observed within a specific laser power and scan speed range (Figure 9b). Elimination was seen by reducing the laser power or by increasing the scan speed above certain thresholds. Reduction in laser power (below 364 W) or increase in laser scan speed (greater than 1 m/s) decreases the input energy density. This decrease causes the vapor jet and melt flow strength to be insufficient to produce metallic jet

spatter. Decreasing the scan speed (below 0.3 m/s) was also observed to eliminate the production of metallic jet spatter for AlSi10Mg. At the reduced scan speed, the resulting depression zone becomes a deep keyhole. When the keyhole is very deep, the highest intensity of the melt flow is at the bottom of the melt pool. The high intensity melt flow weakens as it travels up the depression zone walls. The resulting momentum of the liquid on the keyhole rim is then not high enough to form long protrusion that can be sheared off from the melt pool.

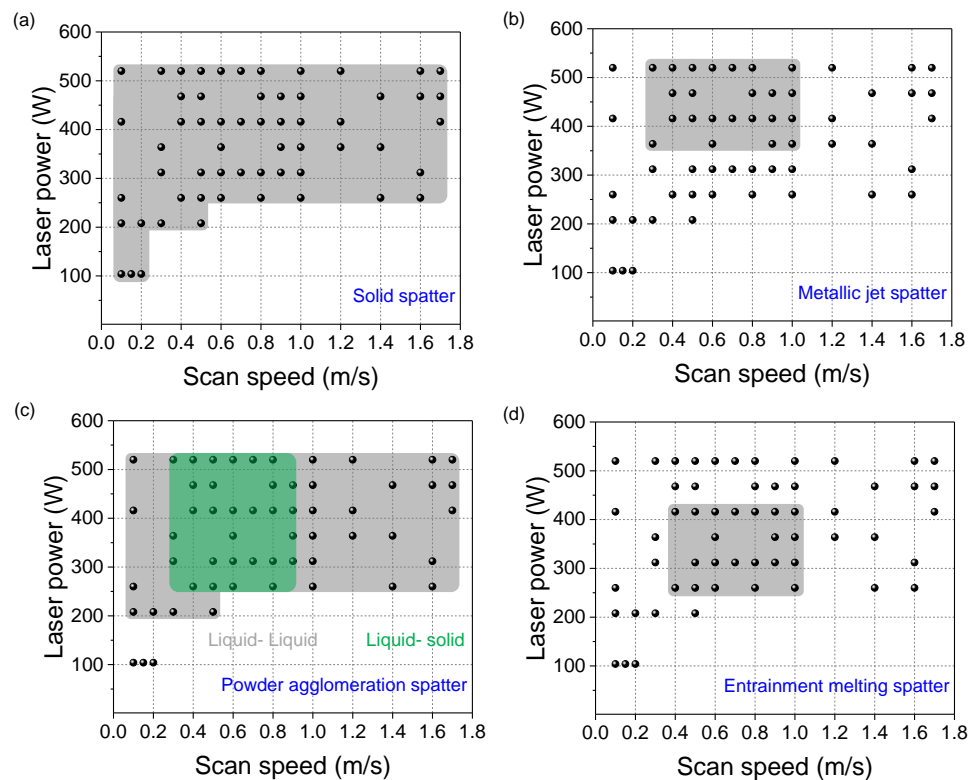


Figure 9. Charts showing spatter formation under various processing conditions. (a) Solid spatter. (b) Metallic jet spatter. (c) Powder agglomeration spatter. (d) Entrainment melting spatter. The material is AlSi10Mg. Black dots indicate the parameters tested. The shaded areas indicate the area that a specific type of spatter was observed. All outlines are generated by observations of spatter from our testing at specified processing conditions and are not verified as thresholds or absolute edges where the specific spatter types are capable to form.

Liquid-liquid powder agglomeration spatter was witnessed during all laser power and scan speed conditions tested (Figure 9c). The inability to prevent liquid-liquid powder agglomeration is due to the incorporation of feedstock powders interacting with laser heating. Like solid powder, the melted powder is ejected by the vapor jet. The only occurrences where liquid-liquid powder agglomeration was not present is in the absence of noticeable melting needed for LPBF.

Liquid-solid powder agglomeration spatter elimination, however, was possible by changes in laser power and scan speed (Figure 9c). Liquid-solid agglomeration spatter is generated by direct laser heating, but are pushed along the solid powder bed by the escaping vaporized material. Above 0.9 m/s, the laser was capable of overtaking the speed of the agglomerating spatter and capture it within the melt pool preventing ejection. Below 0.3 m/s, the generated vapor jet was too strong relative to the ambient gas flow causing liquid spatter to not be pushed into the unmelted feedstock but, rather, eject as liquid-liquid powder agglomeration spatter instead. Liquid-solid powder agglomeration spatter can be many times larger than many of the other types of spatter, so the ability to eliminate this from the process is vital for overall spatter reduction in LPBF process.

Entrainment melting spatter only occurred within a small region of the laser processing conditions during testing (Figure 9d). The occurrence of entrainment melting spatter is strongly related to force generated by the ambient gas flow and vapor jet. Testing above 416W laser power generated a vapor jet that was too powerful for entrained solid spatter to overcome the outward force and interact with the laser heating region. This phenomenon was also present when operating below 0.4m/s. The vaporized material buildup at lower speeds was too strong for entrained solid powders to reach laser

heating before being ejected. Testing done at speeds higher than 1.0m/s caused entrained powders to not interact within laser heating region long enough or be able to catch up to the laser scanning to induce melting.

### **3.4.2. Effects of Environment Pressure on Spatter Formation and Mitigation.**

Environment pressure has a great influence on spatter formation, as shown in Figure 11. Two spatter types were primarily affected by the reduction in the environmental pressure: solid spatter and entrainment melting spatter. Solid spatter occurred at every LPBF testing when manipulating laser power, scan speed, or environmental pressure. The solid spatter was, however, substantially affected by environmental pressure. When the pressure was reduced from 760 torr (Figure 10a-c) to 0.087 torr (Figure 10d-f), the resulting solid spatter was substantially increased. Under vacuum, there is no ambient pressure to counteract the vaporization pressure produced during melting causing an increase in solid spatter in all direction [20]. Higher pressures mitigate the outward force generated by the vaporized material as well as channeling its direction due to ambient gas flow being present. Entrainment melting spatter generation requires the presence of ambient gas flow as its primary mechanism for solid spatter entrainment. The reduction from 760 torr to 0.087 torr decreased the ambient gas flow where spatter entrainment was not possible. The inability for solid spatter to be entrained causes the elimination of entrainment melting spatter when operating in near vacuum conditions.

Liquid-solid powder agglomeration spatter also requires the assistance of ambient gas flow to keep the agglomerating spatter from immediately being ejected. Without strong ambient gas flow, powder directly melted from the laser immediately escape due to the vaporization pressure. Reducing the environmental pressure from 1 atm to 0.087

torr eliminated the production of liquid-solid powder agglomeration spatter.

Unfortunately, liquid-liquid powder agglomeration spatter was unable to be eliminated by the reduction of environmental pressure.

The alteration in the environmental pressure was also unable to eliminate the production of defect induced spatter or metallic jet spatter. A reduction in the environmental pressure reduces the melting point of metals, but even under near vacuum conditions, the presence of metallic jet spatter was still witnessed. Defect induced spatter is generated specifically from the incorporation of defects and no visible evidence was found to show mitigation or elimination of defect induced spatter due to changes in environmental pressure.

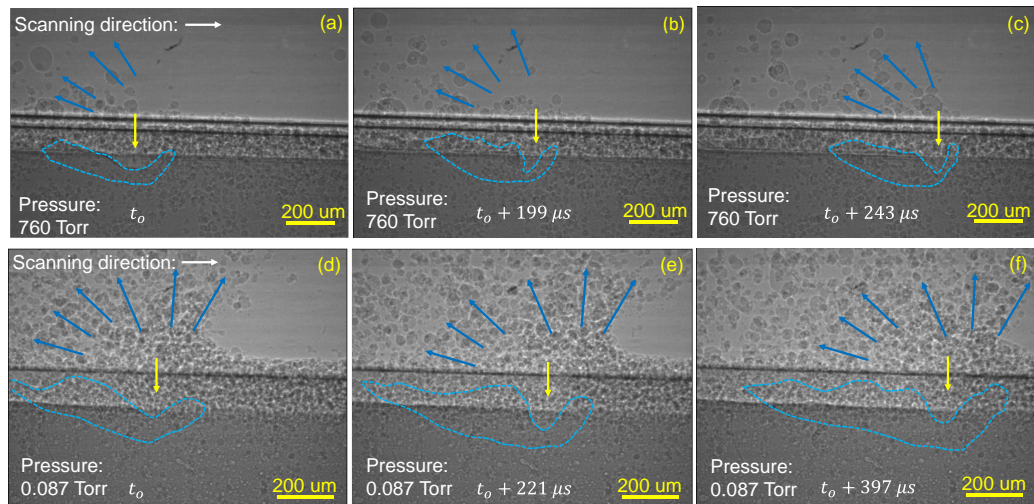


Figure 10. Effect of atmosphere pressure on spatter behavior. (a-c), Dynamic x ray images showing spattering behavior under 760 Torr (1 atm). (d-f) Dynamic x ray images showing spattering behavior under 0.087 Torr (0.00132 atm). The laser power is 416 W, beam size is 100  $\mu\text{m}$ , scan speed is 1.0 m/s. The yellow arrow indicates the current location of the laser beam. The blue dashed lines indicate the melt pool boundaries. Quantity and direction of solid and liquid spatter can be easily identified from regions marked with blue arrows.

### **3.4.3. Effects of Material Feedstock on Spatter Formation and Mitigation.**

Both aluminum and titanium spatter dynamics were observed during LPBF. The underlying formation and propagation phenomena are consistent between the two materials. However, the differences in the melting/boiling point of the material altered the processing parameters that initiated the formation of different spatter. This indicates that the spatter formation map is dependent on the material being processed.

## **4. CONCLUSION**

This work has distinguished five types of spatter produced in the LPBF process. The formation mechanism and features of each type spatter are identified and quantitatively analyzed. The major conclusions are listed below:

1. Five types of spatter are observed and identified in the LPBF process: solid spatter, metallic jet spatter, agglomeration spatter, entrainment melting spatter, and defect induced spatter.
2. The five types of spatter's formation mechanisms were analyzed and described. Solid spatter is formed due to the intense vapor jet ejecting un-melted feedstock powders out of the powder bed. Metallic jet spatter is the detachment of liquid droplet from the melt pool resulting from the intensive vaporization induced high recoil pressure and shear force. Powder agglomeration spatter is formed through coalescing of multiple powders/spatters. Entrainment melting spatter is the melting and ejection of the entrained powders. Defect induced spatter is induced by large defects within the previously built layers.

3. The speed, size, and direction of metallic jet spatter, agglomeration spatter, and entrainment melting spatter were quantified. Metallic jet spatter exhibits the highest speed, powder agglomeration spatter has the largest size. The direction of the spatter highly depends on the depression zone geometry, which provides a potential way to determine the shape of the depression zone from spatter direction.

4. Types of spatters formed in LPBF process and their features depend on processing parameters (laser power, scan speed, and environmental pressure). A spatter formation map is constructed.

## **ACKNOWLEDGEMENTS**

This work is funded by Honeywell Federal Manufacturing & Technologies (FM&T), National Science Foundation. The authors would like to thank Alex Deriy at the APS for his help on the beamline experiments. This research used resources of the Advanced Photon Source, a U.S. Department of Energy (DOE) Office of Science User Facility operated for the DOE Office of Science by Argonne National Laboratory under Contract No. DE-AC02-06CH11357. All data prepared, analyzed and presented has been developed in a specific context of work and was prepared for internal evaluation and use pursuant to that work authorized under the referenced contract. Reference herein to any specific commercial product, process or service by trade name, trademark, manufacturer, or otherwise, does not necessarily constitute or imply its endorsement, recommendation, or favoring by the United States Government, any agency thereof or Honeywell Federal Manufacturing & Technologies, LLC. This publication has been authored by Honeywell

Federal Manufacturing & Technologies under Contract No. DE-NA0002839 with the U.S. Department of Energy. The United States Government retains and the publisher, by accepting the article for publication, acknowledges that the United States Government retains a nonexclusive, paid up, irrevocable, world-wide license to publish or reproduce the published form of this manuscript, or allow others to do so, for the United States Government purposes.

## BIBLIOGRAPHY

- [1] D.D. Gu, W. Meiners, K. Wissenbach, R. Poprawe, Laser additive manufacturing of metallic components: materials, processes and mechanisms, *Int. Mater. Rev.* 57 (2013) 133–164.
- [2] S.A. Khairallah, A.T. Anderson, A. Rubenchik, W.E. King, Laser powder-bed fusion additive manufacturing: Physics of complex melt flow and formation mechanisms of pores, spatter, and denudation zones, *Acta Mater.* 108 (2016) 36–45. <https://doi.org/10.1016/j.actamat.2016.02.014>.
- [3] C.Y. Yap, C.K. Chua, Z.L. Dong, Z.H. Liu, D.Q. Zhang, L.E. Loh, S.L. Sing, Review of selective laser melting: Materials and applications, *Am. Inst. Phys.* 2 (2015) 01–21. <https://doi.org/10.1063/1.4935926>.
- [4] A.A. W. E. King R. Ferencz, N. Hodge, S.K. C. Kamath A. Rubencik, Laser powder bed fusion additive manufacturing of metals; physics, computational, and materials challenges, *Acta Mater.* 108 (2016) 36–45.
- [5] W. Gao, Y. Zhang, D. Ramanujan, K. Ramani, Y. Chen, C.B. Williams, C.C.L. Wang, Y.C. Shin, S. Zhang, P.D. Zavattieri, The status, challenges, and future of additive manufacturing in engineering, *Comput. Des.* 69 (2015) 65–89. <https://doi.org/10.1016/j.cad.2015.04.001>.
- [6] P. Bidare, I. Bitharas, R.M. Ward, M.M. Attallah, A.J. Moore, Laser powder bed fusion in high-pressure atmospheres, *Int. J. Adv. Manuf. Technol.* 99 (2018) 543–555. <https://doi.org/10.1007/s00170-018-2495-7>.
- [7] B. Song, S. Dong, B. Zhang, H. Liao, C. Coddet, Effects of processing parameters on microstructure and mechanical property of selective laser melted Ti6Al4V, *Mater. Des.* 35 (2012) 120–125. <https://doi.org/10.1016/j.matdes.2011.09.051>.

- [8] B. Zhang, L. Dembinski, C. Coddet, The study of the laser parameters and environment variables effect on mechanical properties of high compact parts elaborated by selective laser melting 316L powder, *Mater. Sci. Eng. A.* 584 (2013) 21–31. <https://doi.org/10.1016/j.msea.2013.06.055>.
- [9] T.M. Mower, M.J. Long, Mechanical behavior of additive manufactured, powder-bed laser-fused materials, *Mater. Sci. Eng. A.* 651 (2015) 198–213. <https://doi.org/10.1016/j.msea.2015.10.068>.
- [10] M. Grasso, B.M. Colosimo, Process defects and in situ monitoring methods in metal powder bed fusion: a review, *Meas. Sci. Technol.* 28 (2017) 44005. <https://doi.org/10.1088/1361-6501/aa5c4f>.
- [11] J. Yin, L.L. Yang, X. Yang, H. Zhu, D. Wang, L. Ke, Z. Wang, G. Wang, X. Zeng, High-power laser-matter interaction during laser powder bed fusion, *Addit. Manuf.* 29 (2019) 100778. <https://doi.org/10.1016/j.addma.2019.100778>.
- [12] X. Zhang, B. Cheng, C. Tuffile, Simulation study of the spatter removal process and optimization design of gas flow system in laser powder bed fusion, *Addit. Manuf.* 32 (2020). <https://doi.org/10.1016/j.addma.2020.101049>.
- [13] R. Esmailizadeh, U. Ali, A. Keshavarzkermani, Y. Mahmoodkhani, E. Marzbanrad, E. Toyserkani, On the effect of spatter particles distribution on the quality of Hastelloy X parts made by laser powder-bed fusion additive manufacturing, *J. Manuf. Process.* 37 (2019) 11–20. <https://doi.org/10.1016/j.jmapro.2018.11.012>.
- [14] C. Barrett, C. Carradero, E. Harris, K. Rogers, E. MacDonald, B. Conner, Statistical analysis of spatter velocity with high-speed stereovision in laser powder bed fusion, *Prog. Addit. Manuf.* 4 (2019) 423–430. <https://doi.org/10.1007/s40964-019-00094-6>.
- [15] A. Bin Anwar, I.H. Ibrahim, Q.C. Pham, Spatter transport by inert gas flow in selective laser melting: A simulation study, *Powder Technol.* 352 (2019) 103–116. <https://doi.org/10.1016/j.powtec.2019.04.044>.
- [16] D. Wang, G. Ye, W. Dou, M. Zhang, Y. Yang, S. Mai, Y. Liu, Influence of spatter particles contamination on densification behavior and tensile properties of CoCrW manufactured by selective laser melting, *Opt. Laser Technol.* 121 (2020) 105678. <https://doi.org/10.1016/j.optlastec.2019.105678>.
- [17] D. Galicki, B.C. Chakoumakos, S.P. Ringer, M. Eizadjou, C.J. Rawn, K. Nomoto, S.S. Babu, On the Formation of Spherical Metastable BCC Single Crystal Spatter Particles during Selective Laser Melting, *Materialia*. in press (2020) 100584. <https://doi.org/10.1016/j.mtla.2020.100584>.

- [18] C. Zhao, Q. Guo, X. Li, N. Parab, K. Fezzaa, W. Tan, L. Chen, T. Sun, Bulk-Explosion-Induced Metal Spattering during Laser Processing, *Phys. Rev. X.* 9 (2019) 21052. <https://doi.org/10.1103/PhysRevX.9.021052>.
- [19] U. Ali, R. Esmailizadeh, F. Ahmed, D. Sarker, W. Muhammad, A. Keshavarzkermani, Y. Mahmoodkhani, E. Marzbanrad, E. Toyserkani, Identification and characterization of spatter particles and their effect on surface roughness, density and mechanical response of 17-4 PH stainless steel laser powder-bed fusion parts, *Mater. Sci. Eng. A.* 756 (2019) 98–107. <https://doi.org/10.1016/j.msea.2019.04.026>.
- [20] A.T. Sutton, C.S. Kriewall, M.C. Leu, J.W. Newkirk, B. Brown, Characterization of laser spatter and condensate generated during the selective laser melting of 304L stainless steel powder, *Addit. Manuf.* 31 (2020) 100904. <https://doi.org/10.1016/j.addma.2019.100904>.
- [21] A. Masmoudi, R. Bolot, C. Coddet, Investigation of the laser–powder–atmosphere interaction zone during the selective laser melting process, *J. Mater. Process. Technol.* 225 (2015) 122–132. <https://doi.org/10.1016/j.jmatprotec.2015.05.008>.
- [22] V. Semak, A. Matsunawa, The role of recoil pressure in energy balance during laser materials processing, *J. Phys. D. Appl. Phys.* 30 (1997).
- [23] T.L.R.H.X.C.S.G.S. Pang, Localized boiling-induced spatters in the high-power laser welding of stainless steel: three-dimensional visualization and physical understanding, *Appl. Phys. Rev.* (n.d.).
- [24] V. Gunenthiram, P. Peyre, M. Schneider, M. Dal, F. Coste, I. Koutiri, R. Fabbro, Experimental analysis of spatter generation and melt-pool behavior during the powder bed laser beam melting process, *J. Mater. Process. Technol.* 251 (2018) 376–386. <https://doi.org/10.1016/j.jmatprotec.2017.08.012>.
- [25] Q. Guo, C. Zhao, L.I. Escano, Z. Young, L. Xiong, K. Fezzaa, W. Everhart, B. Brown, T. Sun, L. Chen, Transient dynamics of powder spattering in laser powder bed fusion additive manufacturing process revealed by in-situ high-speed high-energy x-ray imaging, *Acta Mater.* 151 (2018) 169–180. <https://doi.org/10.1016/j.actamat.2018.03.036>.
- [26] M.J. Matthews, G. Guss, S.A. Khairallah, A.M. Rubenchik, P.J. Depond, W.E. King, Denudation of metal powder layers in laser powder bed fusion processes, *Acta Mater.* 114 (2016) 33–42. <https://doi.org/10.1016/j.actamat.2016.05.017>.
- [27] D. Wang, S. Wu, F. Fu, S. Mai, Y. Yang, Y. Liu, C. Song, Corrigendum to “Mechanisms and characteristics of spatter generation in SLM processing and its effect on the properties,” *Mater. Des.* 137 (2018) 33–37. <https://doi.org/10.1016/j.matdes.2016.12.060> [10.1016/j.matdes.2017.09.058](https://doi.org/10.1016/j.matdes.2017.09.058).

- [28] M. Taheri Andani, R. Dehghani, M.R. Karamooz-Ravari, R. Mirzaeifar, J. Ni, Spatter formation in selective laser melting process using multi-laser technology, *Mater. Des.* 131 (2017) 460–469. <https://doi.org/10.1016/j.matdes.2017.06.040>.
- [29] Y. Liu, Y. Yang, S. Mai, D. Wang, C. Song, Investigation into spatter behavior during selective laser melting of AISI 316L stainless steel powder, *Mater. Des.* 87 (2015) 797–806. <https://doi.org/10.1016/j.matdes.2015.08.086>.
- [30] M. Simonelli, C. Tuck, N.T. Aboulkhair, I. Maskery, I. Ashcroft, R.D. Wildman, R. Hague, A Study on the Laser Spatter and the Oxidation Reactions During Selective Laser Melting of 316L Stainless Steel, Al-Si10-Mg, and Ti-6Al-4V, *Metall. Mater. Trans. A.* 46 (2015) 3842–3851. <https://doi.org/10.1007/s11661-015-2882-8>.
- [31] M.J. Zhang, G.Y. Chen, Y. Zhou, S.C. Li, H. Deng, Observation of spatter formation mechanisms in high-power fiber laser welding of thick plate, *Appl. Surf. Sci.* 280 (2013) 868–875. <https://doi.org/10.1016/j.apsusc.2013.05.081>.
- [32] D.K.Y. Low, L. Li, A.G. Corfe, Characteristics of spatter formation under the effect of different laser parameters during laser drilling, *J. Mater. Process. Technol.* 118 (2001) 179–186.
- [33] W.E. King, H.D. Barth, V.M. Castillo, G.F. Gallegos, J.W. Gibbs, D.E. Hahn, C. Kamath, A.M. Rubenchik, Observation of keyhole-mode laser melting in laser powder-bed fusion additive manufacturing, *J. Mater. Process. Technol.* 214 (2014) 2915–2925. <https://doi.org/10.1016/j.jmatprotec.2014.06.005>.
- [34] S.A. Khairallah, A.A. Martin, J.R.I. Lee, G. Guss, N.P. Calta, J.A. Hammons, M.H. Nielsen, K. Chaput, E. Schwalbach, M.N. Shah, M.G. Chapman, T.M. Willey, A.M. Rubenchik, A.T. Anderson, Y.M. Wang, M.J. Matthews, W.E. King, Controlling interdependent meso-nanosecond dynamics and defect generation in metal 3D printing, *Science* (80-. ). 368 (2020) 660–665.

## II. UNCERTAINTIES INDUCED BY PROCESSING PARAMETER VARIATION IN SELECTIVE LASER MELTING OF Ti6Al4V REVEALED BY IN-SITU X-RAY IMAGING

Zachary Young<sup>1,2</sup>, Meelap M. Coday<sup>1,2,3</sup>, Qilin Guo<sup>2,3</sup>, Minglei Qu<sup>2,3</sup>, S. Mohammad H. Hojjatzadeh<sup>1,2,3</sup>, Luis I. Escano<sup>2</sup>, Kamel Fezzaa<sup>4</sup>, Lianyi Chen<sup>1,2,3\*</sup>

<sup>1</sup>Department of Mechanical and Aerospace Engineering, Missouri University of Science and Technology, Rolla, Missouri 65409, USA.

<sup>2</sup>Department of Mechanical Engineering, University of Wisconsin-Madison, Madison, Wisconsin 53706, USA.

<sup>3</sup>Department of Materials Science and Engineering, University of Wisconsin-Madison, Madison, Wisconsin 53706, USA.

<sup>4</sup>X-ray Science Division, Advanced Photon Source, Argonne National Laboratory, Lemont, Illinois 60439, USA.

\*Correspondence to: Lianyi Chen ([lianyi.chen@wisc.edu](mailto:lianyi.chen@wisc.edu)).

### ABSTRACT

Selective laser melting (SLM) additive manufacturing (AM) exhibits uncertainties, where variations in build quality is present despite utilizing similar build processing parameters. In this work, we identify the sources of uncertainty in SLM by in-situ characterization of SLM dynamics induced by small variations in additive manufacturing processing parameters needed for Ti6Al4V. We show that variations in the laser beam size, power, scan speed, and powder bed thickness results in significant variations in the depression zone, melt pool, and spatter behavior. Small (<5%) variations from the optimized laser processing parameters resulted in significant, linear variations in the depression zone, melt pool, and spatter behavior. On average, a small deviation of

only ~5% from the optimized laser processing parameter resulted in a ~10% or greater change in the depression zone and melt pool geometries. Small ( $<50\mu\text{m}$ ) variations in the powder bed thickness processing parameters resulted in substantial changes in the depression zone dynamics ( $>30\%$ ). The laser beam size was found to have significant impact on the spatter dynamics during laser melting, affecting the overall volume ( $>40\%$ ) of spatter generated. This work experimentally identifies what small scale changes in the most significant processing parameters do to the SLM dynamics during AM processing. The variation in the SLM dynamics identified in this work is vital for understanding the sensitivity of the SLM process due to minute changes in AM processing parameters.

**Keywords:** Selective laser melting, laser powder bed fusion, additive manufacturing, Spatter, Melt pool dynamics, quality uncertainty.

## 1. INTRODUCTION

Selective laser melting (SLM, also called laser powder bed fusion) is a type of additive manufacturing (AM) that utilizes a high-power density laser to selectively fuse together metallic powders to form three-dimensional objects [1–3]. Complex-shaped metal parts for rapid production with high levels of flexibility and customization compared to conventional manufacturing is revolutionizing the metal manufacturing industry for aerospace, biomedical, and defense applications [2]. Presently, SLM still faces several challenges: (1) parts printed by the same machine and using the same optimized parameters are not always identical, (2) properties of the printed parts can be difficult to predict, (3) optimal parameters to print a part still rely on trial-and-error

parameter development, and (4) defect sensitive properties (e.g., fatigue life) of SLM parts often result in lower properties than parts fabricated from wrought product forms. An understanding of the fundamental mechanisms of SLM AM and identifying the causes for part quality uncertainty is important for addressing and overcoming the challenges in SLM AM.

During the SLM process, the interaction between the laser and the powder in the region of the highest intensity results in the formation of a cavity due to material vaporization. This vaporization region is known as the depression zone. Immediately surrounding the depression zone where there is still sufficient energy to melt the metallic powders, the powders fuse together to form a localized liquid region known as the melt pool. The newly formed melt pool rapidly cools and leaves behind a new build layer. Once the new build layer has solidified, a new layer of powder is added to the top surface and the processes is repeated until a three-dimensional part is formed in a layer-by-layer fashion. During laser vaporization and melting, molten material known as spatter can be ejected from the depression zone and melt pool regions [1].

Four of the most significant processing parameters [4,5] that can be manipulated to control the SLM process include: (1) the laser beam size, (2) the laser power, (3) the laser scan speed, and (4) powder bed thickness. Each one of these parameters will influence the resulting shape and size of the depression zone, the melt pool, and the spatter behavior. Previous publications show that the processing parameters are a critical factor that contribute to the resulting microstructural features and mechanical properties since they influence the thermal history and cooling rates for Ti6Al4V and other AM materials [1,2,6–14]. Additional works highlight the importance of the powder bed

thickness on the resulting properties of the manufactured part[15–18]. These works make use of energy density equations to describe the effects of laser processing parameters on the dynamics of the AM process [9–12]. Other works use simulations which utilize thermal and fluid flow models to describe heat flow during the AM process [2,9,10].

Previous works highlight the importance and impact of SLM process uncertainty on the finalized parts properties. Work by Criaes et al. and Ma et al. both utilized finite element modeling to analytically demonstrate the processing parameter sensitivity. Analysis demonstrated changes to the underlying physics of SLM systems under processing parameter change; these changes demonstrated the effect laser power and laser scan speed uncertainty generating significant variations to the peak temperature, melt pool geometry, and uncertainty quantification of AM parts[19,20]. Experimental work conducted by Roehling et al. demonstrated the impact of beam size and shape manipulation on resulting microstructure. Their work demonstrated the tailoring of the beam size and beam ellipticity to effectively manipulate change in the microstructure of AM parts. Increases in beam size were demonstrated to increase continuity and smoothness of finalized tracks, while beam ellipticity demonstrated strong manipulation to the AM part's microstructure[21]. Determining the effect of powder layer thickness on AM have been conducted thoroughly to discern the variations produced on part quality. Work by Han et al. utilized discrete element simulation to analytically demonstrate the change in deposition consistency when varying layer thickness and experimentally validated the resulting microstructural and tensile conditions. Findings demonstrated the creation of voids and defects within powder layers attributing to decreases in tensile strength and porosity inclusions of fully built parts[22]. Additional work by Nguyen et al.

conducted additional experimental testing, demonstrating the effects of powder layer thickness on resulting mechanical properties. Their work demonstrated increases in finalized part strength, modulus, hardness, and elongation properties generated by larger grain size systems in reduced powder bed systems with nano-sized precipitates[17]. Additionally, extensive work has been performed by Kusuma et al., Suzuki et al., and Khorasani et al. to identify the effect of AM laser and scan speed processing conditions on finalized part properties[23–25].

Previous works have extensively depicted the importance of AM processing conditions on finalized part properties. Specifically, published research has noted the sudden changes in part properties when altering the laser and powder processing conditions. Previous works, however, have not conducted extensive work to experimentally determine the correlation between the SLM melt pool and spatter dynamics that effectively drive the changes to the solidification rate, undercooling, grain refinement, and porosity generation which reduce the finalized part properties and consistency. Previous works have also not identified the significance of small changes in processing conditions on the impact they have on the in-situ SLM dynamics. The work and understanding of these principles are vital for the proper process control to stabilize the SLM uncertainty driving part limitations and lack of repeatability in commercial AM use.

Utilizing in-situ high-speed high-energy high-resolution synchrotron x-ray imaging allows for the dynamics of the SLM during the laser melting process to be observed and analyzed [30–32]. Dimensional characteristics for the depression zone and melt pool can be extracted from x-ray images which correspond to the real-time behavior

of the material under SLM AM conditions. The real-time spatter behavior characteristics is also revealed for the SLM process. The real-time analysis of the uncertainty/variation during the SLM process is made possible through in-situ x-ray characterization.

In this work, we report the sources of uncertainty in SLM due to variations from the optimized AM processing parameters for Ti6Al4V through in-situ characterization. We reveal the sensitivity of the SLM process to the processing parameters and identify the leading cause of uncertainty by quantifying the percent change in the SLM dynamics (depression zone dynamics, melt pool dynamics, and spatter dynamics) due to the four processing parameters: (1) laser beam size, (2) laser power, (3) laser scan speed, and (4) powder bed thickness. The understanding of the significance of small changes in processing parameters on SLM dynamics are determined and discussed. The uncertainty in this work is studied by making small changes with respect to the optimized processing parameter needed for Ti6Al4V under SLM AM conditions.

## **2. MATERIALS AND METHOD**

### **2.1. MATERIAL**

Ti6Al4V titanium alloy was used in this study because (1) it has good x-ray transparency, (2) it is the most commonly used titanium alloy, makes up approximately half of the share of titanium products used today [33], and (3) it is of particular interest to the aerospace, biomedical, and defense industry since it is suitable for a wide range of applications due to its characteristic high-strength and low-density material property [5]. The Ti6Al4V powders for testing was purchased from Pyrogenesis Canada Inc.

(Montreal, Québec, Canada). The Ti6Al4V metal substrate was purchased from McMaster (Elmhurst, IL, U.S.A). The powder is shown in Figure 1 under SEM to observe the shape and distribution of the two powder sizes.

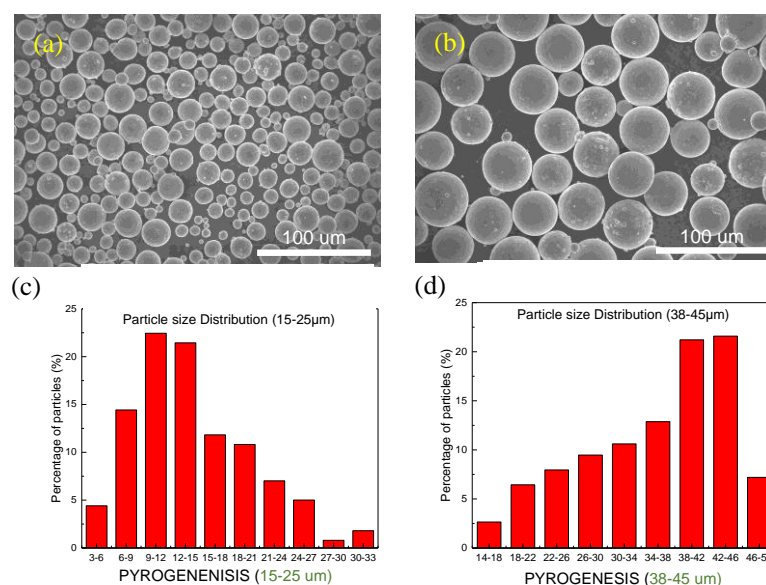


Figure 1. SEM imaging of two sizes of pyrogenesis powders with particle size distribution. SEM images (a-b) depicting the two powder sizes: 15-25 and 38-45 μm powder size. Corresponding particle size distribution (c-d) found using SEM image processing.

The Ti6Al4V grade 5 powder for both systems 15-25 μm and 38-45 μm have chemical systems containing titanium, aluminum, vanadium, and trace element compositions. The Oxygen and Nitrogen amounts vary between the two systems due to measured internal analysis using ONH-2000 by inert gas fusion. The specific chemical compositions for both powder sizes are tabulated in the Table 1 below.

Table 1. Chemical composition of Ti6Al4V.

Chemical Composition	Composition (%wt.)	
	15-25 $\mu\text{m}$	38-45 $\mu\text{m}$
Titanium	Balance	
Aluminum	5.5	
Vanadium	3.5-4.5	
Carbon	<0.08	
Oxygen	0.16	0.12
Nitrogen	0.02	0.01
Hydrogen	<0.015	
Iron	<0.40	
Other total, max	0.40	

Pyrogenesis plasma atomized powder is utilized for all processing parameter testing. Testing of laser processing parameters are all conducted using 15-25 $\mu\text{m}$  powder size. Testing of powder bed thickness is conducted at 15-25 $\mu\text{m}$  and 38-45 $\mu\text{m}$  powder size for all conditions.

## 2.2. IN-SITU HIGH-SPEED SYNCHROTRON X-RAY IMAGING EXPERIMENT

Figure. 2 illustrates the schematic of the synchrotron imaging system. A high-flux synchrotron x-ray with a first harmonic energy of 24 keV and an energy bandwidth of 5~7% was utilized to reveal the dynamics of the SLM AM process (Beam Line 32-ID-B, Advanced Photon Source, Argonne National Laboratory). The transmitted x-ray signal is

captured by a scintillator (LuAG:Ce, 100  $\mu\text{m}$  thickness), where the signal is converted into visible light and recorded by a high-speed camera (Photron FastCam SA-Z) [31]. A frame rate of 50 kHz and a camera exposure time of 1  $\mu\text{s}$  was used to capture the laser printing process. The field of view for the x-ray was 768-pixel x 512-pixel with a resolution of  $\sim 2 \mu\text{m}$  per pixel. The laser scan length was 2.5 mm. The typical sample assembly which is composed of a miniature Ti6Al4V metal substrate with a thickness of 0.40 mm, a height of 2.95 mm, and a powder bed layer thickness of 100  $\mu\text{m}$  is sandwiched between two pieces of glassy carbon, which is transparent to the incident x-ray beam. For more details about the in-situ x-ray imaging experiment, refer to previous publications [31,34–36]. Data image processing was done using ImageJ to adjust the brightness and contrast of the images to enhance the visibility of the melt pool and depression zone boundaries [37].

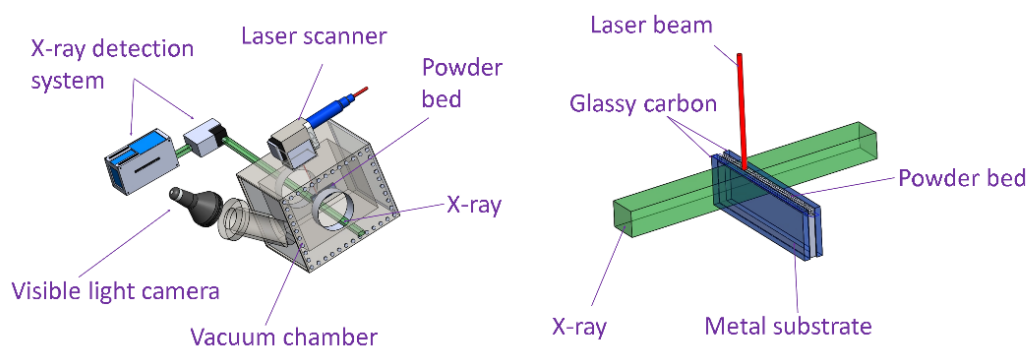


Figure 2. Schematic of the in-situ high-speed synchrotron x-ray imaging and sample assembly setup. Schematic of the in-situ x-ray imaging set-up. The x-ray passes through the sample at a perpendicular angle relative to the sample metal substrate, ending at the x-ray detection system. A visible light camera is used to ensure proper laser-sample alignment. Two glassy carbon walls are used to hold the metal substrate and the powder bed while ensuring x-ray transparency along the x-ray beam path. More details regarding in-situ high-speed synchrotron x-ray imaging available within work done by Qilin et al [38].

### 2.3. CHARACTERIZATION AND QUANTIFICATION OF THE SOURCES OF UNCERTAINTY IN SELECTIVE LASER MELTING

Figure. 3 (a) shows a schematic highlighting the major features of a substrate during laser scanning and their locations. Figure. 3 (b) highlights the various dynamics of the SLM process which are of interest: (1) 2D projection of the depression zone geometry, (2) 2D projection of the melt pool geometry, and (3) spatter behavior. The laser scanning direction shown in Figure. 4 (b) is the same for Figure. 3 (b-g). Figure. 3 (c) is the 2D projected image of the melt pool boundary, revealing the geometry of the melt pool depth and length. Figure. 3 (d) is an optical image of the top surface of the metal substrate after laser scanning which is used to measure the width of the melt pool after excess powder has been removed. Figure. 3 (e) shows the 2D projection of the depression zone geometry, revealing the depression zone depth and width. Figure. 3 (f) shows the spatter dynamics. Figure. 3 (g) depicts the solidified build track after laser scanning. The spatter diameter and volume are measured assuming a spherical spatter geometry. The spatter ejection speed and angle are measured relative to the horizontal location of the top surface of the metal substrate and the laser scanning direction.

Tracking of SLM dynamics is conducted by manual image processing and image analysis. Identification and tracking of systems such as spatter, depression zone, and melt pool dynamics are difficult to automate due to changes in the intensity during x-ray scanning. For manual analysis, all measurements are accurate to 1 pixel within the frame. All pixel displacements are equal to  $\sim 2\mu\text{m}$  giving a total dimensional accuracy down to two microns. This gives a very high accuracy of the depression zone, melt pool, and spatter dynamics. Depression zone dynamics are analyzed at every other frame when the entire region is visible within the depression zone. The width is determined to be the

region at the top of the substrate where the edges of the depression zone are vaporized due to laser heating. The depth of the depression zone is defined as the distance from the top of the substrate to the lowest point in the depression zone (deepest vaporized region within the substrate). For melt pool analysis, three conditions are analyzed and measured: the length, depth, and width are determined at every other frame ( $\sim 40\mu s$ ). The length of the melt pool is taken as the farthest liquid region ahead of the depression, to the tail or farthest region where liquid is present (edge of tail). The depth is defined as the vertical distance from the lowest melted region within the substrate to the top of melted region within the powder bed. The location within the powder bed can be manually detected due to the visible, quantifiable change in intensity from the x-ray image. The width of the melt pool is the only ex-situ analysis conducted within this work. The width of the melt pool is the vertical distance between the edges of the laser affected zone of the single line laser scanning after solidification.

Analysis of the spatter dynamics require constant frame by frame tracking to determine the spatter dynamics. Analysis of spatter dynamics are solely done for liquid spatter ejection due to the significance of liquid spatter on finalized part properties highlighted in work by Ali et al. [26]. Four main spatter dynamics are tracked: spatter ejection angle, spatter speed, spatter diameter, and spatter volume. The spatter ejection angle is defined as the angle of the spatter ejection immediately after leaving the powder bed region relative to the laser location. The laser location is defined for each spatter at the exact moment the spatter fully leaves the powder bed region and is kept constant for each unique spatter. The angle reference is coincident to the substrate region in the direction of the laser scanning.

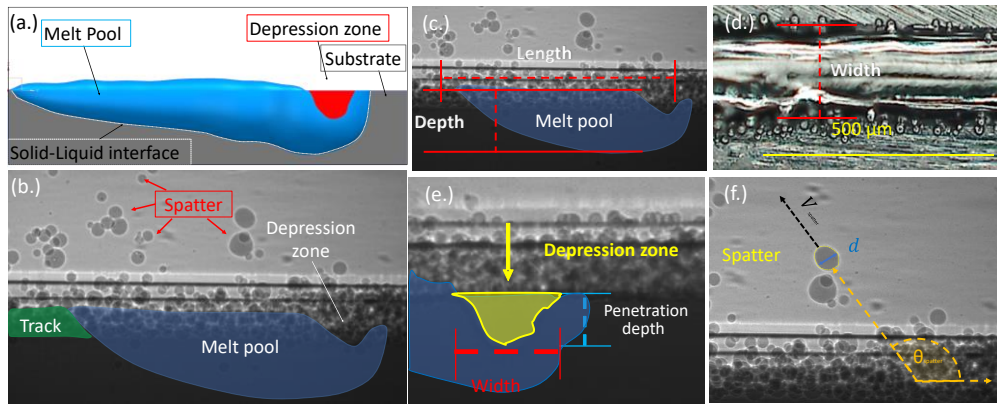


Figure 3. Dynamics of SLM. (a) Schematic outlining dynamics during laser scanning. (b) Experimental laser scanning marking elements of the SLM dynamics during laser scanning. (c) Typical melt pool length and depth dimensions. (d) Typical optical image of the melt pool width measured after laser melting and removal of excess powder. (e) Typical depression zone depth and width dimensions. (f) Typical spatter behavior indicating the spatter diameter,  $d$ , and spatter ejection angle,  $\theta$ . The spatter volume,  $V$ , is calculated assuming a spherical spatter geometry. The spatter speed,  $v$ , is calculated by determining the distance the spatter travels over a known time.

The spatter speed is the change in relative location of the spatter within the viewing window between frame changes. For this work, a 2D spatter velocity is tracked and determined due to the inability to track displacement along the x-ray penetration direction. The location of the spatter is known and tracked and the change in time between image capture is known, so the speed of liquid spatter can be determined for each spatter as

$$V_{spatter} = \frac{\sqrt{(Y_2 - Y_1)^2 + (X_2 - X_1)^2}}{t_2 - t_1} \quad (1)$$

where the second location Y coordinate  $Y_2$  and X coordinate  $X_2$  are compared to the Y  $Y_1$  and X  $X_1$  using the displacement equation in a cartesian coordinates system. The change in time is conducted using the difference between the time of frame capture  $t$  for each coordinate. Spatter diameter is

$$d = \frac{d_{vertical} + d_{horizontal}}{2} \quad (2)$$

where the average of the vertical diameter  $d_{vertical}$  and horizontal diameter  $d_{horizontal}$  is used to determine an accurate spatter diameter. The spatter diameter is determined after spatter has left the powder bed region. The volume of the spatter is determined by the summation of all liquid spatter for each processing condition during testing. Simply, the spatter volume is

$$v_{spatter} = \sum_{i=1}^n \left( \left( \frac{\pi}{6} \right) d_n^3 \right) \quad (3)$$

where the summation of all  $n$  number of spatters using the diameter  $d$ . For testing a spherical geometry is assumed to calculate the volume of spatter produced. The ability to capture the spatter, melt pool, and depression zone dynamics are made capable by high-speed, high-resolution x-ray imaging for precise tracking for all processing parameters.

Table 2 summarizes the processing parameters used in this work. The optimized processing parameters needed for Ti6Al4V under SLM conditions are indicated by the 0% change. Table 1 also details the variations in the processing parameters from the optimized parameters that were studied, along with the percent change in the parameters relative to the optimized parameter (0% change). In this work, we measure and quantify the dynamics of Ti6Al4V under SLM conditions. The characteristic dimensions and quantities of the SLM dynamics are measured for each of the processing parameter conditions. The average value and standard deviation of the characteristic dimensions and quantities are shown in Figures four through seven, while the percent change relative to the average measurements made at the optimized processing parameters for Ti6Al4V under SLM AM conditions are summarized in the Table below.

Table 2. Experimental processing parameters for SLM Ti6Al4V.

Variation in laser beam size							
Beam size, $D$ (um)	Focal plane, $d$ (mm)	Power, $P$ (W)	Scan speed, $V$ (m/s)	Thickness, $t$ (mm)	Scan length, $l$ (mm)	Powder layer Thickness, $t$ (um)	Beam size percent change (%)
80	-2						-11
85	-2.25						-6
88	-2.4						-2
90	-2.5	364	0.9	0.4	3	100	0
92	-2.6						2
95	-2.75						6
100	-3						11
Variation in laser power							
Beam size, $D$ (um)	Focal plane, $d$ (mm)	Power, $P$ (W)	Scan speed, $V$ (m/s)	Thickness, $t$ (mm)	Scan length, $l$ (mm)	Powder layer Thickness, $t$ (um)	Power percent change (%)
		345.8					-5
		356.72					-2
90	-2.5	364	0.9	0.4	3	100	0
		371.28					2
		382.2					5
Variation in laser scan speed							
Beam size, $D$ (um)	Focal plane, $d$ (mm)	Power, $P$ (W)	Scan speed, $V$ (m/s)	Thickness, $t$ (mm)	Scan length, $l$ (mm)	Powder layer Thickness, $t$ (um)	Scan speed percent change (%)
			0.855				-5
			0.882				-2
90	-2.5	364	0.9	0.4	3	100	0
			0.918				2
			0.945				5
Variation in Powder bed thickness							
Beam size, $D$ (um)	Focal plane, $d$ (mm)	Power, $P$ (W)	Scan speed, $V$ (m/s)	Powder size (um)	Powder layer Thickness, $t$ (um)	Scan length, $l$ (mm)	Powder bed average change (um)
				15-25	50		50
				15-25	100		0
90	-2.5	260	1.0	38-45	50	3	-50
				38-45	100		0

## 2.4. SELECTION OF UNCERTAINTY PROCESSING CONDITIONS

The four processing conditions were specifically selected within this work to determine their effects on the SLM dynamics. The laser power, scan speed, powder bed thickness, and beam size are among the most manipulated processing conditions in commercial AM to manipulate finalized part quality. Additionally, these four processing parameters can have intrinsic uncertainty during AM manufacturing due to inherent

product drift, part design, part size, or inherent preparation and deposition uncertainty.

Fig. 4 depicts the 4 processing parameters and demonstrates the justification for determining the effects on the SLM dynamics.

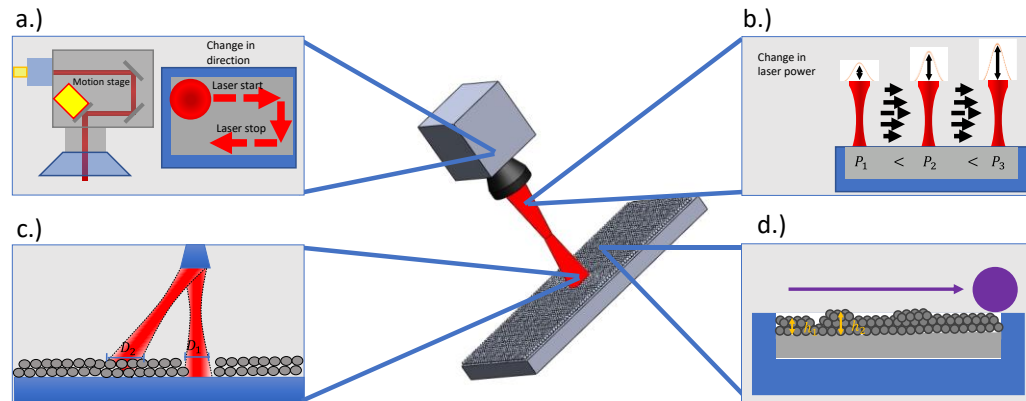


Figure 4. Process uncertainty causes. (a) demonstrates the changes in laser scan speed due to intrinsic drift and laser scan strategy. (b) schematically depicts intrinsic laser power drift apparent in commercial AM laser systems. (c) Gives a visual representation of natural beam size fluctuation inherent in large build systems due to increased focal distance on build edge locations. (d) visually represents powder thickness fluctuations due to inconsistent powder flowability and spreading resulting in non-uniform feedstock deposition.

Laser power and scan speed fluctuations generate inherent fluctuations within a single AM system despite pre-set operating conditions due to intrinsic parameter drift as seen in Figure 4 (a-b). These inherent drifts are depicted in work by Moges et al. and highlighted in research by Lopez et al. The characterization of inherent variation is demonstrated through a full factorial design of experiments assuming normal distributions on nominal values of laser power and laser scan speed. These findings give statistically driven system parameter fluctuation that naturally occur in commercial AM processing [27,28]. Scan speed variation, however, is commonly extrinsically influenced

primarily by the system scan strategy. Introducing scan strategies with laser start, stop, and directional changes during the active laser scanning generate regions with sudden variations in operating laser scan speeds due to acceleration changes in the scanning mirror. Work by Jia et al. demonstrates unique scan strategies that implement directional changes during laser scanning, causing sudden acceleration or deceleration at start and stop locations. Primarily, this problem has been solved by increased understanding and g-code manipulation to maintain consistent scan speed velocities but are still apparent in some scanning strategies[29]. Laser beam size fluctuation is common in large scale powder bed manufacturing due to rigid build platforms. The resulting laser at regions far from the laser origin impact the powder surface at a greater distance, increasing the distance of the laser focal point location relative to the heating region. Work by ayoola et al. demonstrate this phenomenon of beam size manipulation in conduction welding when operating near build platform edges[30]. Powder bed thickness fluctuation is largely driven by the inconsistent flowability conditions of commercial powder leading to reductions in build height and bed density [31]. Work by Jacob et al. demonstrated a measurement procedure to capture the powder bed density and discovered a ~20% fluctuation in the powder bed density along the spreading area. Work by Dowling et al. expands on powder bed fluctuations involving powder size, size distribution, and density; results highlight the uncertainty in AM processing and effects on final part properties[32]. These natural and extrinsic variations in the laser power, scan speed, powder bed thickness, and beam size demonstrate the importance of identifying, understanding, and mitigating the uncertainty in SLM.

### 3. RESULTS AND DISCUSSION

#### 3.1. LASER BEAM SIZE

Figure. 5 shows the change in SLM dynamics induced by altering the laser beam size during SLM of Ti6Al4V. Figure. 5 (a-b) shows the changes in the depression zone depth and width due to the change in the laser beam size. Figure. 5 (c-e) depicts the change in melt pool length, depth, and width due to the change in laser beam size. Figure. 5 (f-i) demonstrates the changes in the spatter dynamics due to change in beam size. Noticeable trends are highlighted and marked in red. Testing is all conducted with 15-25 $\mu\text{m}$  size plasma atomized powder.

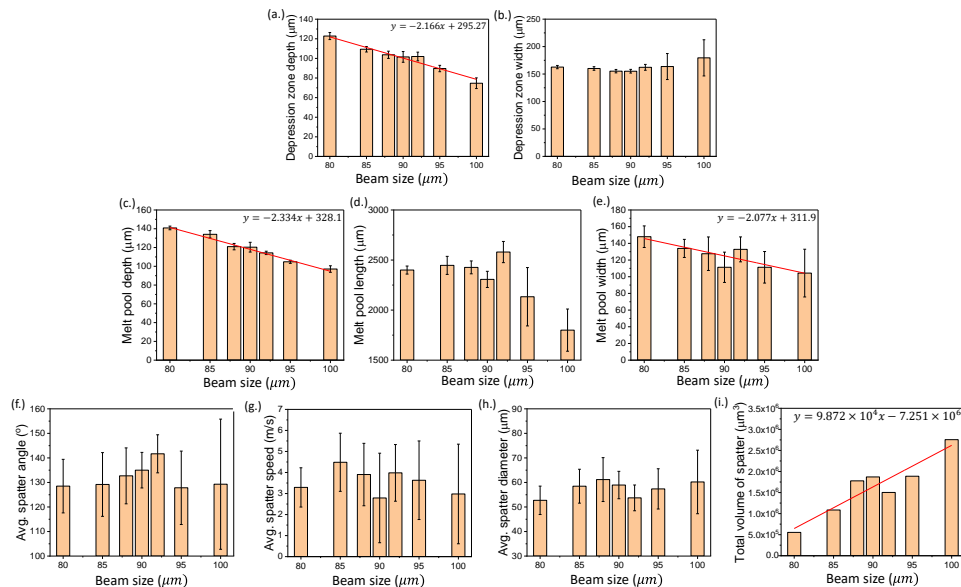


Figure 5. Variation in the SLM dynamics due to variation in the laser beam size for Ti6Al4V. (a-b) shows the changes in the depression zone depth and width due to variation in the laser beam size. (c-e) shows the variation of the melt pool depth, length, and width due to variations in laser beam size. (f-i) shows the variation in the spatter average direction, speed, diameter, and total volume due to change in the laser beam size. All testing is conducted using 15-25 $\mu\text{m}$ , plasma atomized Ti6Al4V powder.

The results in Figure. 5 (a) indicate that an increase in the laser beam size will result in a decrease in the depression zone depth. A linear trend between the laser beam size and the depression zone depth with a slope of -2.17 was observed. No distinct trend for the change in the depression zone width based on variations in the laser beam size was defined from Figure. 5 (b). Within the range of laser beam sizes that were studied, the standard deviation of the depression zone width at each of the seven beam sizes increases significantly once increased at and above 95 $\mu\text{m}$ . The standard deviation remains uniform for depression zone depth across the various laser beam sizes. The standard deviation indicates the stability of the depression zone geometry at each laser beam size. A large standard deviation means that there is an instability in the depression zone geometry, resulting in fluctuations during laser scanning. Conversely, a small standard deviation indicates stability in the depression zone. The increasing laser beam size greater than 92 $\mu\text{m}$  generated substantial fluctuation to multiple SLM dynamics marking an instability being present in the depression zone. Previous work by Suzuki et al. demonstrated the effect of alteration of deposited energy density on respective material properties. Their study related the energy intensity of the system to be effected by the inverse laser beam size to the square root of the third power, demonstrating the analytical significance in beam size on system intensity[24]. Beam size results experimentally demonstrated this work, showing a decrease in the laser beam size can lead to a larger penetration depth of the laser without decreasing the depression zone fluctuation during laser scanning.

Figure. 5 (c-e) shows that an increase in the laser beam size will result in a decreasing trend in the melt pool dynamics. A linear trend between the laser beam size

and the melt pool dynamics with a slope of -2.334 and -2.077 was observed for the melt pool depth and width respectively. An increase in the laser beam size increases the heating region of the laser, reducing the maximum localized energy deposition. This decrease in the energy deposition results in changes in the melt pool geometry and is reflected in the data. An increase in the laser beam size leads to a decrease in the melt pool depth and width. A trend in the melt pool length due to a change in the laser beam size was not observed. However, the standard deviation of the melt pool length at the larger beam sizes (95  $\mu\text{m}$  and 100  $\mu\text{m}$ ) is significantly larger than the standard deviations at the smaller laser beam sizes (<95  $\mu\text{m}$ ). As the beam size increases and the localized intensity decreases, there is not sufficient energy to maintain a consistent melt pool shape and results in a fragmentation or fluctuation of the melt pool length.

The results in Figure. 5 (f-i) depict the effects of varying beam size on the overall spatter dynamics. Within the range of testing, the spatter average diameter, max diameter, and direction was not significantly or noticeably influenced by the change in the laser beam size. The increase in beam size, however, led to an increase in the total amount of spatter volume. The change in the laser beam size caused increases or reduction of the spatter production by 47 and 70% respectively. Work by Liu et al. correlated the effects of the beam size, power, and scan speed effect on the spatter generation. Specifically, the reduction in the beam size dependent energy density led to a reduction of noticeable spatter in high-speed optical imaging [33]. Spatter changes, due to small changes in processing variations, appears to be significantly driven by the laser beam size fluctuations. An increased beam size increases the heat affected zone of the laser with a reduced laser intensity. The increased region reduces the amount of total energy

absorptivity within the central powder location, reducing the powder-to-powder cohesivity without reducing the laser output. The decreased laser intensity in the expanded region generated an increased zone for the production of liquid spatter to formulate and escape without proper substrate fusion.

Table 3. Percent change in SLM dynamics induced by variations in laser beam size during laser scanning.

<b>Beam size: depression zone dynamics</b>					
Beam size, $D$ (um)	Beam size percent change	Depth percent change (%)	Width percent change (%)		
80	-11	20.98	4.86		
85	-6	7.73	3.22		
88	-2	2.15	0.08		
90	0		0		
92	2	0	4.58		
95	6	-0.43	5.51		
100	11	-11.66	15.71		
		-26.43			
<b>Beam size: melt pool dynamics</b>					
Beam size, $D$ (um)	Beam size percent change	Depth percent change (%)	Length percent change (%)	Width percent change (%)	
80	-11	17.04	4.05	32.93	
85	-6	11.4	6.07	20.31	
88	-2	0.49	5.20	14.62	
90	0	0	0	0	
92	2	-5.05	11.85	19.3	
95	6	-12.92	-7.51	0.003	
100	11	-19.33	-21.97	-6.26	
<b>Beam size: spatter dynamics</b>					
Beam size, $D$ (um)	Beam size percent change	Ejection angle percent change (%)	Ejection speed percent change (%)	Spatter diameter percent change (%)	Spatter volume percent change (%)
80	-11	-4.81	-17.34	-10.57	-70.37
85	-6	-4.32	12.81	-0.82	-21.93
88	-2	-1.71	-2.01	3.76	-4.95
90	0	0	0	0	0
92	2	4.94	-8.79	-8.88	-19.68
95	6	-5.32	-25.13	-2.67	0.93
100	11	-4.24	-29.9	2.12	47.33

The small variations in the laser beam size led to significant influence on the overall SLM dynamics. Laser beam size increases reduced the overall laser intensity.

This reduction causes significant changes, greater than the induced fluctuation,

throughout laser scanning. Specifically, the depression zone depth, melt pool depth, melt pool width, and spatter volume had identifiable, linear trends produced by varying the laser beam size greater than the small variations to the processing parameter. The effective change of the SLM dynamics due to changes in the laser beam size are depicted in Table 3.

### 3.2. LASER POWER

Figure. 6 shows the change in SLM dynamics induced by altering the laser power during SLM of Ti6Al4V. Figure. 6 (a-b) shows the changes in the depression zone depth and width due to the change in the laser power. Figure. 6 (c-e) depicts the change in melt pool length, depth, and width due to the change in laser power. Figure. 6 (f-i) demonstrates the changes in the spatter dynamics due to change in laser power. Testing is all conducted with 15-25 $\mu$ m plasma atomized powder.

For both the depression zone depth and width in Figure. 6 (a-b), an overall increasing trend was observed due to an increase in the laser power. A linear trend between the laser power and the depression zone dynamics with a slope of  $0.6451 \frac{\mu m}{W}$  and  $0.4620 \frac{\mu m}{W}$  was observed for the depression zone depth and width, respectively. Similar results obtained by Yin et al. were discovered while utilizing in-situ optical imaging techniques at a much wider testing range. Testing at 750W to 1550 W significantly altered the depression zone depth, width, and profile[34]. This work expands on the work of Yin et al. demonstrating at minute increase to the laser power still leads to a significant heat input into the powder and substrate materials, creating a larger depression cavity

region. For both the depression zone depth and width, the standard deviation width at each laser power increment were similar.

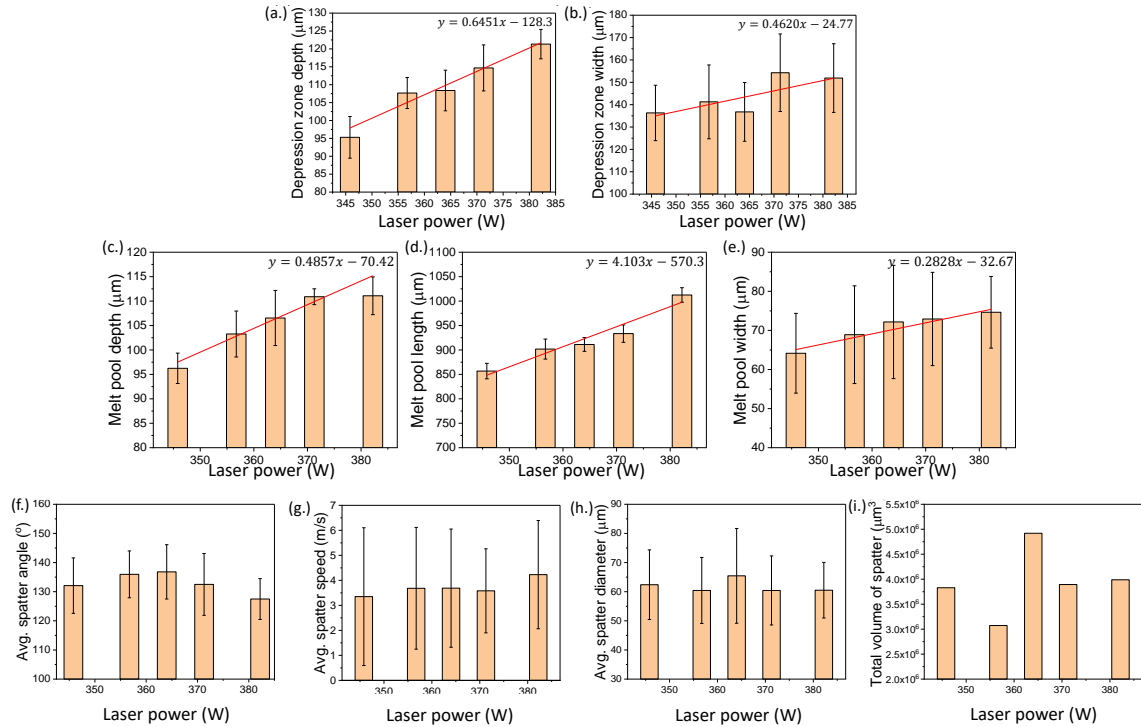


Figure 6. Variation in the SLM dynamics due to variation in the laser power for Ti6Al4V. (a-b) shows the changes in the depression zone depth and width due to variation in the laser power. (c-e) shows the variation of the melt pool depth, length, and width due to variations in laser power. (f-i) shows the variation in the spatter average direction, speed, diameter, and total volume due to change in the laser power. All testing is conducted using 15-25 $\mu\text{m}$ , plasma atomized Ti6Al4V powder.

Figure. 6 (c-e) show that an increase in the laser power leads to an increase in the melt pool geometry. A linear trend with a slope of  $0.4857 \frac{\mu\text{m}}{\text{W}}$ ,  $4.103 \frac{\mu\text{m}}{\text{W}}$ , and  $0.2828 \frac{\mu\text{m}}{\text{W}}$  were observed for the melt pool depth, length, and width respectively. These trends are guided by increased absorptivity of the laser and efficiency with increasing laser power. Work by Lane et al. demonstrated the transient laser energy absorption and its

significance to laser power. Testing demonstrated that an increase in laser output increased the coupling efficiency, manipulating the depression zone geometry and causing an increase in overall absorption for both bare plate and powder models[35]. Testing conducted with significantly smaller variation in the laser power experimentally demonstrate the in-situ manipulation of laser power on melt pool dynamics. As the laser power increases, the system absorptivity increases alongside the total energy into the material, expanding the volume of melted material. A higher laser power allows for the formation of melt pools that are deeper, wider, and longer during the SLM process.

Figure. 6 (f-i) depict the spatter dynamics due to variations in the laser power during laser scanning. The spatter average diameter, direction, speed, and volume were determined. Within the range of testing, no significant trends were depicted on the spatter dynamics due to the small alterations in the laser power. For the laser power, the speed and diameter of the spatter had the greatest fluctuations for all testing conditions.

Changes in laser power had significant changes on the overall SLM dynamics. The increase in the laser power has a direct effect to the laser intensity impacting the powder bed system, causing significant changes of the geometry to occur. Specifically, the depression zone and melt pool dynamics had changes statistically higher than the variation in the laser power. The exact percent changes in the SLM dynamics are categorized and given in Table 4.

Table 2. Percent change in SLM dynamics induced by variations in the laser power during scanning.

<b>Laser Power: depression zone dynamics</b>				
Laser power, P (W)	Power percent change (%)	Depth percent change (%)	Width percent change (%)	
345.8	-5	-12.07	-0.34	
356.72	-2	-0.65	3.28	
364	0	0	0	
371.28	2	5.82	12.80	
382.2	5	11.96	11.05	

<b>Laser power: melt pool dynamics</b>				
Laser power, P (W)	Power percent change (%)	Depth percent change (%)	Length percent change (%)	Width percent change (%)
345.8	-5	-9.66	-5.98	-11.10
356.72	-2	-3.08	-1.04	-4.52
364	0	0	0	0
371.28	2	-4.08	2.43	1.05
382.2	5	4.27	11.11	3.43

<b>Laser power: spatter dynamics</b>					
Laser power, P (W)	Power percent change (%)	Ejection angle percent change (%)	Ejection speed percent change (%)	Spatter diameter percent change (%)	Spatter volume percent change (%)
345.8	-5	-15.68	-9.22	-15.68	-22.17
356.72	-2	-16.44	-0.18	-16.44	-37.55
364	0	0	0	0	0
371.28	2	-8.36	-2.93	-8.36	-20.86
382.2	5	-12.9	14.64	-12.9	-18.93

### 3.3. LASER SCAN SPEED

Figure. 6 shows the change in SLM dynamics induced by altering the laser scan speed during SLM of Ti6Al4V. Figure. 6 (a-b) shows the changes in the depression zone depth and width due to the change in the laser power. Figure. 7 (c-e) depicts the change in melt pool length, depth, and width due to the change in laser scan speed. Figure. 7 (f-i) demonstrates changes in the spatter dynamics due to the change in laser scan speed.

Testing is all conducted with 15-25 $\mu$ m plasma atomized powder.

Figure. 7 (a-b) shows that an overall decreasing trend was observed for the depression zone depth and width due to an increase in the laser scan speed. For the depth and width dimensions, a linear trend between the laser scan speed and the depression

zone dynamics with a slope of  $-186.1 \frac{\mu m \cdot s}{m}$  and  $-87.32 \frac{\mu m \cdot s}{m}$  was observed respectively. An increase in the laser scan speed reduces the total laser intensity as discussed by Boswell et al. being inputted into the powder and substrate materials[36]. This phenomenon is demonstrated in a previous work by Cunningham et al. over a wide range of processing speeds for bare plate testing. Cunningham et al. utilized high speed x-ray imaging to capture the location and penetration depth of the laser; variations in scan velocities from 0.4 to 1.2 m/s demonstrated significant changes to the size, shape, and specification (conduction to keyhole transformation) of the depression zone [37]. The standard deviation of the depression zone depth and width at each of the laser scan speed increments were similar, meaning that the fluctuation from the average depression zone depth and width value at each laser scan speed were not statistically affected by the change in laser scan speed.

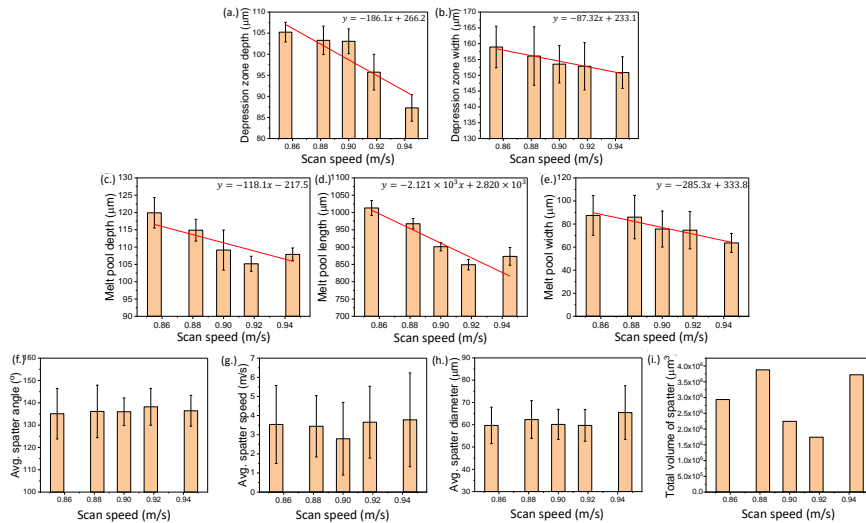


Figure 7. Variation in the SLM dynamics due to variation in the laser scan speed for Ti6Al4V. (a-b) shows the changes in the depression zone depth and width due to variation in the laser scan speed. (c-e) shows the variation of the melt pool depth, length, and width due to variations in laser scan speed. (f-i) shows the variation in the spatter average direction, speed, diameter, and total volume due to change in the laser scan speed. All testing is conducted using 15-25 $\mu$ m, plasma atomized Ti6Al4V powder.

Figure. 7 (c-e) shows that an increase in the laser scan speed leads to a decrease in the melt pool geometry. A decreasing trend with a slope of  $-118.1 \frac{\mu m \cdot s}{m}$ ,  $-2121 \frac{\mu m \cdot s}{m}$ , and  $-285 \frac{\mu m \cdot s}{m}$  was observed for the melt pool depth, length, and width respectively. Testing revealed no statistical trend in the melt pool dynamics fluctuations with changes in laser scan speed within the testing range. Work by Dilip et al. demonstrated the effective change in scan speed to the resulting melt pool geometry utilizing optical micrographs. Scanning speeds ranging from 500 to 1200 mm/s revealed significant decreases in the melt pool depth and width; High scan speeds at lower powers were also demonstrated to generate scanning systems too weak for proper melt pool formation, leading to balling on the substrate surface [6]. Experimental testing with changes at or under 6% were demonstrated within the results to maintain the systems dynamics by significantly affecting the melt pool geometry. As the laser scan speed increases, the laser interaction time decreases and leads to a decrease in the energy deposition. This decrease in the energy deposition means that there is less material being melted or fused together, resulting in a smaller melt pool.

Figure. 7 (f-i) depicts the effect of the spatter dynamics due to the changes in the laser scan speed. The spatter's direction, speed, average diameter, and volume were observed and determined for the entire range of the laser scan speed. The spatter dynamics did not have any significant change directly influenced and observed by the laser scan speed within the range of testing.

The laser scan speed had similar effects on the SLM dynamics as the laser power. An increase in laser scan speed noticeably decreased the depression zone and melt pool geometries during laser scanning. The alteration in scan speed produced linear trends on

changes to the SLM dynamics. More specifically, the variation in the SLM dynamics produced changes greater (>2x) than that of the experimental changes in the laser scan speed. The specific effects of changing the laser scan speed within the range of testing and the percent change in the SLM dynamics are categorized within Table 5.

Table 3. Percent change in SLM dynamics induced by variations in the laser scan speed.

<b>Laser scan speed: depression zone dynamics</b>					
Laser scan speed, V (m/s)	Scan speed percent change (%)	Depth percent change (%)	Width percent change (%)		
0.855	-5	2.1	3.53		
0.882	-2	0.22	1.67		
0.9	0	0	0		
0.918	2	-7.1	-0.43		
0.945	5	-15.32	-1.73		
<b>Laser scan speed: melt pool dynamics</b>					
Laser scan speed, V (m/s)	Scan speed percent change (%)	Depth percent change (%)	Length percent change (%)	Width percent change (%)	
0.855	-5	9.86	12.43	-15.58	
0.882	-2	5.26	7.36	13.64	
0.9	0	0	0	0	
0.918	2	-3.64	-5.77	-1.29	
0.945	5	-1.15	-3.1	-15.91	
<b>Laser scan speed: spatter dynamics</b>					
Laser scan speed, V (m/s)	Scan speed percent change (%)	Ejection angle percent change (%)	Ejection speed percent change (%)	Spatter diameter percent change (%)	Spatter volume percent change (%)
0.855	-5	-0.66	26.86	-0.77	31
0.882	-2	0.1	23.46	3.62	73
0.9	0	0	0	0	0
0.918	2	1.62	31.1	-0.74	-22
0.945	5	0.3	35.56	-8.83	66

### 3.4. POWDER BED THICKNESS

Figure. 8 shows the change in SLM dynamics induced by altering the powder bed thickness during SLM of Ti6Al4V. Figure. 8 (a-b) shows the changes in the depression zone depth and width due to the change in the powder bed thickness. Figure. 8 (c-f) demonstrates changes in the spatter dynamics due to the change in laser scan speed.

Specifically, the changes in the direction, average diameter, max diameter, and volume of spatter. Testing is conducted with 15-25 $\mu\text{m}$  and 38-45 $\mu\text{m}$  plasma atomized powders.

Figure. 8 (a-b) depicts the depression zone dynamics change due to the alteration in the powder bed thickness. Both saw large increases in both the depression zone depth and width due to a reduction in the powder bed thickness. 15-25 $\mu\text{m}$  powder experienced an increase of 55.6% and 33.18% for the depression zone depth and width respectively due to the 50 $\mu\text{m}$  reduction; 38-45 $\mu\text{m}$  powder saw an increase in the 33.18% and 54.59% for the depth and width respectively. The standard deviation in the depression depth and width was not significantly affected by the powder bed thickness fluctuation. Work by Savalani et al. conducted extensive work demonstrating the sensitivity of powder bed thickness variation of magnesium powders at <40  $\mu\text{m}$  build heights. Savalani et al. demonstrated the effects of layer thickness on post process conditions, decreasing the oxidation while increasing the surface roughness due to an increase in thickness[38]. Results in Figure 8 experimentally demonstrate the SLM dynamic changes during the laser melting process. The results demonstrate that the reduction of powder under the same laser processing conditions leads to a decrease in the overall powder being melted and fused to the substrate. This change, however, does not statistically vary greater than the manipulated processing conditions.

Figure. 8 (c-f) demonstrates the effect of the spatter dynamics due to changes in the powder bed thickness. The spatters geometry was statistically unaffected by the change in the powder bed thickness. The decrease in the powder bed thickness, however, increased the average spatter direction angle for both powder sizes changing the ejection

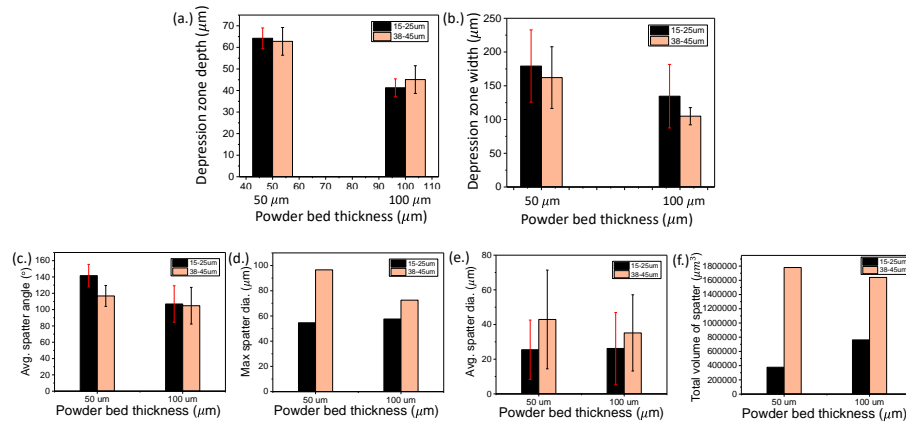


Figure 8. Variation in the SLM dynamics due to variation in the powder bed thickness for Ti6Al4V. (a-b) shows the changes in the depression zone depth and width due to variation in the powder bed thickness. (c-f) shows the variation in the spatter average direction, max diameter, diameter, and total volume due to change in the powder bed thickness. Testing is conducted using 15-25 $\mu\text{m}$  and 38-45 $\mu\text{m}$ , plasma atomized Ti6Al4V powder.

angle of liquid spatter produced at lower powder bed sizes. The fluctuation or variation in the spatter dynamics did not have any significant impact to the spatter volume production when the powder bed thickness was altered. The powder size, however, demonstrated an increase by up to four times the total volume due to changing the powder size from 15-25 $\mu\text{m}$  to 38-45 $\mu\text{m}$ . Work by Zhang et al. highlights the significance in powder size on inter-particle laser reflectivity. Increases in laser heating generated by additional surfaces for laser contact with smaller powder sizes[39]. This phenomenon increases the cohesivity by laser melting of surrounding particles within the substrate, reducing spatter ejection with small powder size.

Altering the powder bed thickness had a substantial change on the overall SLM dynamics. Primarily, the change in the powder bed thickness altered the depression zone depth and length. The decrease in the powder bed thickness decreases the affected powder during laser scanning. The decreased powder volume expanded the energy

inputted into the substrate, increasing the depth and length of the vaporized region of the depression zone. The specific changes to the SLM dynamics induced by the powder bed thickness are categorized on Table 6.

Table 4. Percent change in SLM dynamics induced by variations in the powder bed thickness.

<b>Powder bed thickness: depression zone dynamics</b>					
Powder bed size and thickness ( $\mu\text{m}/\mu\text{m}$ )	Scan speed percent change (%)	Depth percent change (%)	Width percent change (%)		
15-25 / 100	0	0	0		
15-25 / 50	50	55.61	33.18		
38-45 / 100	0	0	0		
38-45 / 50	50	39.32	54.59		
<b>Powder bed thickness: spatter dynamics</b>					
Powder bed size and thickness ( $\mu\text{m}/\mu\text{m}$ )	Scan speed percent change (%)	Ejection angle percent change (%)	Ejection speed percent change (%)	Spatter diameter percent change (%)	Spatter volume percent change (%)
15-25 / 100	0	0	0	0	0
15-25 / 50	50	32.49	-5.21	-2.75	-34.08
38-45 / 100	0	0	0	0	0
38-45 / 50	50	11.44	33.06	22.06	7.88

### 3.5. SENSITIVITY ANALYSIS OF PROCESSING CONDITIONS

Testing of process sensitivity is vital in SLM due to the current repeatability limitations compared to conventional methods. Work by Yadav et al. and Dowling et al. outline the critical importance and necessity for limiting the variables of uncertainty and repeatability respectively to tackle the challenges of AM and bring it towards legacy manufacturing techniques [40,41]. Works by Kusuma et al., Nguyen et al., and Hanzl et al. discuss in detail the effects of significant processing parameter variation on finalized part properties [17,23,42]. This work induced small parameter variations to critical processing conditions, revealing the sensitivity of the in-situ SLM dynamics on systems where intrinsic process variation is present, demonstrating the limitation of current

practices attempting to obtain near perfect part-to-part repeatability. Testing of small variations demonstrated unique processing condition sensitivity. Powder bed thickness variation sensitivity was found to be close to reasonably expected, roughly affecting the SLM dynamics by the same amount as the percent variation in processing. The other 3 processing parameters: laser power, scan speed, and beam size behaved unexpectedly, producing changes to the system outside the expectations of energy density or current methods. Laser beam size changes no greater than 11% had effective changes up to two times greater in the depression zone and melt pool dynamics. Demonstrating systems with large build platforms being susceptible to changes in solidification rates at regions located far from the laser location, changing the localized microstructure, and expected properties of the finalized part. The laser beam size also had a substantial impact on the spatter volume, demonstrating the importance of the spatter control on the impact of the laser beam size and shape compared to power or scan speed. The laser power demonstrates, similarly, that changes of only 5% off the control parameter tested caused changes over twice the parameter fluctuation for all the depression zone and melt pool dynamics. Current systems operating in ideal conditions seeing part reproducibility issues may be apparent due to intrinsic laser power drift within their system causing significant changes to the underlying SLM dynamics. The effects of the laser scan speed, however, was determined to be the most significantly influential parameter for part manufacturing. Scan speed variations of 5% generated up to three times greater depression zone and melt pool fluctuations. This demonstrates the importance of controlling all extrinsic conditions in scan strategy to reduce the overall scan speed fluctuations. This also shows the significance of a controllable, highly influential processing condition that laser scan

speed plays in part control and why many works highlighted by Jia et al. utilize scan strategies to control the finalized part properties. Understanding the significance and impact of parameter fluctuations allows the implementations and advancement of control techniques necessary for AM part reliability. Even though these are the most manipulated processing conditions, identifying all sensitive processing conditions and techniques to mitigate or eliminate them are vital for obtaining process control and reproducibility in additively manufactured products.

#### 4. CONCLUSIONS

In this work, the sources of uncertainty in the SLM process, for Ti6Al4V, due to variations in the processing conditions (laser power, scan speed, beam size, and powder bed thickness) were observed, analyzed, and characterized. The effects on the depression zone, melt pool, and spatter dynamics were quantified with in-situ x-ray imaging. The effects of small changes in processing conditions, that can occur involuntarily in commercial processing, are discovered, and characterized based on the most detrimental effect processing parameters on in-situ process control of SLM dynamics. The major conclusions are marked below.

- The testing of small changes in influential AM processing conditions are justified and discussed on their effects to the SLM dynamics utilizing in-situ x-ray imaging. Testing of changes for laser beam size, laser power, laser scan speed, and powder bed thickness being changed by small amounts that can occur during commercial part to part fabrication are demonstrated to experimentally quantified.

- Small changes in laser beam size (<12%) from optimized processing conditions produce significant changes (~2X) on the SLM depression zone and melt pool dynamics. Laser beam size also strongly influences the production of liquid spatter, causing changes up to 70% in the total spatter volume production, signifying the most influential processing parameter for spatter control commercial AM.
- Laser power fluctuations of 5% or less generated changes greater than twice the change in the parameter. Specifically, the laser power fluctuation directly affects all depression zone and melt pool dynamics, changing the melting region, solidification rate, and process stability with small changes in the laser power intensity.
- Laser scan speed generated the most substantial impact on the depression zone and melt pool dynamics. Scan speed fluctuations at or below 5% caused up to 15% changes in the depression zone and melt pool dynamics. The control of the laser scan speed during AM processing is vital to limit the most influential processing condition in the production of AM part property uncertainty.
- Laser powder bed thickness fluctuations demonstrated a roughly equivalent effect to fluctuations to the SLM dynamics. The powder bed thickness primarily controls the layer-by-layer deposition height and did not statistically have an unexpected change to the system dynamics. The increase in powder size, however, showed a sudden increase in the liquid spatter volume production due to reductions in the interparticle reflections of nearby powders, reducing the overall particle to particle adhesion within the powder bed. The change in powder size can increase the spatter volume up to four times the original powder spatter production.

## ACKNOWLEDGEMENTS

The authors would like to thank Alex Deriy and Niranjan Parab at the APS for their help on the beamline experiments. This research used resources of the Advanced Photon Source, a U.S. Department of Energy (DOE) Office of Science User Facility operated for the DOE Office of Science by Argonne National Laboratory under Contract No. DE-AC02-06CH11357. This work is funded by the National Science Foundation. This work also received funding from the Boeing Company through the Center for Aerospace Manufacturing Technology (CAMT) at Missouri University of Science and Technology, with special thanks to Amaka Ibeh, Fatmata Barrie, and James Castle.

## BIBLIOGRAPHY

- [1] T. DebRoy, H.L. Wei, J.S. Zuback, T. Mukherjee, J.W. Elmer, J.O. Milewski, A.M. Beese, A. Wilson-Heid, A. De, W. Zhang, Additive manufacturing of metallic components – Process, structure and properties, *Prog. Mater. Sci.* 92 (2018) 112–224. <https://doi.org/10.1016/j.pmatsci.2017.10.001>.
- [2] L. Thijs, F. Verhaeghe, T. Craeghs, J. Van Humbeeck, J.P. Kruth, A study of the microstructural evolution during selective laser melting of Ti-6Al-4V, *Acta Mater.* 58 (2010) 3303–3312. <https://doi.org/10.1016/j.actamat.2010.02.004>.
- [3] D. Wang, W. Dou, Y. Yang, Research on selective laser melting of Ti6Al4V: Surface morphologies, optimized processing zone, and ductility improvement mechanism, *Metals (Basel)*. 8 (2018). <https://doi.org/10.3390/met8070471>.
- [4] J. Ciurana, L. Hernandez, J. Delgado, Energy density analysis on single tracks formed by selective laser melting with CoCrMo powder material, *Int. J. Adv. Manuf. Technol.* 68 (2013) 1103–1110. <https://doi.org/10.1007/s00170-013-4902-4>.

- [5] T. Peng, C. Chen, Influence of energy density on energy demand and porosity of 316L stainless steel fabricated by selective laser melting, *Int. J. Precis. Eng. Manuf. - Green Technol.* 5 (2018) 55–62. <https://doi.org/10.1007/s40684-018-0006-9>.
- [6] J.J.S. Dilip, S. Zhang, C. Teng, K. Zeng, C. Robinson, D. Pal, B. Stucker, Influence of processing parameters on the evolution of melt pool, porosity, and microstructures in Ti-6Al-4V alloy parts fabricated by selective laser melting, *Prog. Addit. Manuf.* 2 (2017) 157–167. <https://doi.org/10.1007/s40964-017-0030-2>.
- [7] M. Narvan, K.S. Al-Rubaie, M. Elbestawi, Process-structure-property relationships of AISI H13 tool steel processed with selective laser melting, *Materials (Basel)*. 12 (2019) 1–20. <https://doi.org/10.3390/ma12142284>.
- [8] F. Mazzucato, D. Forni, A. Valente, E. Cadoni, Laser metal deposition of inconel 718 alloy and as-built mechanical properties compared to casting, *Materials (Basel)*. 14 (2021) 1–21. <https://doi.org/10.3390/ma14020437>.
- [9] A. Azarniya, X.G. Colera, M.J. Mirzaali, S. Sovizi, F. Bartolomeu, M. k. St Weglowski, W.W. Wits, C.Y. Yap, J. Ahn, G. Miranda, F.S. Silva, H.R. Madaah Hosseini, S. Ramakrishna, A.A. Zadpoor, Additive manufacturing of Ti–6Al–4V parts through laser metal deposition (LMD): Process, microstructure, and mechanical properties, *J. Alloys Compd.* 804 (2019) 163–191. <https://doi.org/10.1016/j.jallcom.2019.04.255>.
- [10] S. Liu, Y.C. Shin, Additive manufacturing of Ti6Al4V alloy: A review, *Mater. Des.* 164 (2019) 107552. <https://doi.org/10.1016/j.matdes.2018.107552>.
- [11] T. Majumdar, T. Bazin, E.M.C. Ribeiro, J.E. Frith, N. Birbilis, Understanding the effects of PBF process parameter interplay on Ti-6Al-4V surface properties, *PLoS One*. 14 (2019) 1–24. <https://doi.org/10.1371/journal.pone.0221198>.
- [12] H. Shipley, D. McDonnell, M. Culleton, R. Coull, R. Lupoi, G. O'Donnell, D. Trimble, Optimisation of process parameters to address fundamental challenges during selective laser melting of Ti-6Al-4V: A review, *Int. J. Mach. Tools Manuf.* 128 (2018) 1–20. <https://doi.org/10.1016/j.ijmachtools.2018.01.003>.
- [13] A. Saboori, D. Gallo, S. Biamino, P. Fino, M. Lombardi, An overview of additive manufacturing of titanium components by directed energy deposition: Microstructure and mechanical properties, *Appl. Sci.* 7 (2017). <https://doi.org/10.3390/app7090883>.

- [14] S. Rawal, J. Brantley, N. Karabudak, Additive manufacturing of Ti-6Al-4V alloy components for spacecraft applications, in: RAST 2013 - Proc. 6th Int. Conf. Recent Adv. Sp. Technol., IEEE, 2013: pp. 5–11.  
<https://doi.org/10.1109/RAST.2013.6581260>.
- [15] A. Cutolo, B. Neirinck, K. Lietaert, C. de Formanoir, B. Van Hooreweder, Influence of layer thickness and post-process treatments on the fatigue properties of CoCr scaffolds produced by laser powder bed fusion, *Addit. Manuf.* 23 (2018) 498–504. <https://doi.org/10.1016/j.addma.2018.07.008>.
- [16] S. Dadbakhsh, L. Hao, Effect of layer thickness in selective laser melting on microstructure of Al/5 wt.%Fe<sub>2</sub>O<sub>3</sub> powder consolidated parts, *Sci. World J.* 2014 (2014). <https://doi.org/10.1155/2014/106129>.
- [17] Q.B. Nguyen, D.N. Luu, S.M.L. Nai, Z. Zhu, Z. Chen, J. Wei, The role of powder layer thickness on the quality of SLM printed parts, *Arch. Civ. Mech. Eng.* 18 (2018) 948–955. <https://doi.org/10.1016/j.acme.2018.01.015>.
- [18] H.W. Mindt, M. Megahed, N.P. Lavery, M.A. Holmes, S.G.R. Brown, Powder Bed Layer Characteristics: The Overseen First-Order Process Input, *Metall. Mater. Trans. A Phys. Metall. Mater. Sci.* 47 (2016) 3811–3822.  
<https://doi.org/10.1007/s11661-016-3470-2>.
- [19] L.E. Criales, Y.M. Arsoy, T. Özel, Sensitivity analysis of material and process parameters in finite element modeling of selective laser melting of Inconel 625, *Int. J. Adv. Manuf. Technol.* 86 (2016) 2653–2666.  
<https://doi.org/10.1007/s00170-015-8329-y>.
- [20] L. Ma, J. Fong, B. Lane, S. Moylan, J. Filliben, A. Heckert, L. Levine, Using design of experiments in finite element modeling to identify critical variables for laser powder bed fusion, *Proc. - 26th Annu. Int. Solid Free. Fabr. Symp. - An Addit. Manuf. Conf. SFF 2015.* (2020) 219–228.
- [21] T.T. Roehling, S.S.Q. Wu, S.A. Khairallah, J.D. Roehling, S.S. Soezeri, M.F. Crumb, M.J. Matthews, Modulating laser intensity profile ellipticity for microstructural control during metal additive manufacturing, *Acta Mater.* 128 (2017) 197–206. <https://doi.org/10.1016/j.actamat.2017.02.025>.
- [22] Q. Han, H. Gu, R. Setchi, Discrete element simulation of powder layer thickness in laser additive manufacturing, *Powder Technol.* 352 (2019) 91–102.  
<https://doi.org/10.1016/j.powtec.2019.04.057>.

- [23] C. Kusuma, S.H. Ahmed, A. Mian, R. Srinivasan, Effect of Laser Power and Scan Speed on Melt Pool Characteristics of Commercially Pure Titanium (CP-Ti), *J. Mater. Eng. Perform.* 26 (2017) 3560–3568. <https://doi.org/10.1007/s11665-017-2768-6>.
- [24] A. Suzuki, R. Nishida, N. Takata, M. Kobashi, M. Kato, Design of laser parameters for selectively laser melted maraging steel based on deposited energy density, *Addit. Manuf.* 28 (2019) 160–168. <https://doi.org/10.1016/j.addma.2019.04.018>.
- [25] A.M. Khorasani, I. Gibson, U.S. Awan, A. Ghaderi, The effect of SLM process parameters on density, hardness, tensile strength and surface quality of Ti-6Al-4V, *Addit. Manuf.* 25 (2019) 176–186. <https://doi.org/10.1016/j.addma.2018.09.002>.
- [26] U. Ali, R. Esmailizadeh, F. Ahmed, D. Sarker, W. Muhammad, A. Keshavarzkermani, Y. Mahmoodkhani, E. Marzbanrad, E. Toyserkani, Identification and characterization of spatter particles and their effect on surface roughness, density and mechanical response of 17-4 PH stainless steel laser powder-bed fusion parts, *Mater. Sci. Eng. A.* 756 (2019) 98–107. <https://doi.org/10.1016/j.msea.2019.04.026>.
- [27] T. Moges, P. Witherell, G. Ameta, On characterizing uncertainty sources in laser powder bed fusion additive manufacturing models, *ASME Int. Mech. Eng. Congr. Expo. Proc.* 2A-2019 (2019) 1–15. <https://doi.org/10.1115/IMECE2019-11727>.
- [28] F. Lopez, P. Witherell, B. Lane, Identifying uncertainty in laser powder bed fusion additive manufacturing models, *J. Mech. Des. Trans. ASME.* 138 (2016) 1–4. <https://doi.org/10.1115/1.4034103>.
- [29] H. Jia, H. Sun, H. Wang, Y. Wu, H. Wang, Scanning strategy in selective laser melting (SLM): a review, *Int. J. Adv. Manuf. Technol.* 113 (2021) 2413–2435. <https://doi.org/10.1007/s00170-021-06810-3>.
- [30] W.A. Ayoola, W.J. Suder, S.W. Williams, Effect of beam shape and spatial energy distribution on weld bead geometry in conduction welding, *Opt. Laser Technol.* 117 (2019) 280–287. <https://doi.org/10.1016/j.optlastec.2019.04.025>.
- [31] A.B. Spierings, M. Voegtlin, T. Bauer, K. Wegener, Powder flowability characterisation methodology for powder-bed-based metal additive manufacturing, *Prog. Addit. Manuf.* 1 (2016) 9–20. <https://doi.org/10.1007/s40964-015-0001-4>.
- [32] G. Jacob, A. Donmez, J. Slotwinski, S. Moylan, Measurement of powder bed density in powder bed fusion additive manufacturing processes, *Meas. Sci. Technol.* 27 (2016). <https://doi.org/10.1088/0957-0233/27/11/115601>.

- [33] Y. Liu, Y. Yang, S. Mai, D. Wang, C. Song, Investigation into spatter behavior during selective laser melting of AISI 316L stainless steel powder, *Mater. Des.* 87 (2015) 797–806. <https://doi.org/10.1016/j.matdes.2015.08.086>.
- [34] J. Yin, D. Wang, L. Yang, H. Wei, P. Dong, L. Ke, G. Wang, H. Zhu, X. Zeng, Correlation between forming quality and spatter dynamics in laser powder bed fusion, *Addit. Manuf.* 31 (2020) 100958. <https://doi.org/10.1016/j.addma.2019.100958>.
- [35] B. Lane, I. Zhirnov, S. Mekhontsev, S. Grantham, R. Ricker, S. Rauniyar, K. Chou, Transient Laser Energy Absorption, Co-axial Melt Pool Monitoring, and Relationship to Melt Pool Morphology, *Addit. Manuf.* 36 (2020) 101504. <https://doi.org/10.1016/j.addma.2020.101504>.
- [36] J. Boswell, J. Jones, N. Barnard, D. Clark, M. Whittaker, R. Lancaster, The effects of energy density and heat treatment on the microstructure and mechanical properties of laser additive manufactured Haynes 282, *Mater. Des.* 205 (2021) 109725. <https://doi.org/10.1016/j.matdes.2021.109725>.
- [37] R. Cunningham, C. Zhao, N. Parab, C. Kantzos, J. Pauza, K. Fezzaa, T. Sun, A.D. Rollett, Keyhole threshold and morphology in laser melting revealed by ultrahigh-speed x-ray imaging, *Science* (80-. ). 363 (2019) 849–852. <https://doi.org/10.1126/science.aav4687>.
- [38] M.M. Savalani, J.M. Pizarro, Effect of preheat and layer thickness on selective laser melting (SLM) of magnesium, *Rapid Prototyp. J.* 22 (2016) 115–122. <https://doi.org/10.1108/RPJ-07-2013-0076>.
- [39] J. Zhang, D. Gu, Y. Yang, H. Zhang, H. Chen, D. Dai, K. Lin, Influence of Particle Size on Laser Absorption and Scanning Track Formation Mechanisms of Pure Tungsten Powder During Selective Laser Melting, *Engineering.* 5 (2019) 736–745. <https://doi.org/10.1016/j.eng.2019.07.003>.
- [40] P. Yadav, O. Rigo, C. Arvieu, E. Le Guen, E. Lacoste, In situ monitoring systems of the SLM process: On the need to develop machine learning models for data processing, *Crystals.* 10 (2020) 1–26. <https://doi.org/10.3390/cryst10060524>.
- [41] L. Dowling, J. Kennedy, S. O’Shaughnessy, D. Trimble, A review of critical repeatability and reproducibility issues in powder bed fusion, *Mater. Des.* 186 (2020) 108346. <https://doi.org/10.1016/j.matdes.2019.108346>.
- [42] P. Hanzl, M. Zetek, T. Bakša, T. Kroupa, The influence of processing parameters on the mechanical properties of SLM parts, *Procedia Eng.* 100 (2015) 1405–1413. <https://doi.org/10.1016/j.proeng.2015.01.510>.

### III. THE EFFECT OF PARTICLE SIZE DISTRIBUTION WITH EFFICIENT PACKING ON ADDITIVE MANUFACTURING POWDER FLOWABILITY AND SELECTIVE LASER MELTING

Zachary Young<sup>1,2</sup>, Minglei Qu<sup>2,3</sup>, Meelap M. Coday<sup>1,2,3</sup>, Qilin Guo<sup>2,3</sup>, S. Mohammad H. Hojjatzadeh<sup>1,2,3</sup>, Luis I. Escano<sup>2</sup>, Kamel Fezzaa<sup>4</sup> Lianyi Chen<sup>1,2,3\*</sup>

<sup>1</sup>Department of Mechanical and Aerospace Engineering, Missouri University of Science and Technology, Rolla, Missouri 65409, USA.

<sup>2</sup>Department of Mechanical Engineering, University of Wisconsin-Madison, Madison, Wisconsin 53706, USA.

<sup>3</sup>Department of Materials Science and Engineering, University of Wisconsin-Madison, Madison, Wisconsin 53706, USA.

<sup>4</sup>X-ray Science Division, Advanced Photon Source, Argonne National Laboratory, Lemont, Illinois, 60439, USA.

\*Correspondence to: Lianyi Chen ([lianyi.chen@wisc.edu](mailto:lianyi.chen@wisc.edu)).

#### ABSTRACT

Powder based additive manufacturing (AM) contains tremendous uncertainty in commercial applications during powder spreading and overall powder bed quality, leading to problems in repeatability and overall quality of the AM developed products. This work focuses on identifying the uncertainty due to particle size distribution (PSD) on the resulting Ti6Al4V powder's flowability. Specifically, one of the main sources of uncertainty is due to the Powder size ratio creating highly dense, low flowability powder beds at unique powder ratios. Identifying the uncertainty allows powder size distribution manipulation in real applications to alter the properties or prevent failure of powder spreading in AM. The work showed that the PSDs effect on flowability is not linear,

rather the PSDs near local high packing densities cause significant reductions in overall flowability. The location of dense packing regions were found using D.B. Miracle's dense packing formula to determine high density powder bed locations depending on the size of a two powder system. The flowability is tested using a Mercury Scientific revolution powder analyzer to quantify the changes in the powder during hundreds of avalanches on each powder size distribution. The PSDs effects on the part properties are identified through the identification of changes in the Selective laser melting (SLM) dynamics using in-situ high speed x-ray imaging to observe the internal dynamics during the melting process. The testing concluded that operating at or near the dense packing ratios for the powder bed system led to sudden increase in the avalanche angle and break energy of the powder bed, reducing the flowability of the system compared to all other PSDs. The conclusion further demonstrated the effect of dense packing on the final part fabrication process, most notably causing a sudden increase in the build height of systems using the dense packing PSDs. This work looks deeper into the cause of PSD's effects on the flowability, and AM dynamics of parts compared with previous works. The work determines one of the causes of uncertainty induced by PSDs during additive manufacturing by determining and experimentally demonstrating the effect of two powder dense packing systems inducing sudden changes on the overall flowability of the powder and resulting SLM dynamics. The variation in powder flowability and SLM dynamics due to changes in PSD determined in this work are vital for understanding the uncertainty of powder spreading in commercial AM and improving the quality of additively manufactured parts.

**Keywords:** Flowability; Particle size distribution; additive manufacturing; optimization of material properties

## 1. INTRODUCTION

Powder based additive manufacturing uses a powder feedstock (bed or deposition) to deposit material for laser melting during part fabrication[1–5]. Unfortunately, the resulting part quality using this method are not as reliable or repeatable as commonplace conventional methods. A main issue for non-uniformity of part quality is due to powder size distribution (PSD). Uncertainty in PSD in commercial manufacturing leads to reduction in quality and repeatability for powder spreading and deposition[3,6,7]. Previous works have investigated the effects of varying powder size distribution on the resulting material properties[1,7–11]. Variations in PSD has been found to have effects on the resulting physical, surface, and mechanical properties[6,7,12–17]. Testing has also been found that changes from a homogenous powder to non-homogeneous powders results in an overall reduction in the powder's flowability[18,19].

Previous works have identified the importance of PSD on the powder flowability and resulting material properties. Liu et al. has conducted work highlighting the effects of isolating two PSDs: a narrow, near homogenous, PSD and a wider, heterogeneous, PSD with near identical average powder size[20]. The work concluded changes to PSD effecting powder bed flowability, part density, hardness, and surface finishes with similar average powder sizes. Work by Meier et al. utilized discrete element method (DEM) to study the frictional, rolling, and cohesive forces of powder layers and their effect on

adhesion and uniformity of various powders and distributions in additively manufactured parts[21]. Work by Ma et al. tested a wide range of PSD of alumina powders to investigate the finalized sintering characteristics[22]. This work discovered increases in densification rates and grain growth through broadening of the PSD during laser sintering. However, their work could not accurately define optimum PSD outside of narrow, near homogenous, distribution due to the greater control and reliability of microstructure control of powder compacts. A recent work by Bai et al. identifies the effects of PSD on binder jetting additive manufacturing using a bimodal powder mixture at 73-27/ 27-73 weight ratios to obtain high density powder beds[23]. Their work identified numerous benefits to bimodal powder mixing in AM binder jet printing of copper in terms of the sintering density and flowability. These works determined numerous effects of operating at expanded PSDs and what effects that have on physical properties, flowability, and capabilities of powder mixing. These works, however, have not identified the causes of reduced capabilities and uncertainties of varying PSDs in commercial SLM manufacturing or given in-situ analysis of their effects on Ti6Al4V SLM dynamics.

A system to generate efficient atomic packing of a two powder/particle system is proposed by D.B. Miracle et al.[11,20]. The method used a unique PSD with a system of any two particles at precise ratios to promote atomic dense packing of powder systems. One of the powders acts as a central particle with the most efficient three-dimensional packing of satellite particles (second powder) in contact with the single central particle. This technique generates an efficient packing system to get the greatest bulk density when there is mixing of two powder sizes.

Previous works have identified various advantages and disadvantages to operating powder-based systems with varying PSDs. This includes the effects on flowability, surface properties, mechanical properties, and repeatability. Previous works, however, have not determined the causes of sudden changes in flowability during commercial SLM AM processing that led to failures during part manufacturing. The works have also not identified the uncertainties causing physical property variation between part-to-part manufacturing which limit the commercial use of varying PSDs in commercial settings. Current works have not linked a cause to this uncertainty for Ti6Al4V powders that lead to layer-by-layer deposition uncertainty. The works have also not experimentally observed the effective changes in the SLM dynamics of systems with varying PSDs, specifically, on powders with densely packed powder systems.

This work incorporates D.B. Miracle's research to determine the effect that the dense packing and varying PSDs of a two powder mixture have on the resulting flowability and SLM dynamics of Ti6Al4V. The work investigates flowability characteristics of two powder sizes mixed at various PSDs and, more specifically, at D.B. Miracle's dense packing ratios to see if non-homogenous powders flow differently from a single mixture of powders. The resulting PSDs are tested utilizing high speed x-ray imaging to experimentally determine the effects that varying the PSD have on the SLM dynamics of Ti6Al4V. These findings identify if sudden failures in commercial AM processing result in localized regions of dense powder clustering during the AM powder spreading process and determine the effect that dense powder clustering have on SLM dynamics. The goal of this work is to determine the sources of the uncertainty between

commercially employed powders that lead to the reductions in part quality and capabilities in a wider range of commercial applications.

## **2. MATERIALS AND METHODS**

### **2.1. POWDER AND PARTICLE SIZE DISTRIBUTION**

Powder size distribution testing was conducted using two plasma atomized powders from Pyrogenesis. The size specifications were  $\sim 15\text{-}25\mu\text{m}$  (small) and  $\sim 38\text{-}45\mu\text{m}$  (large) according to manufacturer specifications. Scanning electron microscope (SEM) imaging was conducted to ensure the powder size lied within  $D_{50}$  specifications. Testing looked at hundreds of individual powders within multiple SEM images to determine an accurate histogram of the particle size variation provided in Figure 1.

The two powder sizes are mixed to create four additional particle size distributions. Mixing was conducted by a Turbula mixer to ensure proper mixing. The four additional powders were set based on weight percentages of small powder within the larger powder at 10, 30, 70, and 90 percent. The newly mixed powders were observed under SEM imaging and an analysis of hundreds of individual powders were conducted to generate an accurate histogram of the particle size variation shown in Figure 2. The resulting distributions are acceptable to see the effects of flowability within experimentally used powders in AM.

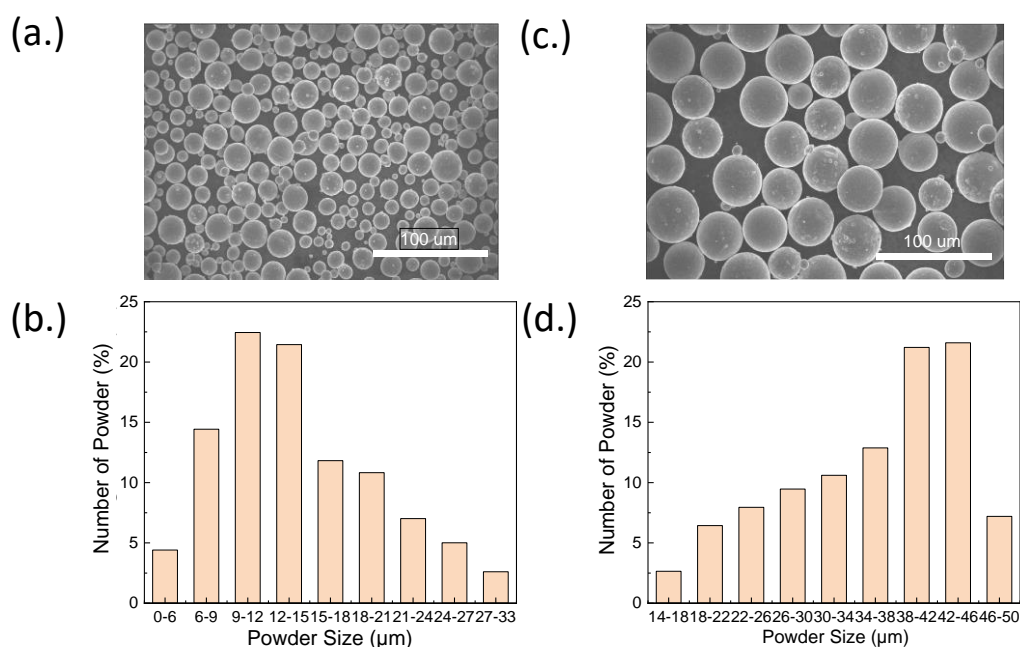


Figure 1. SEM images and histogram of particle size pyrogenesis powder was used for testing with two powder designated size ranges: 15-25 $\mu\text{m}$  (a-b) and 35-48 $\mu\text{m}$  (c-d) from the manufacturer specifications. (a, c) show a single image captured using SEM of powder feedstock material. SEM images of powder were used to determine the size distribution shown in the histograms (b, d).

The 6 PSDs were tested using SEM imaging to produce accurate models of their particle size distribution. Work conducted by Spierings et al. and numerous powder-based research utilize mathematical representative models such as grain size distributions to give an accurate model for the PSDs[25,26]. The powders grain size distributions were calculated for the 6 PSDs utilizing  $D_{10}$ ,  $D_{30}$ ,  $D_{50}$ ,  $D_{70}$ , and  $D_{90}$  distributions to give an accurate representative model. The resulting grain size distribution are provided in Table 1.

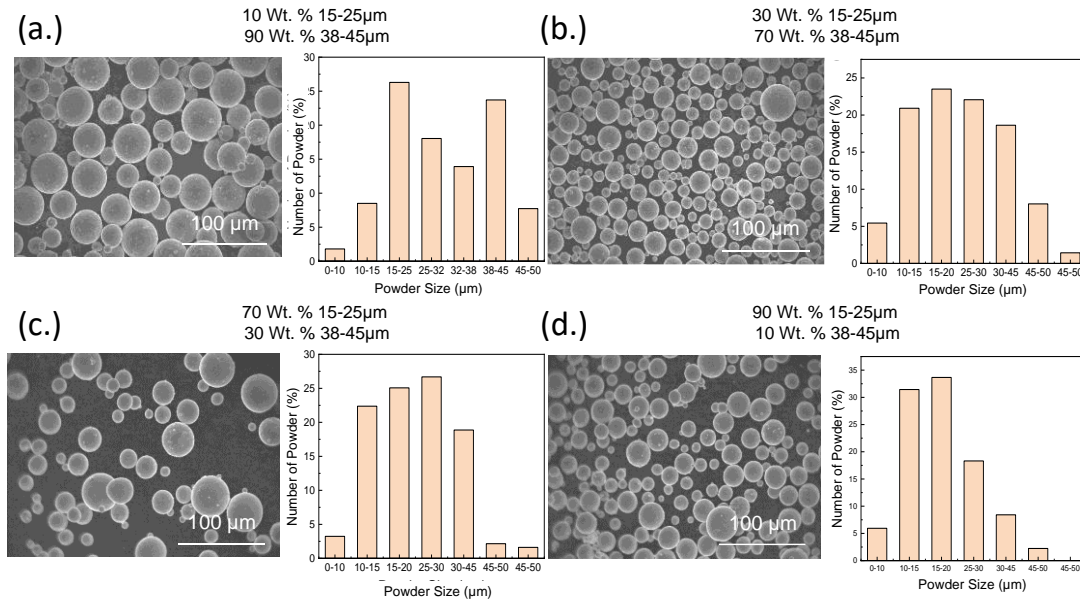


Figure 2. SEM images and histogram of particle size distributions 4 powder size distributions were created by mixing different weight percentages of 15-25µm and 38-45µm powders: 10% wt. 15-25µm (a), 30 wt. % 15-25µm (b), 70 wt. % 15-25µm (c), and 90 wt. % 15-25µm (d). All size distributions are optically depicted through SEM images and histograms were generated to display size distributions.

Table 1. PSDs Powder grain size distributions.

Powder grain size distribution	Ti6Al4V 15-25µm powder mixed into powder bed					
	0%	10%	30%	70%	90%	100%
	15-25µm	15-25µm	15-25µm	15-25µm	15-25µm	15-25µm
$D_{10}$	22.36	14.77	11.71	11.94	10.92	7.38
$D_{30}$	31.53	22.59	16	15.94	14	10.31
$D_{50}$	37.55	30.32	20.32	19.94	16.51	12.98
$D_{70}$	41.44	38.5	24.71	23.81	19.5	16.92
$D_{90}$	44.85	43.85	30.74	27.94	25	22.1

## 2.2. EFFICIENT PARTICLE PACKING

The particle size distributions at 10 and 90 percent of small powder mixed with large powder were created to generate the highest packing density with the powder sizes.

The ratio is explained by D.B. Miracles work on atomic packing density[11,20] to generate the highest density of satellite particles clustered around a central particle as seen in Figure 3.

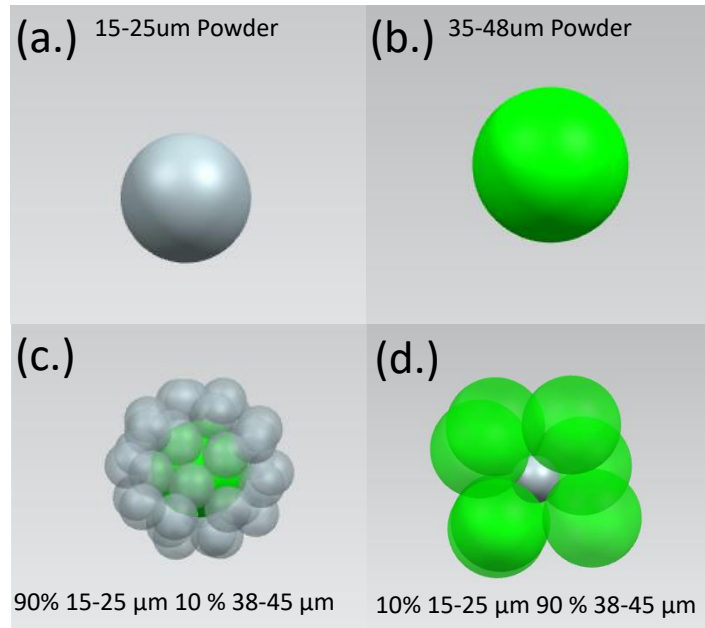


Figure 3. 3D representation of atomic packing method D.B. Miracle's model of dense sphere packing for 15-25um(a) and 38-45um(b) particle distributions. Two theoretical dense packing models can be produced: (c) 15-25um powders packed around a central 38-45um powder, (d) 38-45um powder packed around a central 15-25um powder. The first packing model has the greatest packing efficiency and can produce the densest packing method for the two powder sizes.

To determine the packing density, the two powder size variances were averaged for calculation of the mixing. The final weight percentages were rounded to the nearest 10% due to the powder variance. The powder ratio was determined depending on the ratio  $R$  of the central powder  $r_i$  to the satellite powders  $r_j$ . Three equations are utilized in the determination of satellite powders surrounding a central powder due to ratio  $R$ . The

resulting  $N^T$  is the full and partial  $r_j$  powders that can be theoretically placed around the central  $r_i$  powder. The equation can be simplified to determine the integer amount  $N$  of satellite powders  $r_j$  capable of being placed around the central powder  $r_i$ . The resulting relationship is converted to weight percentages to determine the small and large powder ratios. Additional information regarding the methodology to the dense packing system can be found within the works of Miracle et al. [27,28].

$$N^T = \begin{cases} \frac{4\pi}{\left( \left( 6 \arccos^{\frac{1}{2}} \left[ \sin\left(\frac{\pi}{3}\right) \{1-1/(R+1)^2\} \right] - \pi \right) \right)} & \text{for } 0.225 \leq R < 0.414, \\ \frac{4\pi}{\left( \left( 8 \arccos^{\frac{1}{2}} \left[ \sin\left(\frac{\pi}{4}\right) \{1-1/(R+1)^2\} \right] - 2\pi \right) \right)} & \text{for } 0.414 \leq R < 0.902, \\ \frac{4\pi}{\left( \left( 10 \arccos^{\frac{1}{2}} \left[ \sin\left(\frac{\pi}{5}\right) \{1-1/(R+1)^2\} \right] - 3\pi \right) \right)} & \text{for } 0.902 \leq R. \end{cases} \quad (1)$$

### 2.3. FLOWABILITY TESTING

Analysis was completed using powder revolution to determine the flowability factors. Testing was conducted on A Mercury Scientific Revolution Powder analyzer. Flowability factors such as break energy and avalanche angle were determined. All tests were done with single batch of each commercial grade powder for multiple iterations and averaged to give accurate flowability properties. The powder analyzer uses visible light camera to capture the powder dynamics during rotation as shown in Figure 4.

Flowability required the creation of ~250g of each PSD for accurate testing. The various PSDs were mixed with a Turbula mixture for uniform powder systems. Once mixed the PSDs are placed within the cylindrical testing drum inside the Mercury powder analyzer. Vibrations are conducted to identify changes in the effective density recorded at

one to two second intervals. The density change is done by capturing volume changes of a powders known mass using the system's visible light camera. Once vibrations have completed, the cylindrical testing drum rotates. The system captures the angle of the powder surface (relative to the center to tip of the slope) forming along the rotating wall. After hundreds of avalanches, the system calculates the average on the flowability characteristics of the powder system.

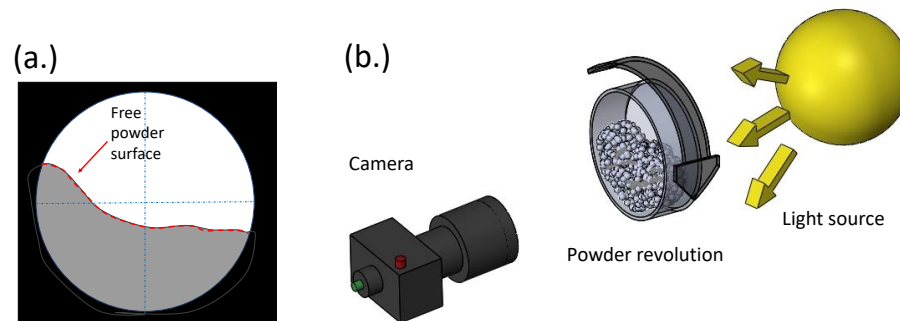


Figure 4. Schematic of powder revolution. A Mercury Scientific Revolution powder analyzer is used for the analysis of flowability properties of powder with varying particle size distributions throughout testing. The free powder surface (a) is tracked under hundreds of revolutions to accurately capture and quantify flowability characteristics. The analyzer uses a light source and visible light camera to capture events during powder dynamics (b). Captured images are used to determine avalanche angle and break energy of the powder dynamics.

Testing was conducted to determine two flowability characteristics: Avalanche angle and the break energy. Work conducted by Nalluri et al. demonstrates the effects of the avalanche angle and break energy on the resulting flowability of powder bed systems. Nalluri's work demonstrated the relationship of powder flowability with a commercially available flow testing instrument and demonstrated the correlation of avalanche angle and break energy effects on the flowability of powder bed systems[29]. Additional work by Hancock et al. demonstrates robust procedure and methodology for avalanche testing

instrumentation[30]. The avalanche angle is the average angle of the powder the moment before an avalanche occurs. Specifically, the avalanche angle is the moment the powder buildup along the cylindrical wall during revolution gives out, causing the powder to avalanche. The break energy is the maximum energy of the powder prior to the avalanche minus the energy of the powder prior to beginning of powder rotation. The break energy is defined as the difference of the total powder energy before and after an avalanche occurs. The total powder energy is determined as the location of the pixel relative to the bottom of the sample. The potential energy  $U_{pixel}$  of a pixel is defined as

$$U_{pixel}(mj) = M_{pixel}(kg) * H_{pixel}(m) * G \left( \frac{m}{s^2} \right) * 1000. \quad (2)$$

where the height  $H_{pixel}$  of each pixel is multiplied by the gravitational constant and mass of the individual pixel. The mass of a pixel  $M_{pixel}$  from visible light camera is defined as

$$M_{pixel} = \left( \frac{M_{total}}{V_{total}} \right) * V_{pixel} \quad (3)$$

where  $V_{total}$  and  $V_{pixel}$  are the volumes of the total powder system and individual pixel respectively. The cumulative total of the powder and its location within the cylinder defines the total potential energy of the powder system.

Testing the systems apparent and vibrational density were conducted to determine the static density of the various PSDs. Apparent density is determined within Mercury Scientific powder revolution analyzer utilizing equation (3) to determine the Mass and volume of the powder bed system. The packed density was determined using a built-in system within the powder revolution analyzer. Testing conducted powder vibration constantly and recording the change in the powder bed volume. After roughly 7.45 minutes of cyclical vibration the final post vibration density was determined. The

Hausner ratio was determined for all 6 PSDs using the apparent and post-vibration densities. The Hausner ratio is defined as the ratio between the tapped density to the apparent density of the powder. The determined static flowability properties are provided within Table 2 below.

Table 2. PSDs static density calculations.

Powder Size distribution (% 15-25 $\mu$ m)	Density and Hausner ratio		
	Apparent density, $\rho_{apparent}$ (g/cc)	Density after vibration, $\rho_{vibration}$ (g/cc)	Hausner ratio, $\frac{\rho_{apparent}}{\rho_{vibration}}$
0	2.45	2.66	1.09
10	2.49	2.74	1.10
30	2.43	2.65	1.09
70	2.33	2.61	1.12
90	2.33	2.66	1.14
100	2.5	2.66	1.06

Density testing demonstrated the highest apparent density was 2.5g/cc at 100% 15-25 $\mu$ m powder. The greatest post vibration density occurred at 10% 15-25 $\mu$ m powder with a density of 2.74g/cc. The second greatest post density vibration were tied between the 0%, 90%, and 100% powder size distributions at 2.66g/cc. The greatest Hausner ratio is 1.14 at 90% 15-25 $\mu$ m powder. Generally, powders having poor flowability are defined at increased Hausner ratios. 10% and 90% 15-25 $\mu$ m powder is conducted at dense packing ratios according to work by Miracle et al. and have the greatest effects on the post vibration density and Hausner ratios respectively. Testing of dynamic flow through powder revolution testing is conducted to determine the effects of localized dense packing dynamic powder flow capabilities.

## 2.4. IN-SITU SELECTIVE LASER MELTING DYNAMICS

The change in the powder size distribution leads to a non-homogenous powder bed system during additive manufacturing. Selective laser melting (SLM) is conducted under high speed in-situ x-ray imaging to determine the effects caused by changes in PSD. Testing is conducted with a high-flux synchrotron x-ray with a first harmonic energy of 24 keV and an energy bandwidth of 5~7% (Beam Line 32-ID-B, Advanced Photon Source, Argonne National Laboratory). A scintillator (LuAG:Ce, 100  $\mu\text{m}$  thickness) is used to capture the x-ray signal where the signal is converted into visible light and recorded by a high-speed camera (Photron FastCam SA-Z) [21]. A frame rate of 50 kHz and a camera exposure time of 1  $\mu\text{s}$  was used to capture the laser printing process. The field of view for the x-ray was 768 pixel x 512 pixel with a resolution of  $\sim 2$   $\mu\text{m}$  per pixel. The laser scan length was 2.5 mm. The typical sample assembly which is composed of a miniature Ti6Al4V metal substrate with a thickness of 0.40 mm, a height of 2.95 mm, and a powder bed layer thickness of 100  $\mu\text{m}$  is sandwiched between two pieces of glass carbon, which is transparent to the incident x-ray beam.

The effect of PSD was focused on 4 main SLM dynamics: depression zone, melt pool, spatter, and build track. Figure. 5 (a) shows an experimental high speed x-ray imaging highlighting the SLM dynamics. Figure. 5 (b) highlights the shape and fluctuations in the scan track after laser scanning and solidification. Figure. 5 (c) demonstrates a 2D projected image of the depression zone location and geometry. Figure. 5 (d) outlines the 2D projected spatter dynamics produced during SLM: spatter size, velocity, volume, and direction. Depression zone, melt pool, and spatter dynamics are 2D projections determined with in-situ high speed imaging of selective laser melting of

Ti6Al4V. Scan track geometry is determined using pre and post x-ray imaging of SLM. Spatter diameter and volume are measured assuming a spherical geometry relative to the 2D projection.

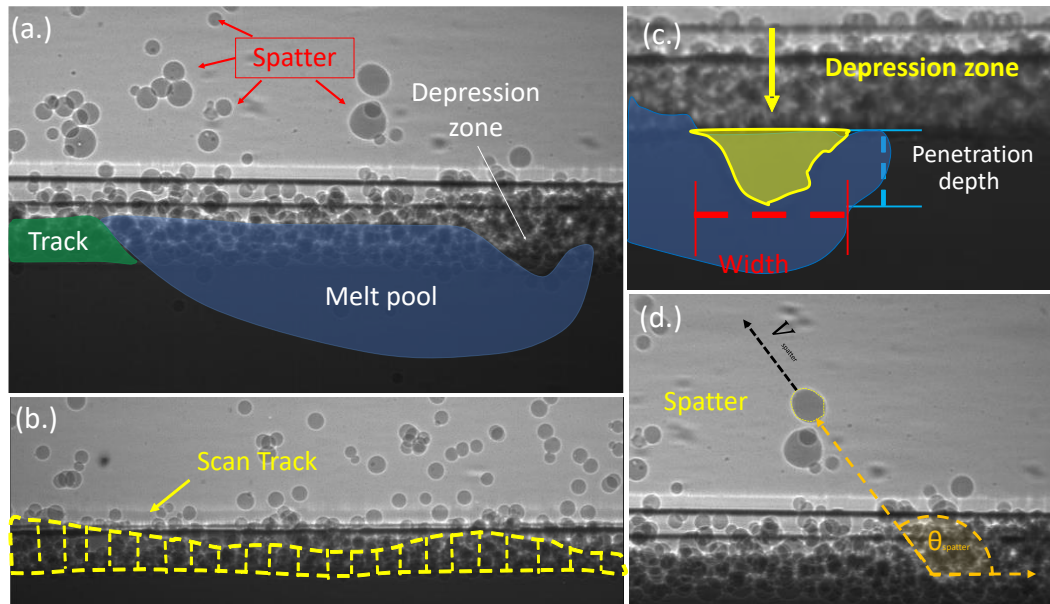


Figure 5. SLM dynamics (a, b, c, d) X-ray images of selective laser melting. (a) experimental dynamic schematic marking measured SLM dynamics: depression zone, spatter, and scan track. (b) post-scan X-ray imaging marking the location and geometry of melted scan track. (c) experimental imaging demonstrating depression zone geometry. (d) x-ray imaging marking the spatter diameter  $d$ , direction  $\theta_{spatter}$ , velocity  $V_{spatter}$  and volume  $v_{spatter}$  during SLM.

The SLM dynamics are captured using high speed x-ray imaging. A test sample is placed in an argon vacuum chamber to prevent oxidation during laser scanning. Testing is conducted for all PSDs at 1 atm. During laser scanning, a single line of powder is melted in the x-ray viewing window. At 50kHz frame rate, the dynamics during the melting process are captured over hundreds of images during laser scanning. For analysis, the geometry of the depression zone depth and width are visually recorded along the

scanning process. The resulting geometry is averaged, and overall fluctuations are recorded. Scan track profile is found the moment after solidification of the melt pool occurs during scanning. The height of the scan track along the viewing window is visually recorded and averaged. The spatter is determined by watching for the ejection of liquid spatter from the powder bed region. Once liquid spatter has escaped the powder region, the dynamics are analyzed. The angle of spatter is positioned relative to the laser location (front wall of depression zone) and measured relative to the substrate and ejection angle as the spatter escapes from the powder bed until it is not visible within the viewing window. The velocity of spatter is found assuming a 2D projection by taking the central displacement in the x-y coordinates over a known change in time. The diameter of the liquid spatter is determined once the spatter leaves the powder bed region. The spatters diameter,  $d$  is found by averaging the x-axis and y-axis diameter of the powder assuming a near spherical geometry. The volume is found for all spatter produced by assuming spherical geometry of all spatter diameters. The total summation of all liquid spatter volume is collected within the viewing window for each test. Equations for the measuring the SLM dynamics are defined in the nomenclature section for additional clarity. Testing is conducted multiple times for each PSD and the resulting average effects on the SLM dynamics are recorded.

### 3. RESULTS AND DISCUSSION

#### 3.1. AVALANCHE ANGLE AND BREAK ENERGY

Testing was conducted using 6 different powder size distributions as ratios of small powder (15-25 $\mu\text{m}$ ) to large powder (38-45 $\mu\text{m}$ ): 0, 10, 30, 70, 90, 100 percent by weight. Testing was conducted to determine the effect that powder size distribution plays on the powder flowability. Previous studies claim that non-uniform particle distributions typically lead to overall reductions in powder flowability [18,19]. This work will look to specifically test to see if there is a trend in the size distribution and change in powder flowability conditions. Two major flowability conditions tested is the effect of powder size distributions on avalanche angle and break energy. The avalanche angle is the recorded angle at the instant of avalanche. The break energy is defined as the difference between the maximum energy of the sample powder before the avalanche begins and the starting energy of the powder sample before rotation begins. The flowability properties for both conditions are conducted for all PSDs.

The avalanche angle is the angle produced during rotation within the mercury scientific cylinder right before the static powder buildup along the wall collapses. The increased angle of the static powder buildup has a negative effect on the flowability of powder during powder feeding in commercial systems. Changing the powder distribution from homogeneous to non-homogeneous distribution leads to an increase in the avalanche angle (Figure 6. a.). This is caused by an increase of finer particles being introduced within larger powder systems, decreasing the overall flowability of the system by inducing increased interstitial contact and inter-particle friction within the powder bed

as described and demonstrated by work from Brika et al [32]. Work from Liu et al. also highlighted reductions in flowability characteristics such as the Hausner ratio increase due to increased PSD from a near homogenous to a non-homogeneous powder system [20]. From testing, the lowest avalanche angle occurred at the homogenous systems with 0 and 100% 15-25 $\mu\text{m}$  powder. A unique trend was present when testing at the dense packing mixtures. At 10 and 90% 15-25 $\mu\text{m}$  powder, a large increase in the avalanche angle was present compared to higher and lower PSDs surrounding them. Within the powder bed system, the PSDs generate local regions where dense powder packing causes increased amounts of inter-particle contact [32], increasing the inter-frictional forces at the location within the powder bed. The increase in frictional forces resists the transition from potential to kinetic avalanche during powder rotation. The particle size distributions near their powder's high atomic packing densities generates an increase to the inter-frictional forces, decreasing the flowability of the powder bed system.

The break energy of the six PSD showed an upward trend as the amount of % 15-25 $\mu\text{m}$  powder increased. At the powder's high atomic packing distributions (10 and 90%), a large jump in the break energy was observed. The highest break energy occurred at 37mJ/kg at 90% PSD; the lowest break energy occurred at 20.6mJ/kg at 0%. The most noticeable effect is the sudden jump from 0 to 10% 15-25 $\mu\text{m}$  powder distribution causing a change of 16mJ/kg on the resulting break energy during testing. The cause of increased break energy is caused by the increased inter-frictional similar to the resulting avalanche angle.

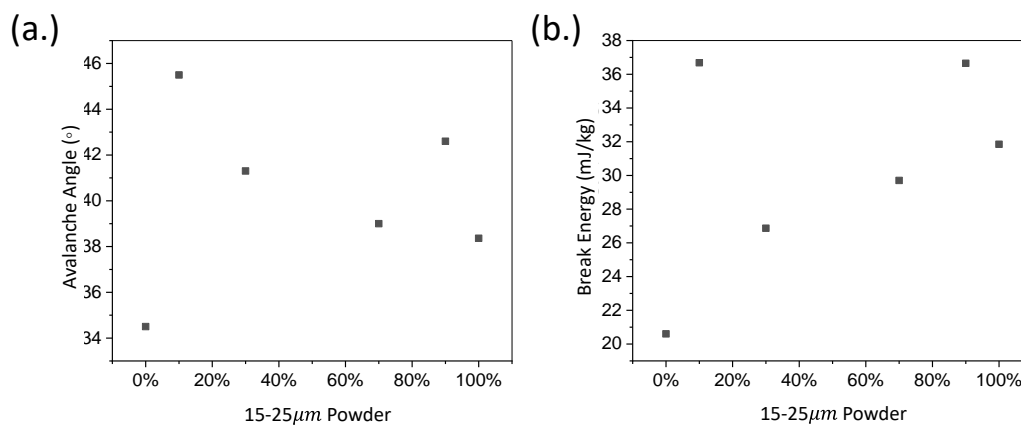


Figure 6. Avalanche angle and break energy of different particle size distributions. Avalanche angle and break energy were calculated for all particle size distributions. The size distributions are marked along the x-axis depending on the weight percentage of 15-25 $\mu\text{m}$  powder for surface fractal and avalanche angle. Avalanche angle is measured by degree from the horizontal to peak tip during the occurrence of powder avalanche. Break energy is determined from the difference in the potential energy at the moment of avalanche to the potential energy prior to rotation.

Table 3. PSD's effects on avalanche angle and break energy.

Powder flowability properties		
Powder size distribution (% 15-25 $\mu\text{m}$ )	Avalanche Angle ( $^{\circ}$ degrees)	Break energy (mJ/kg)
0	34.7	20.9
10	45.6	36.9
30	41.3	27
70	39	29.6
90	42.8	36.8
100	38.5	31.3

Table 3 highlights the 2 flowability features, avalanche angle and break energy, tested within this work. The testing demonstrated the changes in flowability properties due to the change in the powder size distribution. As the powder changed from a commercial grade homogenous state to a non-homogenous (no powder mixing vs.

powder mixing), changes in the avalanche angle and energy were clearly observed.

Testing near the efficient atomic packing region for the two commercial powder sizes led to significant changes in the powder's overall flowability.

### **3.2. EFFECT OF PSD ON FLOWABILITY**

Flowability testing revealed unique phenomena for plasma atomized powder at varying PSDs. An increase in PSD (non-homogeneous) resulted in a larger avalanche angle and break energy due to reduced flowability. Testing, however, showed that the decreased flowability did not have a linear or quadratic relationship between the two homogeneous powders. The system showed sharp peaks near the atomic packing densities of the two powders.. Work by Abdullah et al. focused on the manipulation of powder bulk densities on overall flowability. The work demonstrated the effect of adding fines (i.e., small powder inclusions) into powder bed systems to determine the effect on flowability. His work discovered that these inclusions fill void cavities during powder flow and adhere to large particles preventing percolation and increasing cohesivity and internal friction within the system[33]. Our work demonstrates peaks due to the increased bulk density of the powder by creating a PSD with efficient clustering of satellite powders around a single, central powder generated within the mixture. The efficient clustering is apparent in dynamic flowability by increasing the surface area of clustered powders in contact with each other. Simulation work by Vo et al. conducted extensive work into the role of inter-particle friction's effects on granular flow. This work utilized three-dimensional particle dynamics simulation to highlight the impact of the inter-frictional forces on the resulting frictional coefficient's effect on granular powder

flow[34]. Additional work by Nan et al. utilizes Discrete element method to identify the causes and effects of powder jamming during powder spreading. Simulations required determination of physical contact forces between contacting particles and walls and to determine and simulate powder spreading systems of granular powder and jamming during flow[35]. Increased bulk density in localized regions of dense packing at the specified PSDs causes increased interstitial contact, increasing the total internal friction between the powders during rotations. The internal friction requires more energy on the powder mixture in order to break the static position of the powder, resulting in decreased flowability demonstrate during testing.

The atomic packing densities by mixing the two Pyrogenesis powders (15-25 $\mu m$  and 35-48 $\mu m$ ) occur near 90 and 10 percent 15-25 $\mu m$  powder. The highest packing density near the homogenous mixture (100 or 0%) demonstrates the uncertainty faced in commercial powder additive manufacturing. New powder for part-to-part fabrication with small amounts (10% for this instance) of non-uniform powder can lead to sudden, sharp drops in the powder's overall flowability. These sudden drops in additive manufacturing can lead to quality reduction during powder spreading/deposition or cause jamming during spreading/deposition causing powder loss and increased cycle time due to machine maintenance/clearing. Determining the powder's PSD to ensure that it is not near atomic packing density before powder spreading is essential for reducing the possibility of quality loss due to sudden decrease in flowability between powder batches. To mitigate or eliminate flowability uncertainty, reducing the powder size distribution to closest to homogenous as possible is preferred[20]. Since obtaining homogeneous powder is difficult in commercial industry, reducing the distribution curve by eliminating

the outlier powders will decrease the chance of the powder having an atomic packing distribution. The adjustment in the powder's PSD will greatly reduce the uncertainty during the additive manufacturing process and can lead to increased quality and efficiency of the system.

### 3.3. EFFECT OF PSD ON SLM DYNAMICS

Testing is conducted at the 6 unique PSDs to determine the effects on the SLM dynamics. Testing is conducted at a beam size of  $90\mu\text{m}$  with standard laser gaussian distribution. The focal plane is placed at  $2.5\text{mm}$  below the powder bed location. Laser scanning was conducted with a laser power and scan speed of  $364\text{W}$  and  $0.9\text{m/s}$  respectively. Powder bed thickness is maintained at  $\sim 100\mu\text{m}$ . Testing observed the effect that the change in PSD has on the depression zone, spatter, and build track dynamics.

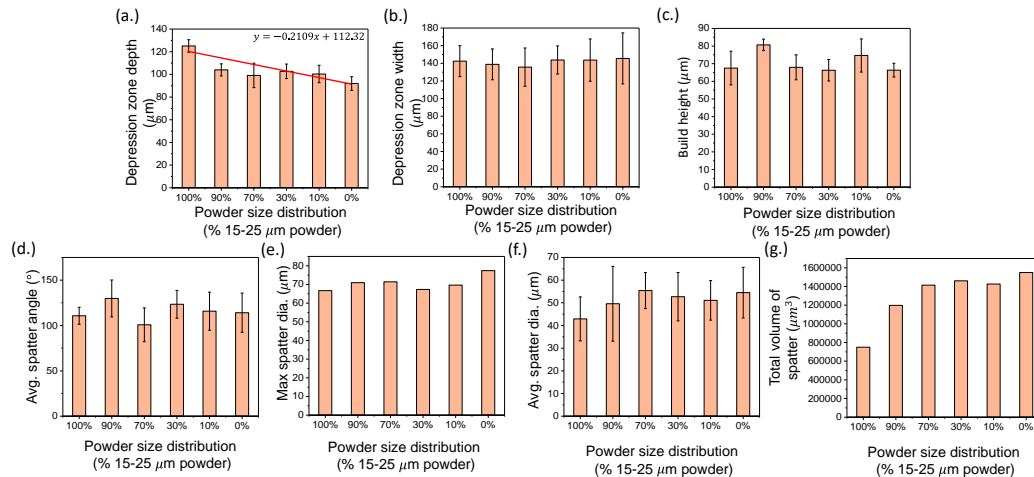


Figure 7. SLM dynamics. Depression zone, build height, and spatter dynamics were determined for each PSD. (a-b) Variation of the depression zone depth and width due to change in PSD. (c) Variation in build height due to change in PSD. (d-g) Variation in the spatter angle, max diameter, avg. diameter, and volume due to change in PSD.

The results demonstrated in Figure 7. (a-b) depict the change in the depression zone depth and width due to varying the mixing of small (15-25 $\mu\text{m}$ ) and large (38-45  $\mu\text{m}$ ) powder. A downward slope of -0.2109 was determined due to the increase of large powder percentage into small powder. The trend is due to the change in powder size, as the large powder requires greater energy input to melt and fuse to the substrate during scanning. The cause for the increased energy is due to the reduction in laser absorption of the powder bed as the size of the powder increases. Work by Zhang et al. demonstrates a three-dimensional laser absorption model and highlights the effect of the powder size on the resulting energy absorption into the system. Their work demonstrated the increase in particle size decreased the presence of multi-reflection absorption of surrounding particles, creating inhomogeneous irradiance intensity and a corresponding decrease in the intensity inputted into the powder bed system[36]. Our work experimentally demonstrates the model, showing as the average particle size of the system increases with decreasing depression zone depth. The depression zone width was not significantly affected by the increase in the powder size distribution. The standard deviation in both the depression depth and width remained consistent during variation of the powder size distribution.

Figure 7. (c) depicts the variation in the build height due to the fluctuation of the powder size distribution. A noticeable trend was found when operating at the two efficient powder packing density. The 90% small powder and 10% small powder had the highest average build height with increases of 19.49% and 10.56% to the 100% 15-25 $\mu\text{m}$  powder respectively. The other PSDs did not have any significant change to the build

track's overall height. Build height fluctuation was the most stable at 90% small powder with an average deviation less than  $5\mu m$ .

The experiments displayed in Figure 7. (d-g) demonstrate the change in spatter dynamics with the manipulation of PSD. The increase in PSD caused an increase in the overall spatter produced during SLM scanning. A change of 10% PSD from 100% to 90% 15-25 $\mu m$  powder caused the greatest increase, increasing the spatter volume by almost 60%. The gradual increase from 15-25 $\mu m$  to 38-45 $\mu m$  led to an increase in the overall spatter volume produced by ~50% over the testing range. The change in PSDs did not lead to any statistically significant effect on the fluctuations in the spatter dynamics.

### **3.4. SLM IMPACT DUE TO CHANGE IN PSD**

The change in the PSD in the powder system gave significant changes to the overall SLM dynamics. The change in SLM dynamics will affect the physical properties of the finalized part, hindering the physical capabilities and repeatability of the part. Most notably, the change in PSD had a significant effect on the depression zone depth, spatter volume, and scan track build height.

The increase in the PSD from 15-25 $\mu m$  towards 38-45 $\mu m$  showed a downward trend on the overall depression zone depth. This decreasing trend is driven by the increased localized energy that is required to melt larger powders for fusion to the substrate to occur due to decreased absorption. As the powder bed arrives closer to the 38-45 $\mu m$  powder bed system, the decrease in particle-to-particle reflections occur from the laser scanning. These decreased reflections decrease the overall absorptivity of the laser, decreasing the total energy deposited by the laser[36]. The increased energy

deposited within the powder bed decreases the amount of energy deposited into the substrate; the reduced energy limits the total amount of metal vaporization developed by the laser, decreasing the depression depth generation during laser scanning. A similar increase in the spatter volume is witnessed with increasing powder size. The increased energy deposition into the larger powder, decreasing reflection and absorptivity overall, causes powder melting or ejection to occur prior to fusion to the substrate. The reduced fusion causes a greater volume of powder to be ejected as spatter prior to capture by the melt pool or fusion to the substrate can occur. The two factors appeared primarily affected by the PSD but did not have a noticeable effect near the atomic packing density locations.

The change in the scan track's build height, however, demonstrated sharp changes due to operating laser scanning near the atomic packing PSDs. The two locations saw increases greater than 10 and 20% in the overall deposited scan track height when operating with the same initial powder bed thickness. The atomic packing locations drove an increase in the localized density of the powder bed, depositing a greater total volume of powder within a single layer on the build track. Work by Spierings et al. demonstrates the necessity of fine particle inclusion to fill voids within coarse grains. The works found the inclusions of these fine particles generate greater density to the powder bed system and result in improved scan surface quality and part density. Spiering's work utilizes a dense atomic packing system to create high density locations within the powder bed by reducing the porosity within the powder bed system[26,37]. During laser scanning, the atomic packing locations created greater density powder beds after dynamic spreading, causing an increase in the scan track height while decreasing the overall fluctuation in the

scan track profile. The increased height during scanning can greatly benefit the cycle time during production of finalized parts by reducing the number of laser scans required for part fabrication. The decreased fluctuations limit the production of layer by layer non uniformity and defect production during large scale part fabrication. The ability to operate successfully (without flowability driven failure) at the atomic packing density of a mixed powder system can greatly enable a more efficient and repeatable process for AM part manufacturing.

#### **4. CONCLUSION**

This work investigated the effects of PSD on the flowability and SLM dynamics of powders under commercial additive manufacturing conditions. More specifically, two Pyrogenesis powders were mixed at 6 unique PSDs and their flowability was measured; two of the PSDs were chosen near D.B. Miracle's atomic packing density to determine if the dense powder packing of commercial powder would have a significant effect on the overall flowability of the powder. Dense packing powder bed systems were found to greatly increase the avalanche angle and break energy during revolution testing. These results signify a sudden decrease in localized powder bed flowability during spreading. The cause is due to an increase in contact forces generated by additional powder-to-powder surface contact within the dense powder bed systems. In-situ x-ray imaging testing was conducted to experimentally demonstrate the effects of dense packing systems on the SLM dynamics. The major conclusions found are:

- Testing of 6 PSDs of commercial grade Ti6Al4V powder (15-25 $\mu\text{m}$  / 38-45 $\mu\text{m}$ ) were conducted. Two PSDs were generated using D.B. Miracle's atomic packing density to determine powder systems with localized dense powder packing within the powder bed.
- Flowability testing experimentally determined the flow properties of the 6 PSDs through dynamic testing of the avalanche angle and break energy. Testing demonstrated variation in avalanche angle and break energy by up to 10.9° and 16mJ/kg respectively
- Dense packing PSDs yielded sudden increases in both the avalanche angle and break energy compared to the surrounding PSDs by up to ~30% and ~70% increases respectively. Demonstrating the effect of dynamics testing on dense packing PSDs creating increases in the systems inter-particle friction forces, creating sudden decreases in the overall flowability of the system.
- Powder flowability experimentally verified the decrease in the flowability of homogenous to inhomogeneous PSDs attributed to the lack of inclusion of fine particles within cavities of the dynamic powder bed system, decreasing inter-frictional forces in the system.
- Testing was conducted on the 6 PSDs utilizing in-situ high speed x-ray imaging to capture the SLM dynamics during laser scanning. Changes in PSDs depicted trends in the depression zone, scan track, and spatter dynamics identified during testing.
- Experimental testing verified and demonstrated previous simulations affecting the relationship between powder size and reduced energy deposition. A decreasing

trend of -2.109 was identified with increasing PSD towards a larger average powder size. This work experimentally proved the decrease in inter-particle reflections resulting in decreased laser intensity through in-situ analysis by demonstrating the effective decrease in the depression zone geometry with increasing powder size.

- In-situ analysis of the scan track profile demonstrated the benefit of dense packing systems in commercial application. Two powder systems tested at dense packing locations generated increases up to ~20% in the scan track height with reduced fluctuation in the scan track profile.
- This work demonstrates the cause of uncertainty due to dense packing of powder systems in commercial AM. The risk and benefits of dense powder systems utilizing atomic powder packing PSDs are discovered through dynamic flowability and in-situ high speed x-ray imaging. Reductions in flowability are present due to increased inter-particle friction forces near regions of dense packing during flow, while increases in scan track profile and smoothness are found due to the increase in dynamic spreading powder density during laser scanning.

## **ACKNOWLEDGEMENTS**

The authors would like to thank Alex Deriy, Niranjan Parab, Kamel Fezzaa, and Tao Sun at the APS for their help on the beamline experiments. This research used resources of the Advanced Photon Source, a U.S. Department of Energy (DOE) Office of

Science User Facility operated for the DOE Office of Science by Argonne National Laboratory under Contract No. DE-AC02-06CH11357. This work also received funded from the Boeing Company through the Center for Aerospace Manufacturing Technology (CAMT) at Missouri University of Science and Technology, with special thanks to Amaka Ibeh, Fatmata Barrie, and James Castle.

### BIBLIOGRAPHY

- [1] C. Meier, R. Weissbach, J. Weinberg, W.A. Wall, A.J. Hart, Critical influences of particle size and adhesion on the powder layer uniformity in metal additive manufacturing, *Journal of Materials Processing Technology*. 266 (2019) 484–501. <https://doi.org/10.1016/j.jmatprotec.2018.10.037>.
- [2] W. Gao, Y. Zhang, D. Ramanujan, K. Ramani, Y. Chen, C.B. Williams, C.C.L. Wang, Y.C. Shin, S. Zhang, P.D. Zavattieri, The status, challenges, and future of additive manufacturing in engineering, *Computer-Aided Design*. 69 (2015) 65–89. <https://doi.org/10.1016/j.cad.2015.04.001>.
- [3] M. Grasso, B.M. Colosimo, Process defects and in situ monitoring methods in metal powder bed fusion: a review, *Measurement Science and Technology*. 28 (2017) 44005. <https://doi.org/10.1088/1361-6501/aa5c4f>.
- [4] D.K.Y. Low, L. Li, A.G. Corfe, Characteristics of spatter formation under the effect of different laser parameters during laser drilling, *Journal of Materials Processing Technology*. 118 (2001) 179–186.
- [5] C.Y. Yap, C.K. Chua, Z.L. Dong, Z.H. Liu, D.Q. Zhang, L.E. Loh, S.L. Sing, Review of selective laser melting: Materials and applications, *American Institute of Physics*. 2 (2015) 01–21. <https://doi.org/10.1063/1.4935926>.
- [6] H. Gong, J.J.S. Dilip, L. Yang, C. Teng, B. Stucker, Influence of small particles inclusion on selective laser melting of Ti-6Al-4V powder, *IOP Conference Series: Materials Science and Engineering*. 272 (2017) 2–8. <https://doi.org/10.1088/1757-899X/272/1/012024>.

- [7] I. Mehdipour, K.H. Khayat, Effect of particle-size distribution and specific surface area of different binder systems on packing density and flow characteristics of cement paste, *Cement and Concrete Composites*. 78 (2017) 120–131. <https://doi.org/10.1016/j.cemconcomp.2017.01.005>.
- [8] C.L.A. Leung, S. Marussi, M. Towrie, R.C. Atwood, P.J. Withers, P.D. Lee, The effect of powder oxidation on defect formation in laser additive manufacturing, *Acta Materialia*. 166 (2019) 294–305. <https://doi.org/10.1016/j.actamat.2018.12.027>.
- [9] O. Ertugrul, H.S. Park, K. Onel, M. Willert-Porada, Effect of particle size and heating rate in microwave sintering of 316L stainless steel, *Powder Technology*. 253 (2014) 703–709. <https://doi.org/10.1016/j.powtec.2013.12.043>.
- [10] G. Spierings, A.B. & Levy, Comparison of density of stainless steel 316L parts produced with selective laser melting using different powder grades, *Review Literature And Arts Of The Americas*. (2009) 342–353.
- [11] D.B. Miracle, W.S. Sanders, O.N. Senkov, The influence of efficient atomic packing on the constitution of metallic glasses, *Philosophical Magazine*. 83 (2003) 2409–2428. <https://doi.org/10.1080/1478643031000098828>.
- [12] C. Qiu, C. Panwisawas, M. Ward, H.C. Basoalto, J.W. Brooks, M.M. Attallah, On the role of melt flow into the surface structure and porosity development during selective laser melting, *Acta Materialia*. 96 (2015) 72–79. <https://doi.org/10.1016/j.actamat.2015.06.004>.
- [13] H.G. Coe, S. Pasebani, Use of bimodal particle size distribution in selective laser melting of 316L stainless steel, *Journal of Manufacturing and Materials Processing*. 4 (2020). <https://doi.org/10.3390/jmmp4010008>.
- [14] J. Ma, L.C. Lim, Effect of particle size distribution on sintering of agglomerate-free submicron alumina powder compacts, *Journal of the European Ceramic Society*. 22 (2002) 2197–2208. [https://doi.org/10.1016/S0955-2219\(02\)00009-2](https://doi.org/10.1016/S0955-2219(02)00009-2).
- [15] D.J. Lacks, A. Levandovsky, Effect of particle size distribution on the polarity of triboelectric charging in granular insulator systems, *Journal of Electrostatics*. 65 (2007) 107–112. <https://doi.org/10.1016/j.elstat.2006.07.010>.
- [16] C. Chang, R.L. Powell, Effect of particle size distributions on the rheology of concentrated bimodal suspensions, *Journal of Rheology*. 38 (1994) 85–98. <https://doi.org/10.1122/1.550497>.

- [17] B. Guillaume, F. Boschini, I. Garcia-Cano, A. Rulmont, R. Cloots, M. Ausloos, Optimization of BaZrO<sub>3</sub> sintering by control of the initial powder size distribution; a factorial design statistical analysis, *Journal of the European Ceramic Society*. 25 (2005) 3593–3604. <https://doi.org/10.1016/j.jeurceramsoc.2004.09.022>.
- [18] S.E. Brika, M. Letenneur, C.A. Dion, V. Brailovski, Influence of particle morphology and size distribution on the powder flowability and laser powder bed fusion manufacturability of Ti-6Al-4V alloy, *Additive Manufacturing*. 31 (2020) 100929. <https://doi.org/10.1016/j.addma.2019.100929>.
- [19] J.K. Prescott, R.A. Barnum, On powder flowability, *Pharmaceutical Technology*. 24 (2000) 60-84+236.
- [20] C.T.I.A.R.H. Bochuan Liu Ricky Wildman, Investigation the Effect of Particle Size Distribution on Processing Parameters Optimisation in, Additive Manufacturing Research Group, Loughborough University. (2011) 227— – 238.
- [21] C. Meier, R. Weissbach, J. Weinberg, W.A. Wall, A.J. Hart, Critical influences of particle size and adhesion on the powder layer uniformity in metal additive manufacturing, *Journal of Materials Processing Technology*. 266 (2019) 484–501. <https://doi.org/10.1016/j.jmatprotec.2018.10.037>.
- [22] J. Ma, L.C. Lim, Effect of particle size distribution on sintering of agglomerate-free submicron alumina powder compacts, *Journal of the European Ceramic Society*. 22 (2002) 2197–2208. [https://doi.org/10.1016/S0955-2219\(02\)00009-2](https://doi.org/10.1016/S0955-2219(02)00009-2).
- [23] Y. Bai, G. Wagner, C.B. Williams, Effect of particle size distribution on powder packing and sintering in binder jetting additive manufacturing of metals, *Journal of Manufacturing Science and Engineering, Transactions of the ASME*. 139 (2017) 1–6. <https://doi.org/10.1115/1.4036640>.
- [24] D.B. Miracle, Efficient local packing in metallic glasses, *Journal of Non-Crystalline Solids*. 342 (2004) 89–96. <https://doi.org/10.1016/j.jnoncrysol.2004.05.017>.
- [25] M. Sinico, G. Cogo, M. Benettoni, I. Calliari, A. Pepato, INFLUENCE OF POWDER PARTICLE SIZE DISTRIBUTION ON THE PRINTABILITY OF PURE COPPER FOR SELECTIVE LASER MELTING, n.d.
- [26] A.B. Spierings, G. Levy, Comparison of density of stainless steel 316L parts produced with selective laser melting using different powder grades, n.d.
- [27] D.B. Miracle, Efficient local packing in metallic glasses, *Journal of Non-Crystalline Solids*. 342 (2004) 89–96. <https://doi.org/10.1016/j.jnoncrysol.2004.05.017>.

- [28] D.B. Miracle, W.S. Sanders, O.N. Senkov, The influence of efficient atomic packing on the constitution of metallic glasses, *Philosophical Magazine*. 83 (2003) 2409–2428. <https://doi.org/10.1080/1478643031000098828>.
- [29] V.R. Nalluri, M. Kuentz, Flowability characterisation of drug-excipient blends using a novel powder avalanching method, *European Journal of Pharmaceutics and Biopharmaceutics*. 74 (2010) 388–396. <https://doi.org/10.1016/j.ejpb.2009.09.010>.
- [30] B.C. Hancock, K.E. Vukovinsky, B. Brolley, I. Grimsey, D. Hedden, A. Olsofsky, R.A. Doherty, Development of a robust procedure for assessing powder flow using a commercial avalanche testing instrument, *Journal of Pharmaceutical and Biomedical Analysis*. 35 (2004) 979–990. <https://doi.org/10.1016/j.jpba.2004.02.035>.
- [31] Q. Guo, C. Zhao, L.I. Escano, Z. Young, L. Xiong, K. Fezzaa, W. Everhart, B. Brown, T. Sun, L. Chen, Transient dynamics of powder spattering in laser powder bed fusion additive manufacturing process revealed by in-situ high-speed high-energy x-ray imaging, *Acta Materialia*. 151 (2018) 169–180. <https://doi.org/10.1016/j.actamat.2018.03.036>.
- [32] S.E. Brika, M. Letenneur, C.A. Dion, V. Brailovski, Influence of particle morphology and size distribution on the powder flowability and laser powder bed fusion manufacturability of Ti-6Al-4V alloy, *Additive Manufacturing*. 31 (2020). <https://doi.org/10.1016/j.addma.2019.100929>.
- [33] E. Chan, E.C. Abdullah, D. Geldart, The use of bulk density measurements as flowability indicators Cite this paper The use of bulk density measurements as flowability indicators, 1999.
- [34] T.T. Vo, T. Nguyen-Thoi, The role of inter-particle friction on rheology and texture of wet granular flows, *European Physical Journal E*. 43 (2020). <https://doi.org/10.1140/epje/i2020-11987-2>.
- [35] W. Nan, M. Pasha, T. Bonakdar, A. Lopez, U. Zafar, S. Nadimi, M. Ghadiri, Jamming during particle spreading in additive manufacturing, *Powder Technology*. 338 (2018) 253–262. <https://doi.org/10.1016/j.powtec.2018.07.030>.
- [36] J. Zhang, D. Gu, Y. Yang, H. Zhang, H. Chen, D. Dai, K. Lin, Influence of Particle Size on Laser Absorption and Scanning Track Formation Mechanisms of Pure Tungsten Powder During Selective Laser Melting, *Engineering*. 5 (2019) 736–745. <https://doi.org/10.1016/j.eng.2019.07.003>.

- [37] A.B. Spierings, N. Herres, G. Levy, M.A.B. Spierings, Influence of the particle size distribution on surface quality and mechanical properties in AM steel parts  
ETH Library Influence of the particle size distribution on surface quality and mechanical properties in additive manufactured stainless steel parts, *Rapid Prototyping Journal*. 17 (n.d.). <https://doi.org/10.3929/ethz-a-006443611>.

## SECTION

### 2. CONCLUSION

Within this work, we report the (1) five unique types of spatter based on their characteristics and formation mechanisms due to high speed in-situ x-ray imaging, (2) effects of the ambient and processing conditions on the spatter dynamics, (3) the generation of spatter formation mapping for AlSi10Mg, (4) the effect of small changes in the laser (laser power, scan speed, and beam size) and powder processing parameters (powder size, bed thickness, size distribution) that contribute to uncertainty in the SLM additive manufacturing process, (5) and determining the source of uncertainty of powder flowability of Ti6Al4V due to the efficient atomic packing of powder with non-homogenous particle size distributions. We show the formation mechanisms and underlying physics of the production of five unique types of spatter in AM LPBF. The resulting characteristics of the spatter dynamics are quantified due to their speed and size after ejection. The effects of variations to laser scan speed, laser power, and ambient pressure have on the overall spatter dynamics are determined and experimentally demonstrated. Mitigation strategies are shown with a spatter formation mapping for AlSi10Mg. We show that small changes in the laser (<5%) and powder (<20 $\mu$ m) processing conditions produce significant changes in the depression zone, melt pool, build height, and spatter dynamics. Changes of 5% in laser processing conditions or changes of 20 $\mu$ m in powder size led to a ~10% change in the depression zone and melt pool geometry. Processing powder near their atomic packing density by changing the

powder distribution by 10% led to increases up ~20% in the overall build height. The changes in the ~10% of the laser beam size and ~20 $\mu$ m in the powder size led to large variations in the overall spatter geometry and total volume during laser melting. This work demonstrated the efficient atomic packing density for plasma atomized commercial grade powder and tested the avalanche angle, avalanche energy, break energy, and surface fractal. Powder flowability working near the efficient atomic packing mixtures (10 and 90%) led to significant increases in the avalanche angle, surface fractal, avalanche energy, and break energy.

**VITA**

Zachary Aaron Young attended Missouri University of Science and Technology, where he graduated in 2018 with a Bachelor of Science in Aerospace Engineering. He received his PhD in Mechanical Engineering from Missouri S&T in December 2021